Title

Electronic Structure and the Effects of Spin-Orbit Coupling and Orbital Character in Low-Dimensional Semiconducting Materials with Electronic Device Applications

Author

Latzke, Drew

Publication Date

2018

Electronic Structure and the Effects of Spin-Orbit Coupling and Orbital Character in Low-Dimensional Semiconducting Materials with Electronic Device Applications

by

Drew Latzke

A dissertation submitted in partial satisfaction of the

requirements for the degree of

Doctor of Philosophy

in

Applied Science and Technology

and the Designated Emphasis

in

Nanoscale Science and Engineering

in the

Graduate Division

of the

University of California, Berkeley

Committee in charge:

Professor Alessandra Lanzara, Chair
Professor Jeffrey Neaton
Professor Junqiao Wu

Fall 2018

Electronic Structure and the Effects of Spin-Orbit Coupling and Orbital Character in Low-Dimensional Semiconducting Materials with Electronic Device Applications

Abstract

Electronic Structure and the Effects of Spin-Orbit Coupling and Orbital Character in Low-Dimensional Semiconducting Materials with Electronic Device Applications

by

Drew Latzke

Doctor of Philosophy in Applied Science and Technology

and the Designated Emphasis in Nanoscale Science and Engineering

University of California, Berkeley

Professor Alessandra Lanzara, Chair

Interest in low-dimensional ($\leq$ 2-dimensional) semiconducting materials is ever growing as electronic device sizes shrink and new physics continues to emerge at such a microscopic scale. Heterostructures allow for a set of physical building blocks made from low-dimensional materials that can be used to tailor devices to obtain precise and unique electronic interactions and device characteristics. Over time as this field has grown, certain research materials that for a time were overlooked in favor of other materials have come into renewed interest as a result of their unique properties that were previously deemed not as useful or were simply left undetected. One such example of this is the family of thin film transition metal dichalcogenides (TMDs), whose unique monolayer and thin film photoluminescence, band gap transition, and spin-orbit-coupling-induced physics has recently been studied intensely as a result of their unique spintronics and valleytronics applications. Another example is C_{60} which has an extremely unique low-dimensional buckyball molecular structure. It too can take on a crystalline thin film form to be used in heterostructures and electronic devices, but experimental evidence of long-range electronic order in thin film C_{60} has been lacking until now.

This dissertation presents angle-resolved photoemission spectroscopy (ARPES) studies of multiple TMD and C_{60} compounds with supporting theory calculations to investigate the electronic stucture of these materials. Specific attention is given to the effects of spin-orbit coupling and orbital character. The relationship between the electronic properties of bulk and thin film TMDs is elaborated in detail with a focus on the valence band splitting at the K point. The first observation of a dispersive thin film C_{60} band structure is discussed as well as the unique photoemission traits of the C_{60} band manifolds. Study of the electronic properties of these low-dimensional TMD and C_{60} materials provides important considerations for current and future cutting-edge electronic device applications.

The outline of the paper is as follows:

Chapter 1 provides an introduction to C_{60} including its history, structure, and electronic properties with particular emphasis on its thin film form. Chapter 2 introduces the primary experimental technique used in this dissertation—angle-resolved photoemission spectroscopy (ARPES). The basic principles of ARPES as well as the specifics of synchrotron-based ARPES are discussed. Additionally, the basic principles of low-energy electron diffraction (LEED) and a method for extracting lattice constants from LEED data are discussed.

Chapter 3 is the main chapter discussing the results of our transition metal dichalcogenide (TMD) studies. It begins with an introduction to TMDs including their structure, band gap, and the effect of strong spin-orbit coupling (SOC) on their unique spin- and valley-based physics. The origins of the valence band splitting in bulk TMDs (specifically MoS_2 and WS_2), the effects of SOC, the relationship between bulk and thin film TMDs, and the relationships between splitting, band gap, and molecular weight are discussed with ARPES data and supporting theory calculations.

Chapter 4 transitions from the main material of interest being TMDs to C_{60} through a discussion of high quality C_{60} growth. It gives an overview of both historical and modern C_{60} thin film growth on various substrates. Specific focus is given to growth on the strong SOC substrate TMD MoS_2. This is followed by a transition to growth on a novel substrate also with strong SOC, Bi_2Se_3, which is the type of thin film C_{60} sample studied in Chapters 5 and 6.

Chapters 5 and 6 present the results of our thin film C_{60} studies. Chapter 5 provides an in-depth study of the first experimental observation of highly-dispersive band structure in pure C_{60} through ARPES measurements supported by first-principles calculations. The effects previously hindering this observation are discussed as well as the role of the novel Bi_2Se_3 substrate in reducing C_{60} disorder and allowing for high quality epitaxial C_{60} deposition. Chapter 6 gives a comprehensive review of photon energy- and polarization-dependent effects in pure C_{60}. The effects of and new details about the orbital character of the C_{60} valence band manifolds are discussed with relation to linear- and circular-polarization dependent ARPES. Band manifold ARPES intensity oscillations with photon energy (and hence, k_z) are discussed including the implications for the precise details of the orbital character within each of the band manifolds.

To Amrita

For her unwavering and unimaginable support and love

Contents

List of Figures

List of Tables

Acknowledgments

Firstly, I want to thank my research advisor, Prof. Alessandra Lanzara, for her support and guidance throughout my graduate school tenure. Her knowledge and insights have proved invaluable and she has pushed me to develop and hone many useful skills for the next step in my career.

The Lanzara Research Group has been a welcoming and helpful group of students and postdocs. Greg Affeldt, Ryo Mori, and Kenny Gotlieb have been very helpful collaborators within the group and, more importantly, great friends. When I was starting out in the group, Choongyu Hwang, Chris Smallwood, Wentao Zhang, and Tristan Miller provided invaluable help and experience. I have had the pleasure of working with and getting help from many others including Chiu-Yun Lin, Jonathan Han Son Ma, Sam Ciocys, Nick Dale, Prosper Dzanwa, Conrad Stansbury, Danny Eilbott, Kayla Currier, Cassi Hunt, Claudia Fatuzzo, Bruin Pollard, Alex Nguyen, Chris Jozwiak, and Irene Lo Vecchio.

For many years now, I have had the pleasure of learning from and collaborating with Claudia Ojeda-Aristizabal, whose C_{60} knowledge has been invaluable to my research. I am grateful to Jonathan Denlinger, who has helped us obtain high-quality data at Beamline 4.0.3 of the ALS and provided a wealth of insights into my research.

Finally, I would like to thank the other UC Berkeley faculty members that provided me with valuable research and career insights, guidance, knowledge, and support throughout my time in graduate school: Professors Jeff Neaton, Junqiao Wu, Roger Falcone, James Analytis, Tsu-Jae King Liu, and David Attwood.

Chapter 1

Introduction to C_{60}

This chapter gives an introduction to fullerene C_{60} including the history of its synthesization and study, its physical structure, and electronic properties with particular emphasis on its thin film form.

1.1 History and First Synthesization

C is a unique molecule formed by sixty carbon atoms bonded in a near-spherical shape with icosahedral symmetry called a buckyball as shown in Fig. 1.1. The term buckyball is derived from buckminsterfullerene—the name given to C_{60} after the late Buckminster Fuller for his popularization of geodesic dome structures to which the C_{60} molecular structure bears a strong resemblance.

Despite the ubiquity of elemental carbon and graphite, the unusual structure of C_{60} hindered its discovery for quite some time. C_{60} laboratory synthesization was first reported by Kroto et al. [1] in 1985 by way of laser-vaporization of graphite as shown in Fig. 1.2. The synthesization of C_{60} was surprisingly not by design as the main goal was to investigate long carbon chain molecules found in interstellar space and circumstellar shells [2]. The synthesization process worked by first vaporizing the surface of a graphite disk with a pulsed laser. A flow of helium gas served to assist in this reaction and carry the resultant products away into a molecular beam which was then photoionized and probed by a time-of-flight mass spectrometer. A strong peak was found at the mass corresponding to sixty carbon atoms signalling the presence and hence, creation of C_{60}. The unique buckyball shape of C_{60} was proposed at the time as a likely candidate for the physical structure, but not confirmed until later.

While Kroto et al. had developed a method to synthesize C_{60}, the process could not easily produce significant quantities of concentrated C_{60}. It was not until 1990 that a method for synthesizing large quantities of molecular and solid C_{60} was developed by Krätschmer et al. [3]. They first formed a carbon soot containing a few percent by weight C_{60} by evaporating graphite electrodes in a helium atmosphere. They purified the resultant material by either

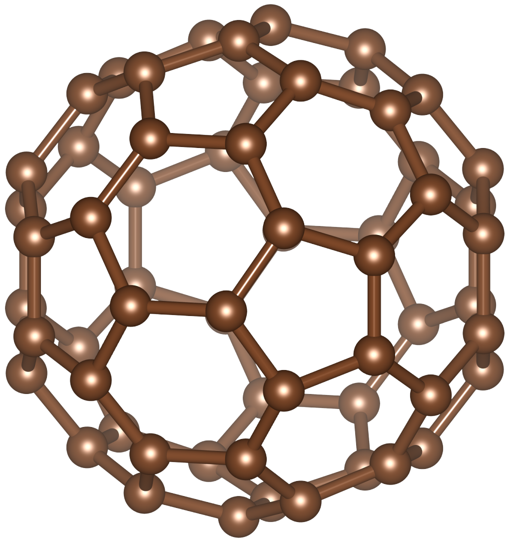

Figure 1.1: A C_{60} buckyball molecule consisting of 60 carbon atoms each with two single and one double bond.

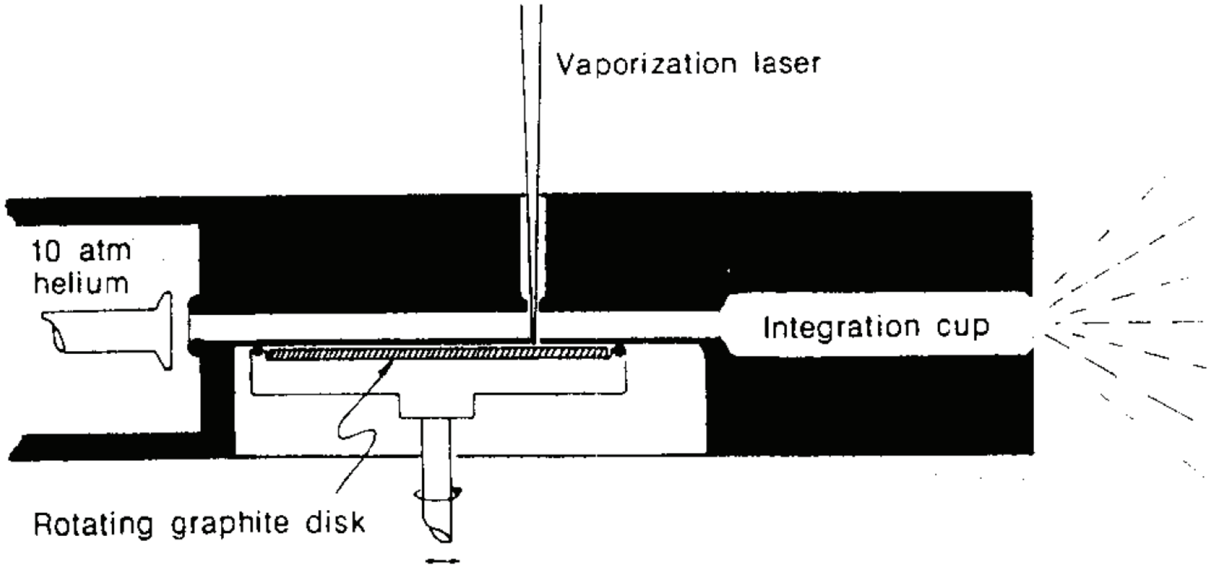

Figure 1.2: First method to synthesize C_{60}. A laser vaporizes a graphite disk, while helium gas carries the resultant species away. Reprinted by permission from Springer Nature: Ref. [1], 1985.

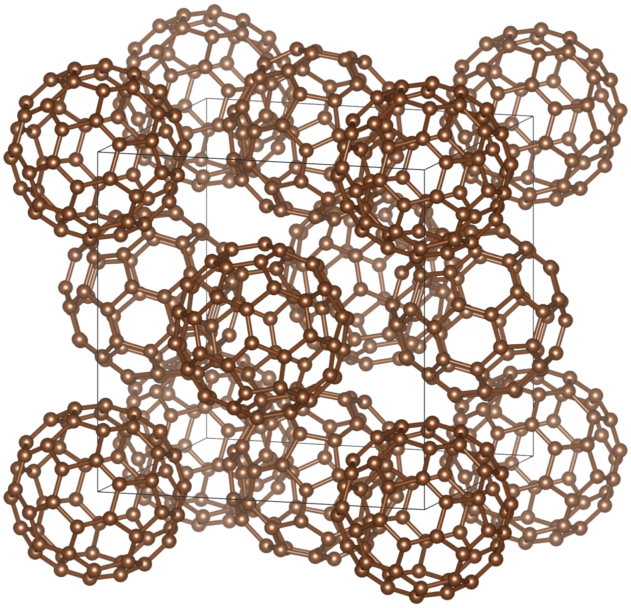

Figure 1.3: Bulk C_{60} with a buckyball at each fcc lattice site. Black lines denote unit cell.

dissolving it in a benzene solution and extracting a C_{60}-rich solution or by heating it in vacuum (or an inert atmosphere) to 400 °C to sublime the C_{60}. The end result of the process was purified C_{60} and even flakes of (somewhat disordered) bulk C_{60} crystals.

1.2 Physical Structure

The structure of a single C_{60} molecule is shown in Fig. 1.1. It has the shape of a truncated icosahedron (point group symmetry I_h) with a diameter of 7.1 Å [4]. Each (equivalent) carbon atom has two "single" bonds (lying between a pentagon and hexagon on the surface) of 1.46 Å and one "double" bond (between two hexagons) of 1.39 Å where all bonds are mainly of an aromatic character [5] (e.g. like those found in benzene). The bonds form 12 pentagon and 20 hexagon faces on the surface of the buckyball. The differents faces offer different possible bonding sites for bonding with other materials. This is an important consideration for C_{60} bonding with Bi_2Se_3 as will be discussed in Chapter 5.

In its bulk form, C_{60} arranges itself in a face-centered cubic (fcc) lattice (with one C_{60} molecule centered at each lattice site) and has a lattice constant of 14.2 Å [5] as shown in Fig. 1.3. C_{60} buckyballs are separated by a minimum gap of 3.1 Å [6] across which there is a weak inter-molecular bond. At room temperature the buckyballs freely rotate about their center of mass. This rotation is partially constrained below 249 K [5] which causes a structural transition from fcc to sc (Pa3 space group) with four buckyballs within the unit cell due to the partial rotational ordering.

In its thin film form it is deposited in layers corresponding to the (111) direction of the

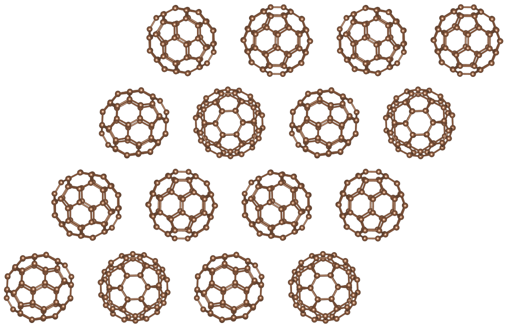

Figure 1.4: Thin film C_{60} with a buckyball at each hexagonal lattice site (corresponding to the (111) direction of the bulk fcc lattice).

bulk fcc lattice where each layer is arranged into a hexagonal lattice as shown in Fig. 1.4. The lattice constant of thin film C_{60} is 10.0 Å which is equal to the bulk nearest neighbor distance ($\frac{14.2\ \text{Å}}{\sqrt{2}}$) as the thin film structure is not, in general, significantly structurally different from the bulk (111) structure. The hexagonal lattice of thin film C_{60} has a hexagonal Brillouin zone (BZ) which is equivalent to the fcc (111) surface BZ shown in Fig. 1.5. The Γ point is located at the center of the BZ with a K point at each vertex and an M point at the center of each edge. The full bulk BZ is shown at the bottom of Fig. 1.5 where we can see that the bulk X and L points are both consolidated into the M point for thin film C_{60}, whereas the Γ and K points retain their labels.

1.3 Electronic Properties

Molecular Solid vs. Long Range Electronic Order

Each carbon atom in C_{60} has two “single” bonds and one “double” bond with neighboring atoms, similar to the sp^2 trigonal bonding in the related graphite and graphene, but with added complexity due to the curvature in C_{60} causing further hybridization between orbitals[8]. Considering bulk C_{60}, as an initial approximation, one would expect the electronic structure to be dominated by the electronic interactions within a single molecule (as opposed to those on the scale of the entire crystalline lattice) as the relative bond length between carbon atoms in a single molecule (∼1 Å) is much smaller than that of the van der Waals bonds between adjacent C_{60} molecules (∼10 Å) or even the bond length between the closest carbon atoms in adjacent C_{60} molecules (∼3 Å)[9]. Initial studies with infrared and Raman spectroscopy supported this approximation as the observed vibrational modes of solid C_{60} are consistent with a molecular solid[8]. While both experiment and theory agree that the valence band structure is composed of largely separate band clusters with small bandwidths (<1 eV) predicted by the highly molecular electronic structure, theory additionally predicts relatively large dispersions compared with the bandwidth (∼0.5 eV) of the indi-

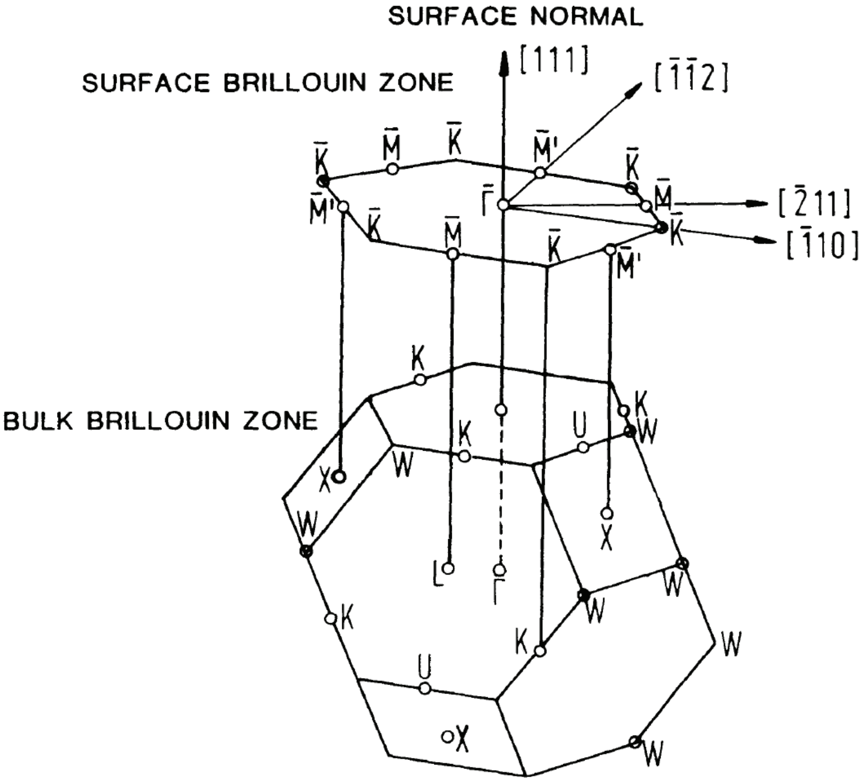

Figure 1.5: Bulk fcc C_{60} Brillouin zone and (111) reduced surface Brillouin zone corresponding to thin film C_{60}. Reprinted from Ref. [7].

vidual bands contained within a single band cluster pointing additionally to a long-range crystalline order[10]. In particular, when quasiparticle corrections are considered, larger bandwidths (~1 eV) are found for the highest occupied molecular orbital (HOMO) and the lowest unoccupied molecular orbital (LUMO) in contrast with results using the local density approximation (LDA) only[11].

Transition from a Molecule to Crystalline Lattice

A single C_{60} molecule has discrete molecular energy levels as shown in Fig. 1.6. The highest occupied molecular orbital (HOMO) is formed by five filled degenerate states with h_u symmetry. The HOMO-1 is formed by two sets of states (nine individual states) with g_g and h_g symmetry that happen to be nearly degenerate in energy with one another. Transitioning to a crystalline structure, these discrete energy levels broaden into dispersive band manifolds as shown on the right side of Fig. 1.6.

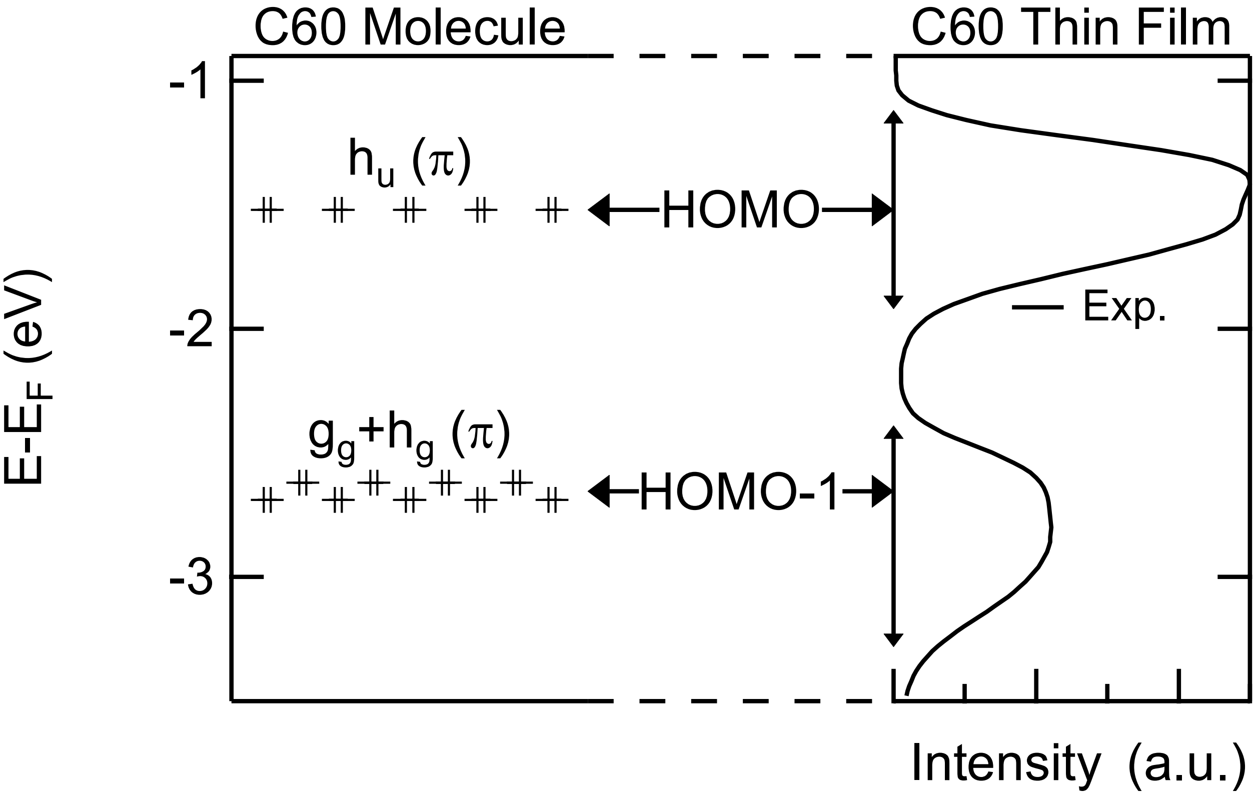

Figure 1.6: Transition from C_{60} molecular energy levels to crystalline band structure for the HOMO and HOMO-1. Experiment curve is obtained from integrated ARPES spectra of a 5 nm C_{60} thin film.

C_{60} Band Structure Calculations

Louie et al. [12] calculated the bulk C_{60} (Fm3 structure) HOMO band structure in 1993 using both an LDA and quasiparticle approach as shown in Fig. 1.7. They calculated a band gap of 2.15 eV in the quasiparticle case which is in better agreement with experimental values as compared with the LDA case. The band structure is qualitatively quite similar in both cases, but the quasiparticle-calculated band manifolds have a 30% larger band width hinting that the dispersion within C_{60}'s valence bands may be larger than the magnitudes calculated with LDA. In both cases the calculated band structure is qualitatively very similar. At Γ, the five degenerate energy levels (left side of Fig. 1.6) from a single buckyball are split to two separate bands by the bulk crystal field as shown in Fig. 1.7. The same is true for the L point, while the X point removes the degeneracy entirely to reveal five separate bands.

Louie et al. [12] also modified (broadened) their calculations to simulate experimental ARPES energy-distribution curves (EDCs) as shown in Fig. 1.8. The individual bands from their calculations (Fig. 1.7) are now simply shoulders (as opposed to well-defined peaks) in a broad intensity envelope for each EDC. Little dispersion is predicted for either of the

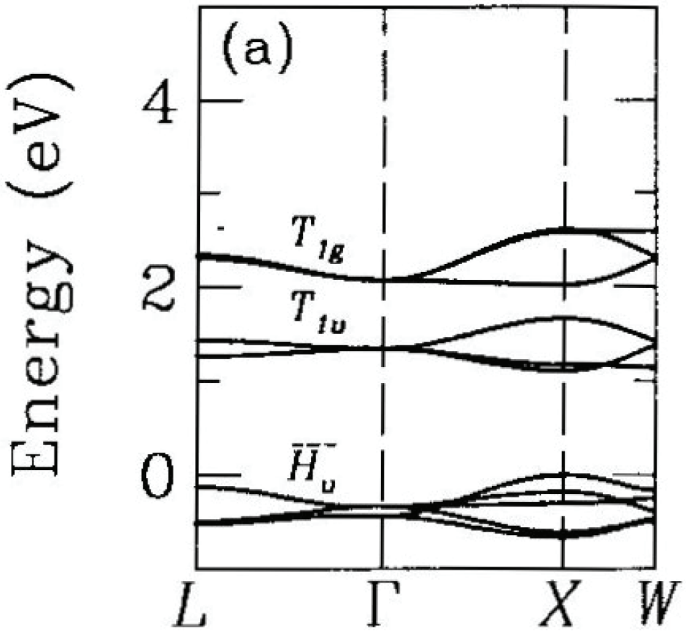

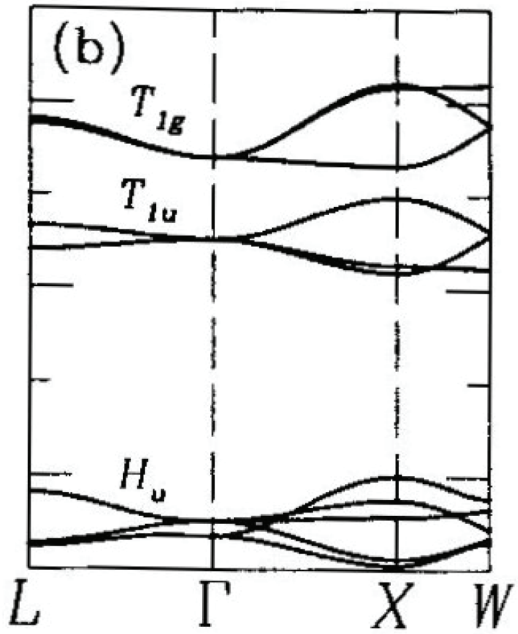

Figure 1.7: Calculated bulk C_{60} (Fm3 structure) HOMO, LUMO, and LUMO+1 band structure using **(a)** LDA and **(b)** a quasiparticle approach. Reprinted from Ref. [12], Copyright 1993, with permission from Elsevier.

high symmetry directions. (For reference, a comparison between the bulk and thin film high symmetry points is discussed in the previous section and shown in Fig. 1.5.) They attribute the intensity broadening to finite resolution effects, the multi-band nature of the band manifolds, orientational disorder, and integration over k_z. These are important considerations for the search to experimentally observe dispersive C_{60} bands. Luckily, finite resolution effects have become less impactful over time as instrumentation improves. The reduction of orientational disorder is a key topic in Chapter 5, where we discuss the observation of dispersive C_{60} bands.

Troullier et al. [5] calculated the band structure of a bulk fcc C_{60} crystal in the Fm3 structure with the energy levels at Γ shown in Table 1.1. They chose the Fm3 structure for their calculations as it maintains the highest symmetry possible for fcc C_{60} considering the possible rotation directions of the different buckyballs. They classify each state with an orbital character of either π, which are localized to surfaces just outside and inside the shell of the buckyball, or σ, which are localized to a surface on the buckyball. Due to the highly spherical nature of a C_{60} buckyball, the wave functions of the states can be additionally decomposed into spherical harmonics to determine n, the number of radial nodes plus one, and l, the dominant angular momentum. The σ states correspond to $n = 1$ as they do not have a radial surface node, while the π states correspond to $n = 2$ as they have one radial surface node at the surface of the buckyball. These are indicated by subscripts such as π_5

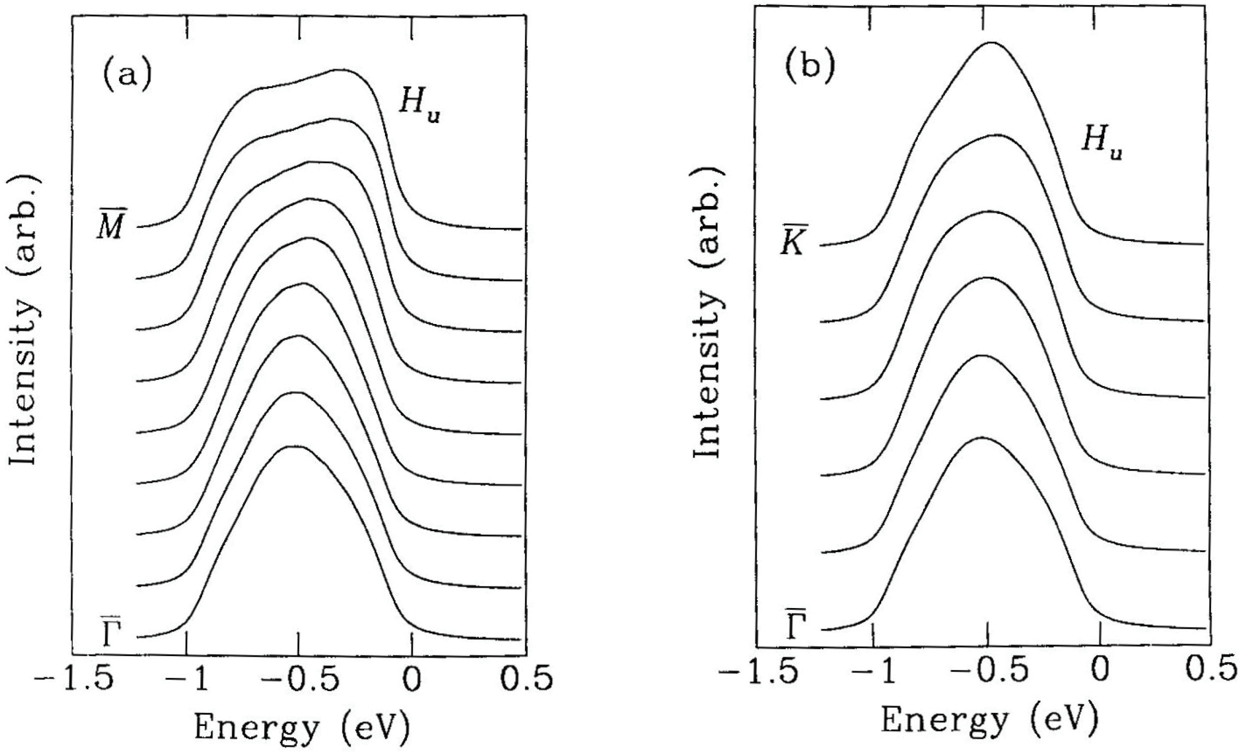

Figure 1.8: Simulated ARPES spectra for the C_{60} HOMO in the **(a)** $\Gamma - M$ and **(b)** $\Gamma - K$ directions. Reprinted from Ref. [12], Copyright 1993, with permission from Elsevier.

for the HOMO which has π orbital character with a dominant angular momentum number of $l = 5$. The highest energy occupied band manifold in bulk C_{60} is called the HOMO as it is formed by the highest occupied molecular orbital states from a single buckyball. In these calculations it is shown to have a π_5 orbital character, while the band manifold just below in energy, the HOMO-1 has a π_4 orbital character. Even lower in energy, the HOMO-2 has a mixed orbital character with states of π_3, σ_8, and σ_9 character.

Jalali-Asadabadi et al. [13] calculated the bulk fcc C_{60} band structure using a variety of modern density functional theory (DFT) methods in 2016. They found that the Tran and Blaha non-regular modified Becke and Johnson (TB-mBJ) method reproduces the experimental band gap of 2.12 eV while all others studied underestimate the band gap. They found the PBE-GGA+DFT-D3(vdW) method to produce the most accurate representation of the C_{60} band structure as shown in Fig. 1.9. The calculated band structure is quite similar to that calculated by Louie et al. (shown in Fig. 1.7) and finds the same number of nondegenerate HOMO bands at the Γ, X, and L points as in the earlier calculations. In general, across the HOMO and HOMO-1 there is an upper and lower cluster of bands with a crossing (or avoided crossing) nearly midway along the $\Gamma - X$ and $\Gamma - L$ directions. As will be discussed in Chapter 5, this bears a strong resemblance to the newly observed experimental C_{60} band

Energy (eV)	**Orbital Character**	**Band Manifold**
0.000	π_5-t_u	HOMO
-0.225	π_5-e_u	HOMO
-0.965	π_4-t_g	HOMO-1
-1.084	π_4-t_g	HOMO-1
-1.615	π_4-a_g	HOMO-1
-1.850	π_4-e_g	HOMO-1
-2.628	π_3-t_u	HOMO-2
-2.755	σ_9-t_u	HOMO-2
-2.766	σ_9-e_u	HOMO-2
-3.120	σ_8-t_g	HOMO-2
-3.189	σ_8-e_g	HOMO-2
-3.452	π_3-t_u	HOMO-2
-3.597	π_3-a_u	HOMO-2

Table 1.1: Calculated energies at Γ and orbital character of the first three bulk fcc (Fm3 structure) C_{60} valence band manifolds. Zero energy is set to the highest occupied state. Energies and orbital character from Ref. [5].

structure.

History of the Search for Dispersive C_{60} Band Structure

The first experiments on bulk C_{60} single crystals reported valence bands with band widths as large as 800 meV, yet with dispersions of no more than 50 meV for the HOMO and HOMO-1 band clusters, arguing that the small ratio between the band dispersion and the band width was due to transitions to excited vibrational states [9]. More recent high resolution ARPES experiments at low temperatures [14] reported non-dispersive HOMO and HOMO-1 bands ruling out effects of rotational disorder or lack of sufficient resolution in energy or momentum as factors hampering the observation of extended electronic states.

While bulk C_{60} single crystals prove difficult for photoemission experiments, the in situ deposition of crystalline layers of C_{60}, on the other hand, allows for a proper, well ordered and sufficiently conductive surface for photoemission experiments. Previous works on C_{60} (111) thin films deposited on GeS (001)[15, 16] show a weak dependence ($\sim$100 meV with an energy resolution of $\sim$100 meV) on the emission angle for the peaks in angle-resolved energy distribution curves (EDC: a curve of photoemission intensity vs. energy at a single momentum) corresponding to the center energy of each band cluster. Only by using low photon energies are larger changes with emission angle discernable and are interpreted as dispersive bands with the influence of vibronic loss structures[15]. A later study showed a more clear dependence of the band structure with emission angle, but again at low energies which are susceptible to strong final state effects[16] due to the relatively dispersive conduction bands near the Fermi level.

More recent measurements of C_{60} monolayers on Al (111) show the signature of some band dispersion at larger photon energies[17]. Other ARPES measurements of monolayers on Ag (100) and Ag (111)[18, 19] (which also allow for a convenient arrangement of the C_{60}

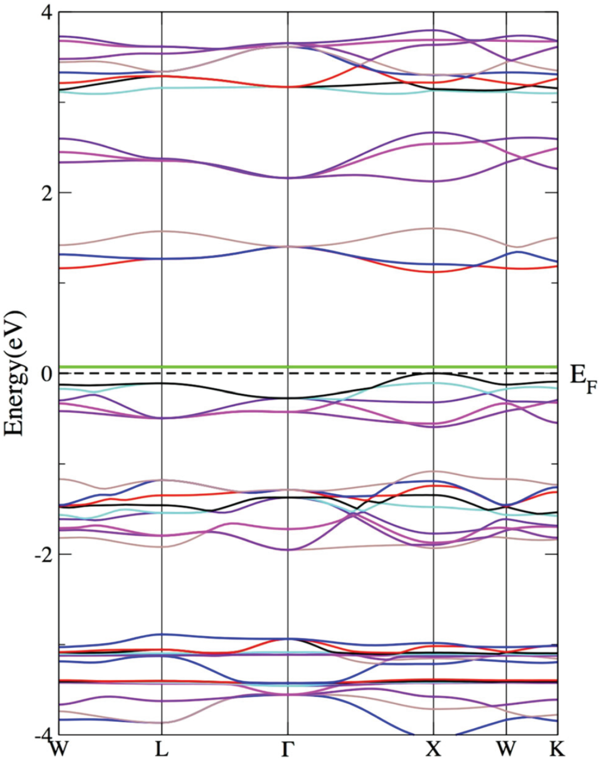

Figure 1.9: Band structure for the pristine fcc-C_{60} fullerite within PBE-GGA+DFT-D3(vdW). Fermi level is set to zero eV. Reprinted by permission from Springer Nature: Ref. [13], copyright 2016.

molecules) managed to observe a 100 meV dispersion of C_{60}'s lowest unoccupied molecular orbital (LUMO) band cluster by alkali doping, but no clear dispersion was observed for the HOMO bands[20]. More recent studies on thin film samples have reported larger dispersions of the band clusters, but the observed dispersions may have been affected by final state effects of dispersions in the conduction band. Dispersive features have been observed in the more heavily doped K_6C_{60} thin film[21] which has an ordering corresponding to the (110) direction of a bcc lattice (as opposed to the (111) direction of an fcc lattice for pure C_{60} thin films). The electronic band structure in such alkali-metal-doped C_{60} compounds is significantly different from the pure case as the conduction band in pure C_{60} is not observed to simply fill with incremental doping in a rigid-band picture, but instead an overall reconstruction of the band structure is observed[22]. The observation of dispersions of multiple individual bands within pure C_{60} band clusters has yet to be reported.

Despite a wealth of reports, the C_{60} experimental electronic valence band structure is still not fully understood. The experimental realization of dispersive C_{60} band structure is discussed in Chapter 5 and an in depth look in to its orbital character and unique photoemission properties is discussed in Chapter 6.

Thin Film C_{60} Applications

The unconventional zero-dimensional buckyball structure of C_{60} combined with strong electron-electron and electron-phonon interactions[18] in its bulk form allows for unique physics not seen in ordinary crystalline materials such as relatively high T_c superconductivity when doped with alkali metals (A_3C_{60}) and a non-continuous transition to an insulating phase (A_4C_{60})[23]. Thin film C_{60} is host to a litany of promising electronic device applications including photovoltaics[24], solar cells[25, 26], field-effect devices[27, 28], and interests in other fields such as astrophysics, where signature of the formation of C_{60} in the interstellar medium has returned as an active subject in recent years[29, 30, 31].

Chapter 2

Experimental Techniques

This chapter provides an overview of the experimental techniques mainly used throughout this work. The basic principles of angle-resolved photoemission spectroscopy (ARPES) are discussed as well as the advantages of a synchrotron-based light source for ARPES. Additionally, the basic principles of low-energy electron diffraction (LEED) are discussed as well as a method for calculating lattice constants from LEED data.

2.1 Angle-Resolved Photoemission Spectroscopy

Principle of ARPES

Angle-resolved photoemission spectroscopy (ARPES) is the ideal probe to observe a material's momentum-resolved electronic band structure. It builds on the basic principle of the photoelectric effect discovered by Hertz [32]—electrons are ejected from a material upon incidence of light in an energy-conserving process—but with the added benefit of a detector which can discriminate between different angles of photoelectron emission. This process conserves energy as well as in-plane momentum so we can recover the energy as

$$E_K = h\nu - \phi - E_B \tag{2.1}$$

for kinetic energy E_K, photon energy $h\nu$, work function ϕ, and binding energy (positive as equilibrium ARPES only probes occupied states) E_B. The in-plane momentum is then

$$k_\parallel = \frac{1}{\hbar}\sqrt{2m_e E_K}\sin(\theta) \tag{2.2}$$

for electron rest mass m_e and angle between sample normal and outgoing photoelectron θ. Out-of-plane momentum k_z (or $k_\perp$) is not conserved, however, due to the electron's interaction while exiting the symmetry-breaking sample surface [33]. At normal emission, the out-of-plane momentum is given by

$$k_z = \frac{1}{\hbar}\sqrt{2m_e(E_K + V_{in})} \tag{2.3}$$

for inner potential V_{in}. The inner potential for a three-dimensional material (i.e. a bulk crystal) can be determined with ARPES by examining the periodicity of the normal-emission band structure with a photon-energy scan. Electron bands with three-dimensional character must show a periodicity in k_z as a result of long-range crystalline order. Hence, the inner potential can be used as a fitting parameter which will have the material's proper value when the periodicity of the band structure is recovered. A photon-energy dependence not only reveals information about the bulk characteristics of a material's band structure, but can consequently be used to determine which features have a two-dimensional character as these features will show no dispersion (or periodicity) in k_z. This is particularly useful for differentiating between bulk and surface or interface states.

The actual intensities measured in an ARPES experiment are subject to (usually) significant intrinsic effects. A common model including intrinsic effects (many-body effects) takes the photoemission intensity as [34, 35]

$$I(k, E) = |M|^2 f(E) A(k, E) \tag{2.4}$$

for matrix element M determining the transition probability from initial to final state, single-particle spectral function A, and Fermi function f. Matrix elements effects ($|M|^2$) are commonly discussed when analyzing ARPES data as they directly affect (possibly with dramatic magnitude) the observed intensity and depend on both photon energy and polarization. The Fermi function must be included as ARPES is a probe of occupied states, but not unoccupied states. The single-particle spectral function can be expanded as [34, 35]

$$A(k, E) = \frac{1}{\pi} \frac{\Sigma''(k, E)}{(E - E^{\circ}(k) - \Sigma'(k, E))^2 + (\Sigma''(k, E))^2} \tag{2.5}$$

for self-energy $\Sigma(k, E) = \Sigma'(k, E) + i\Sigma''(k, E)$ which contains information on many-body effects in the system.

In addition to intrinsic effects, all ARPES data is susceptible to various extrinsic effects. One common and unavoidable (but sometimes reducible) effect is broadening due to finite energy and momentum resolution. The total energy resolution is taken as the root mean square of the light source energy resolution (dependent on photon energy and usually a tradeoff with flux) and the detector energy resolution (dependent on analyzer settings and usually a tradeoff with acquisition time). The momentum resolution ($\Delta k_{\parallel}$) is related to the angular resolution ($\Delta\theta$) by

$$\Delta k_{\parallel} \simeq \frac{1}{\hbar} \sqrt{2 m_e E_K} \cdot \cos\theta \cdot \Delta\theta \tag{2.6}$$

where the kinetic energy of the ejected electrons (E_K) is dependent on the incident photon energy [36]. Additionally, ARPES data is affected by an energy-dependent intensity background due to inelastically scattered electrons (photoelectrons that underwent inelastic collisions before exiting the sample).

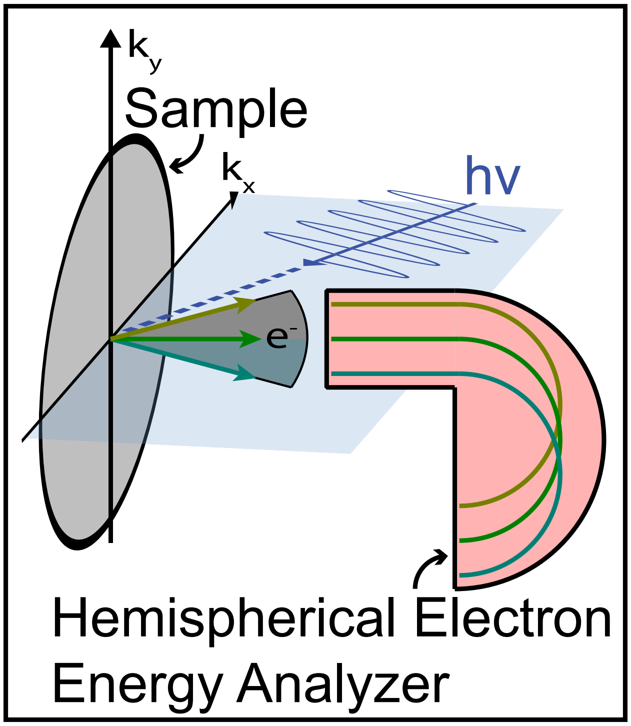

Figure 2.1: Typical experimental equilibrium ARPES setup.

A typical ARPES experiment commonly utilizes a hemispherical electron analyzer as shown in Fig. 2.1. As described previously, electron are ejected from the light-illuminated sample at various angles and energies. A certain angular and energy range (based on the experiment geometry and analyzer voltages) of photoelectrons enter the analyzer and are directed by electrostatic forces (created by applied voltages within the analyzer) until they hit a micro-channel plate (MCP) [34]. The photoelectrons follow a different path based on their exit angle and kinetic energy from the sample and hence when they hit the MCP, they can be separated physically in two dimensions—one for energy and one for angle. The MCP amplifies the signal of each photoelectron so that a charge-coupled device (CCD) can capture a two-dimensional image where intensity is proportional to the number of photoelectrons at a given angle and kinetic energy exiting from the sample.

Synchrotron-based ARPES

Synchrotron-based ARPES has significant differences when compared with laser-based ARPES. Most notably, a synchrotron allows for efficient switching over a wide range (10's or 100's of eV) of photon energies. It general provides higher photon energies overall when compared with laser-based ARPES which are typically more surface sensitive, but allow access to a wider momentum range, deeper energy range, and to core levels.

Semiconducting and insulating materials are prime candidates for sychrotron-based experiments as, by nature, they lack accessible states at the Fermi level so the energy range of states accessible by laser-based experiments is significantly reduced if not completely eliminated altogether. This is the primary reason why most of the data presented in this dissertation was taken using a synchrotron light source. Synchrotron light sources allow for a detailed determination of two-dimensional versus three-dimensional states thanks to their wide range of available photon energies. This is especially useful for our results on the bulk versus thin film properties of TMDs as will be discussed in Chapter 3 and our results on the thin film properties and unique photoemission intensity oscillations of C_{60} as will be discussed in Chapters 5 and 6.

2.2 Low-Energy Electron Diffraction

Principle of LEED

Low-energy electron diffraction (LEED) offers a precision in situ measurement of crystalline sample surface quality. LEED takes advantage of the regular spacing in crystalline lattices to produce diffraction spots and patterns which allow for a determination of sample quality, crystallinity, orientation, and lattice constant. LEED, as opposed to x-ray diffraction techniques, uses low-energy electrons which penetrate very little into the bulk of the sample, making it a highly surface-sensitive measurement [37].

The typical experimental setup of a LEED experiment is shown in Fig. 2.2. The crystalline sample is placed in front of an electron gun which directs a beam of (tunable) energized electrons towards the sample which are then backscattered onto a phosphor screen around the electron gun producing visible diffraction patterns based on the sample's crystal structure. A series of metal grids in front of the screen are set at certain electrostatic potentials to create an energy filter to remove inelastically scattered electrons [38]. We can relate the diffraction spot apparent distance from the center of the screen x with the angle between the incoming and outgoing electron θ by

$$\sin\theta = \frac{x}{Z_\circ} \tag{2.7}$$

for distance between sample and screen $Z_\circ$ and assuming the sample normal is aligned with the electron gun axis as shown in Fig. 2.2.

The basic principle determining the angle θ at which backscattered electrons constructively interfere is shown in Fig. 2.3. Electrons of a certain, but tunable, energy (and hence, wavelength λ) backscatter off of the lattice sites at an angle θ. The path length difference between backscattered electrons from neighboring sites is d. As shown by the geometry considerations, we can relate d to θ by

$$\sin\theta = \frac{d}{a} \tag{2.8}$$

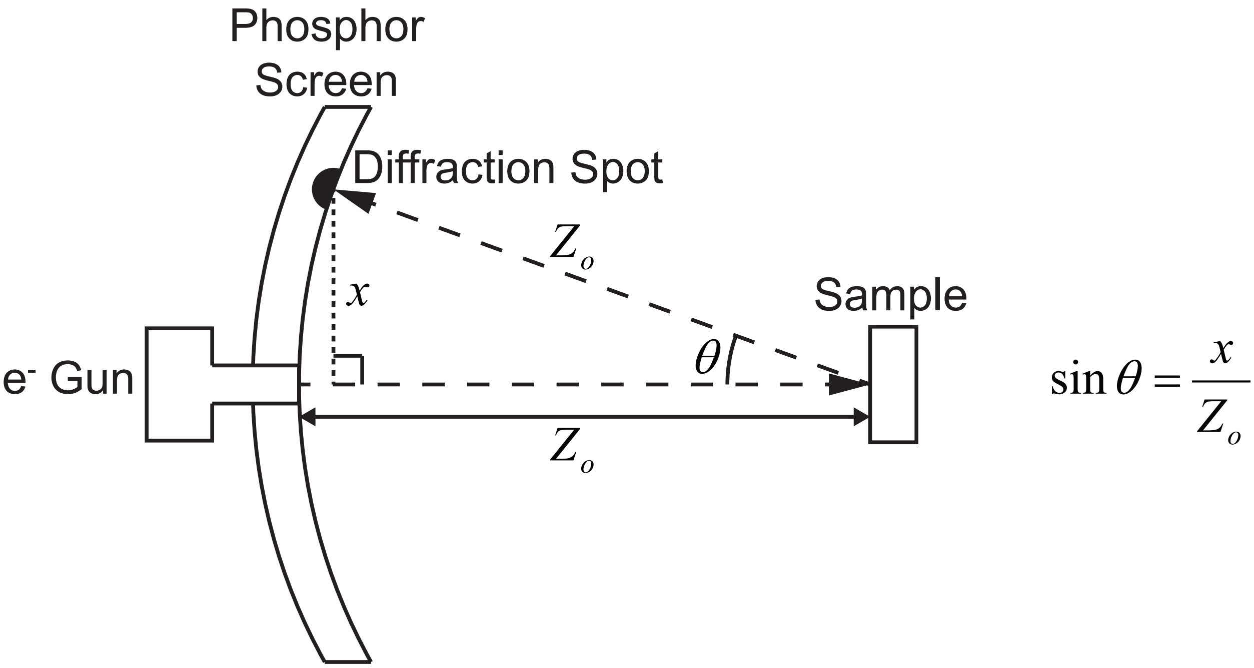

Figure 2.2: Typical experimental setup for low-energy electron diffraction (LEED) measurements: electrons from an electron gun are backscattered at an angle θ from a sample directly facing the electron gun and create diffraction spots on a phosphor screen (a distance $Z_\circ$ from the sample) which appear to be a distance x from the center.

For constructive interference to occur, the path length difference must be an integer multiple of the wavelength; i.e.

$$d = a \cdot \sin\theta = n\lambda \qquad \text{for some } n \in \mathbb{Z} \tag{2.9}$$

The integer n corresponds with the order of the diffraction spots (e.g. 1 is first order, 2 is second order, ...). We can relate the wavelength of an electron to its energy E (in eV) by [37]

$$\lambda = \frac{12.3}{\sqrt{E(\text{eV})}}\text{Å} \tag{2.10}$$

Lattice Constant Determination

In order to extract the lattice constant from the sample LEED pattern, we can combine Equations 2.7, 2.8, and 2.9 to get

$$a = \frac{(n\lambda)Z_\circ}{x} \tag{2.11}$$

If the sample to screen distance is not known, the lattice constant can still be determined by comparing with a reference pattern from a sample with a known lattice constant. Solving

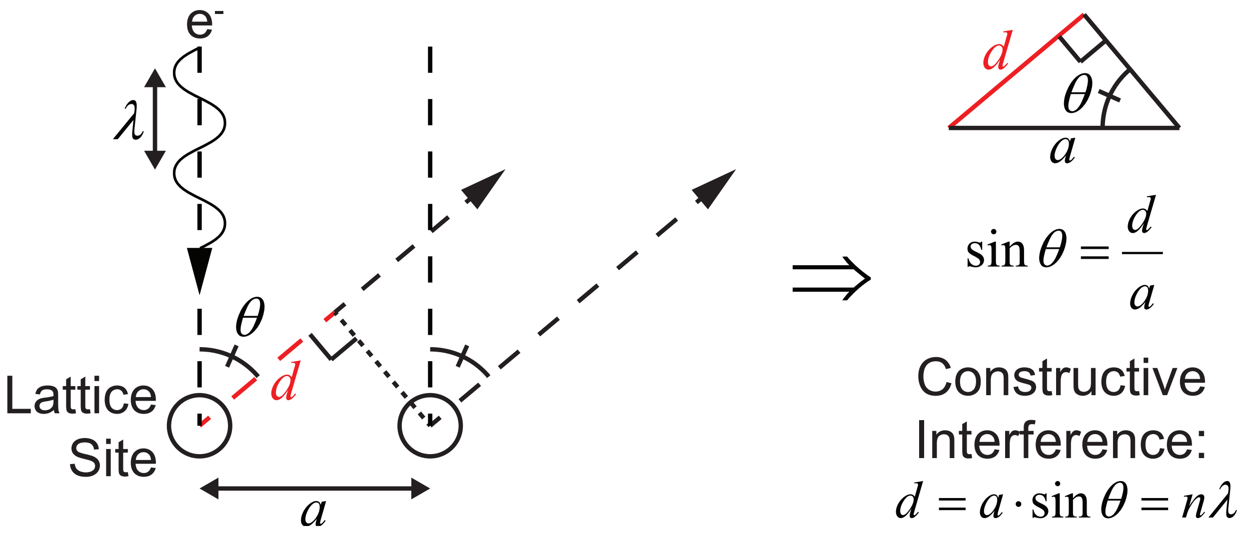

Figure 2.3: Basic principle of LEED: electrons backscatter off of lattice sites to create constructive interference diffraction spots at an angle θ depending on the wavelength of electrons λ and lattice constant a.

for $Z_\circ$ from a reference sample, we get

$$Z_\circ = \frac{a^{\text{ref}} x^{\text{ref}}}{n^{\text{ref}} \lambda^{\text{ref}}} \tag{2.12}$$

and plugging in to Equation 2.11, we get

$$a = \frac{(n\lambda) x^{\text{ref}}}{(n^{\text{ref}} \lambda^{\text{ref}}) x} \cdot a^{\text{ref}} \tag{2.13}$$

This is the method used in Chapter 5 to determine the C_{60} lattice constant from a Bi_2Se_3 reference.

Chapter 3

Spin-Orbit Coupling and Interlayer Interaction in Bulk Transition Metal Dichalcogenides

This chapter begins with an introduction to transition metal dichalcogenides (TMDs) including their structure, band gap, and the effect of strong spin-orbit coupling (SOC) on their unique spin- and valley-based physics. The origins of the valence band splitting in bulk TMDs (specifically MoS_2 and WS_2), the effects of SOC, the relationship between bulk and thin film TMDs, and the relationships between splitting, band gap, and molecular weight are discussed with ARPES data and supporting theory calculations. The majority of the figures and data for this chapter, other than the beginning introductory section, were reproduced with permission from Ref. [39], copyright 2015 by the American Physical Society.

3.1 Introduction to Transition Metal Dichalcogenides

Transition metal dichalcogenides (TMDs) (MX_2 where M = Mo or W and X = S, Se, or Te) are layered semiconducting materials that have been studied for decades and historically used a dry lubricant (as a result of their layered structure), but only recently have shown enhanced promise for application to a wide range of electronic devices, including the growing fields of spintronics and valleytronics [40].

Structure

The TMD layered structure, as shown in Fig. 3.1(a), makes them ideal for photoemission experiments as they are easily cleaved in situ to reveal a clean, flat surface. The bonding within each layer is covalent and hence much stronger than the van der Waals bonding between adjacent layers. For this reason, they exhibit a quasi-two-dimensional behavior even in the bulk limit [41]. The degree of this two-dimensional behavior in the bulk limit

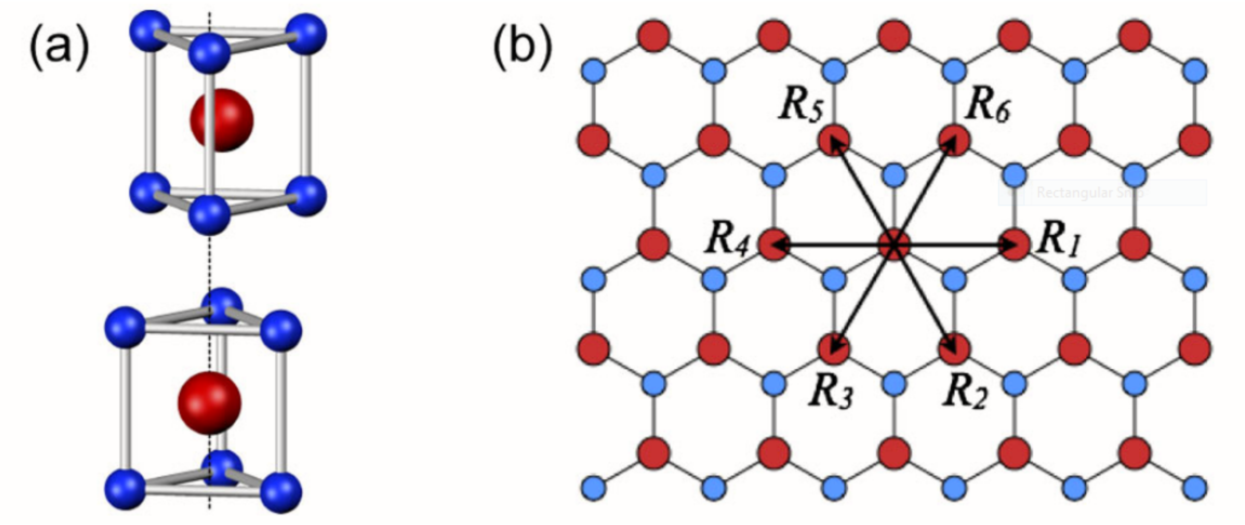

Figure 3.1: **(a)** The unit cell of bulk 2H-MoS2, which has the inversion center located in the middle plane. It contains two unit cells of MoS2 monolayers, which lacks an inversion center. **(b)** Top view of the MoS2 monolayer. R_i are the vectors connecting nearest Mo atoms. Reprinted figure with permission from Ref. [43]. Copyright 2012 by the American Physical Society.

is examined in Chapter 3. MoS_2 (and other TMDs such as WS_2) has a 2H phase at room temperature as shown in Fig. 3.1(a,b) where red corresponds to Mo and blue corresponds to S. The first Brillouin zone (BZ) of these 2H-TMDs is shown in Fig. 3.2. The reduced surface Brillouin zone is the same as the monolayer BZ where $\overline{\Gamma}$ is located at the center of the hexagonal BZ and the $\overline{\Gamma} - \overline{\mathrm{K}}$ distance is $4\pi/3a$ and the $\overline{\Gamma} - \overline{\mathrm{M}}$ distance is $2\sqrt{3}\pi/3a$ for lattice constant a (3.16 Å for MoS_2 and 3.15 Å for WS_2 [42]). For the remainder of this chapter, all high symmetry points are referring to the reduced surface/monolayer BZ, not the bulk BZ.

Thickness Dependent Band Gap Transition

2H-MoS_2 (and similar TMDs) has a bulk indirect band gap of ~ 1.2 eV and a larger direct gap of ~ 1.8 eV [44] as shown in Fig. 3.3(a) [45]. The indirect gap is between the valence band maximum (VBM) at Γ and the conduction band minimum (CBM) located near the midpoint between Γ and K. As the number of layers is reduced towards the monolayer limit as shown in panels (a–d), the VBM decreases in energy while the CBM increases. Finally, at the monolayer limit (and not before), the band gap switches from indirect to direct as the new VBM and CBM are both located at K as shown in Fig. 3.3(d). The main reason for these changes is that the bulk VBM and CBM bands have an orbital character that is strongly affected by interlayer interaction. The bands that make up the direct gap at K however, are derived from Mo d-orbitals [44] which are localized within the interior of each layer as Mo

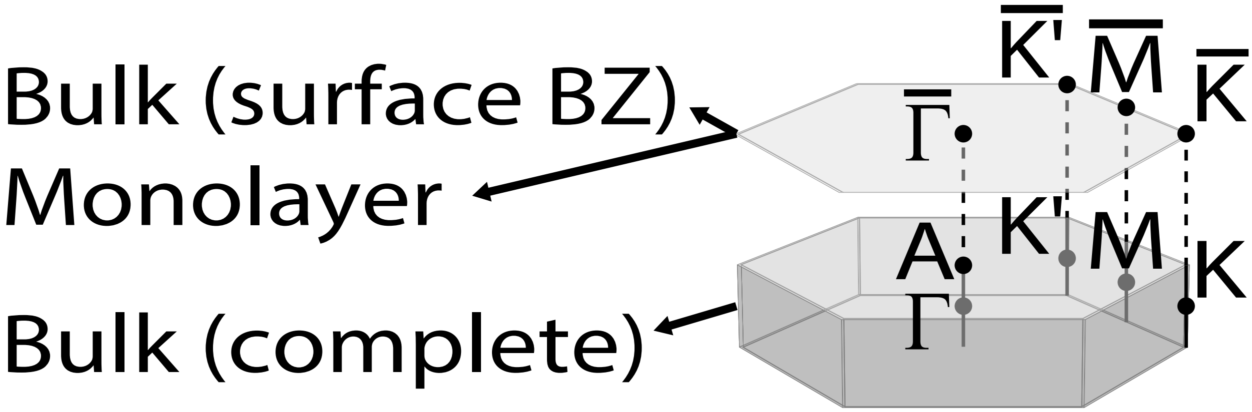

Figure 3.2: Top: 2H-TMD bulk reduced surface Brillouin zone (BZ) and monolayer BZ. Bottom: Full 2H-TMD bulk BZ.

atoms lie in the center of each layer unlike the S atoms which form both the top and bottom surface as shown in Fig. 3.1(a). As the Mo d-orbitals are localized within the layers, they lack significant interlayer interaction and the direct gap persists for all thicknesses. It only becomes the minimum gap for the monolayer case when the bands for the indirect gap are widened. The effects of interlayer interaction on the band structure in bulk TMDs will be elaborated in Chapter 3.

The change in the band gap from indirect to direct in the monolayer limit also accounts for the greatly enhanced photoluminescence seen in monolayer samples [45]. The energy of the monolayer TMD direct gap lies within the visible range which is one of the reasons for the strong interest with regards to TMD electronic device applications. Due to strong interest in recent years, monolayer TMD samples can now be readily obtained by mechanical exfoliation, chemical vapor deposition (CVD), and molecular beam epitaxy (MBE) [46].

SOC-Induced Spin- and Valley- Physics

In samples of all thicknesses, TMDs are theorized to have a split valence band as a result of strong spin-orbit coupling (SOC). The three K$'$ points are located adjacent or opposite to any of the three K points as shown in Fig. 3.2. K$'$ and K are inequivalent in the monolayer limit due to the breaking of inversion symmetry, but may also be inequivalent in the bulk due to local inversion symmetry breaking, distortions, or even defects. The magnitude of the valence band splitting is directly proportional to the strength of spin-orbit coupling. The overall spin-orbit coupling in TMDs is heavily influenced by the intrinsic atomic spin-orbit coupling which is largely dependent on atomic number. Hence, TMDs with heavier constituent atoms have a larger magnitude of splitting, especially when comparing the Mo- and W-based TMDs as will be elaborated at the end of Chapter 3.

The valence band splitting takes on a spin polarization as the samples are thinned to the monolayer limit. Bulk TMD structures have both time reversal symmetry and inversion

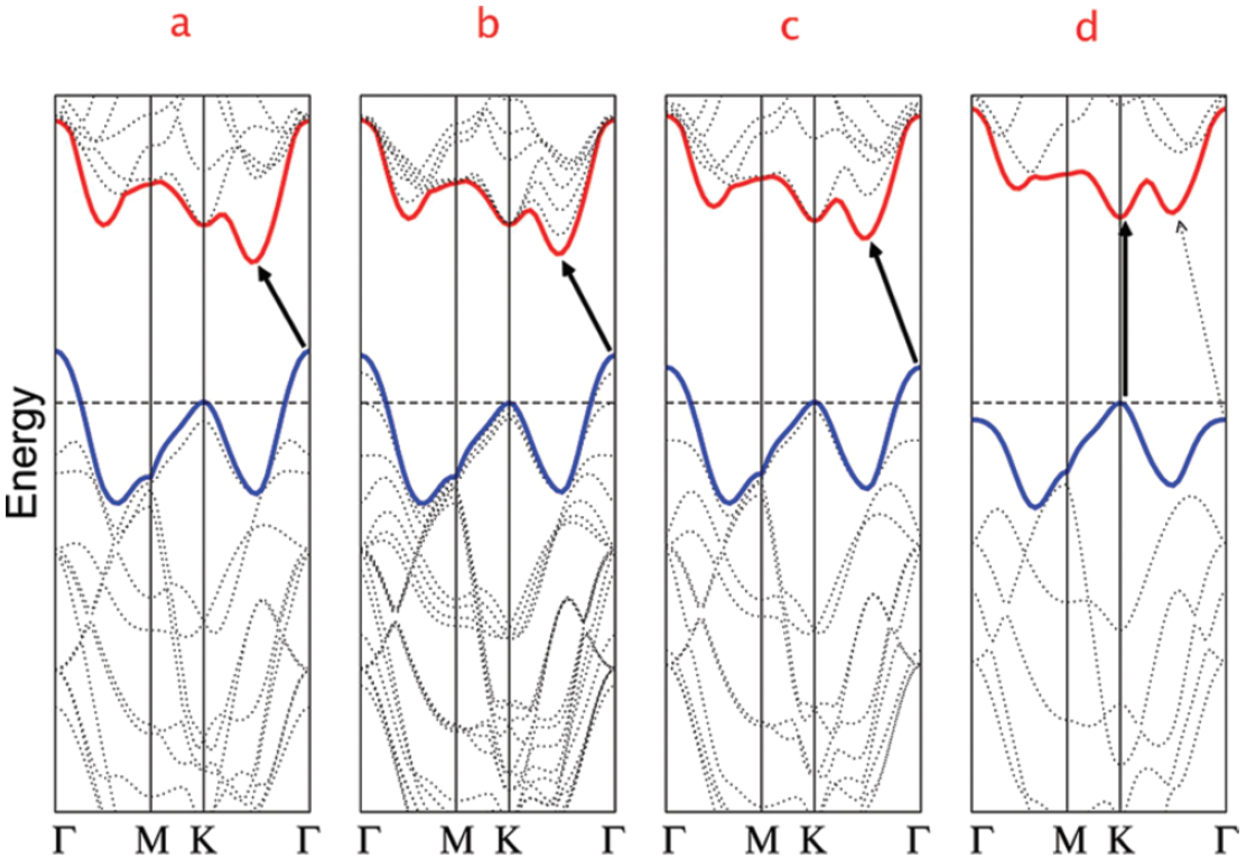

Figure 3.3: Calculated band structures of **(a)** bulk MoS2, **(b)** quadrilayer MoS2, **(c)** bilayer MoS2, and **(d)** monolayer MoS2. The solid arrows indicate the lowest energy transitions. Bulk MoS2 is characterized by an indirect bandgap. The direct excitonic transitions occur at high energies at K point. With reduced layer thickness, the indirect bandgap becomes larger, while the direct excitonic transition barely changes. For monolayer MoS2 in d, it becomes a direct bandgap semiconductor. This dramatic change of electronic structure in monolayer MoS2 can explain the observed jump in monolayer photoluminescence efficiency. Reprinted (adapted) with permission from Ref. [45]. Copyright 2010 American Chemical Society.

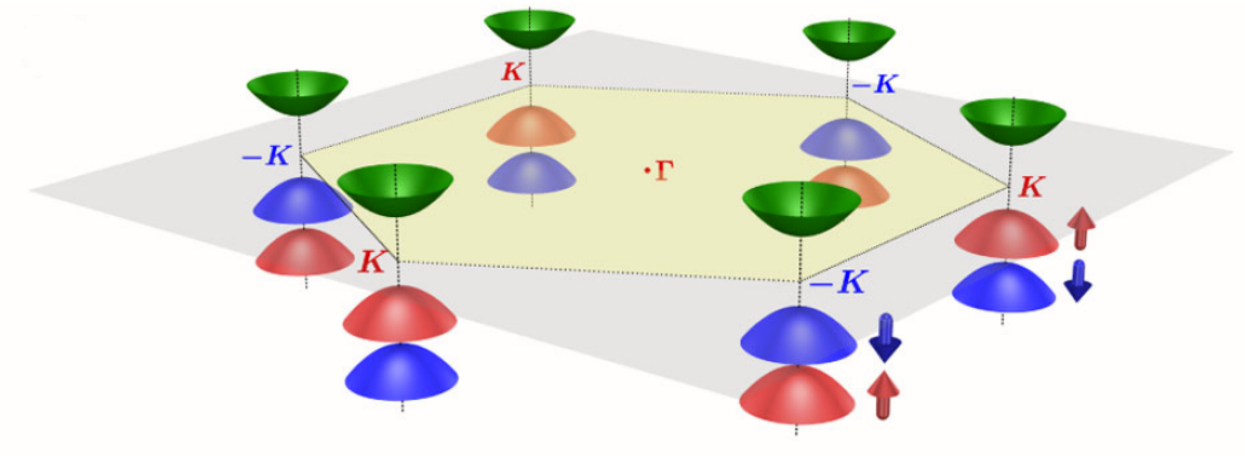

Figure 3.4: Schematic drawing of the band structure at the band edges located at the K points. Reprinted figure with permission from Ref. [43]. Copyright 2012 by the American Physical Society.

symmetry, but inversion symmetry is broken for a single layer structure as the inversion plane normally lies between two adjacent layers as can be deduced from the unit cell displayed in Fig. 3.1(a). This induces the split valence band to be nearly fully (out-of-plane) spin polarized [47, 44] near the K and K′ points of the hexagonal Brillouin zone as shown in Fig. 3.4. The spin polarization is predicted to be reversed between the K and K′ points, implying existence of an unusual spin-valley coupling in the TMDs. The ability to selectively populate[48, 43, 49] these valleys demonstrates their viability for use in spintronics and valleytronics devices. The different spin and valley combinations that can be created are shown in Fig. 3.5. Circularly polarized light of a specific handedness and energy will couple with different transitions. There are four possible combinations of spin- (up or down) and valley- (K or K′) number, all of which are accessible by tuning the incident light polarization and energy allowing for precise control of valley- and spin-polarization.

As a result of their physical structure, TMDs can be more easily stretched than other materials opening the door to strain-based tuning of their optical and electronic properties. In fact, MoS_2 can sustain folding, wrinkling, and a strain of up to 10% [42]. Strain can be achieved by a variety of techniques and is predicted to affect the band gap, VBM and CBM locations, and even create a semiconducting to metallic transition [50]. The effects of strain as it relates to the band gap and valence band splitting across the family of TMDs is elaborated on at the end of Chapter 3.

Despite the importance of the split valence band that governs the unique spin and valley physics of TMDs, there remain questions regarding the origin of these splittings in bulk TMDs. In particular, this splitting is theorized to be entirely a consequence of spin-orbit coupling in the monolayer limit, and a combination of spin-orbit coupling and interlayer interaction in the bulk limit, but there is disagreement[51, 52, 53, 54] about the relative

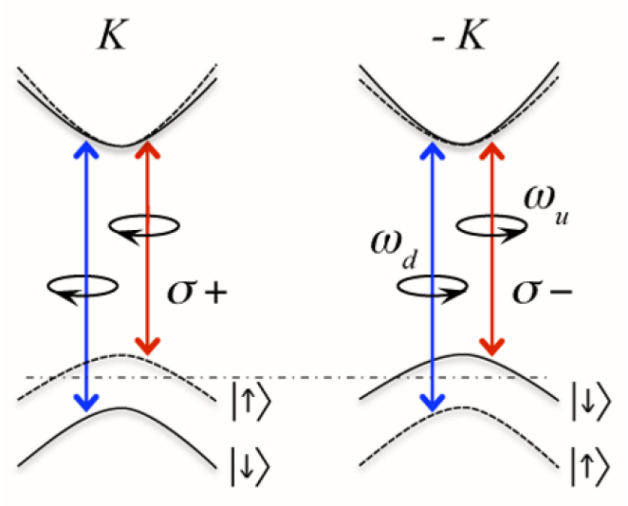

Figure 3.5: Valley and spin optical transition selection rules. Solid (dashed) curves denote bands with spin-down (-up) quantized along the out-of-plane direction. The splitting in the conduction band is exaggerated. ω_u and ω_d are, respectively, the transition frequencies from the two split valence-band tops to the conduction band bottom. Reprinted figure with permission from Ref. [43]. Copyright 2012 by the American Physical Society.

strength of the two mechanisms in the bulk limit. Current electronic band structure studies of bulk MoS_2[54, 55, 56, 57, 58, 59] and WS_2[51] are limited by energy and momentum resolution and lack focus on the valence band splittings. Experimentally, the sizes of the splittings have been characterized, but only with limited resolution.

Here we present high-resolution angle-resolved photoemission spectroscopy (ARPES) data of the electronic band structure of bulk MoS_2 and WS_2, and analyze our measurements via parallel first-principles computations. Our findings resolve previous debates on the role of interlayer interaction on the valence band splitting, revealing that the splitting in the bulk samples is primarily due to spin-orbit coupling and not interlayer interaction. In order to gain insight into the nature of this splitting, we further investigate its origins, its magnitude, and its correlation with the electronic band gap across a range of TMDs. Our comparisons for various TMDs reveal the interplay between the valence band splitting, band gap, molecular mass, and out-of-plane to in-plane lattice constant ratio, suggesting how specific TMDs would be suited for particular applications.

3.2 Methods

High-resolution ARPES experiments on MoS_2 (WS_2) were performed at Beamline 10.0.1.1 (4.0.3) of the Advanced Light Source at a temperature of 150 K using 50 eV (52-120 eV) photons. The total energy resolution was 10 meV (20 meV) for experiments on MoS_2 (WS_2)

with an angular resolution ($\Delta\theta$) of $\leq 0.2°$. The momentum resolution ($\Delta k_{\parallel}$) is related to the angular resolution by $\Delta k_{\parallel} \simeq \sqrt{2mE_k/\hbar^2} \cdot \cos\theta \cdot \Delta\theta$ where the kinetic energy of the ejected electrons (E_k) is dependent on the incident photon energy[36]. The samples were cleaved in situ at 150 K in a vacuum better than 5×10^{-11} Torr.

The electronic structures of MX_2 (M = Mo or W and X = S, Se, or Te) were computed using the projector augmented wave method[60, 61] as implemented in the VASP[62, 63, 64] package within the generalized gradient approximation (GGA)[65] scheme. A $15 \times 15 \times 3$ Monkhorst-Pack k-point mesh was used in the computations. We used experimental lattice constants and relaxed the atomic positions until the residual forces were less than 0.001 eV/Å. The spin-orbit coupling effects were included self-consistently. In order to correct the energy band gaps, we also performed calculations with the HSE hybrid functional[66, 67].

Single crystals were synthesized using the Br_2 vapor transport technique in a two-zone furnace system. Mo, W, and S powders (purity 99.9995%) were mixed in stoichiometric ratios in a sealed quartz tube at 1×10^{-7} Torr pressure and annealed to 880 °C for one week to yield precursor powders. Next, they were loaded into 2 inch diameter tubes with Br_2 liquid, pumped down to 1×10^{-7} Torr, and sealed. Typical growth parameters were established as heat up for one week from room temperature to 910 °C, the low temperature zone was set to 890 °C in one day, and the system was kept at this temperature for three weeks and controllably cooled down to room temperature in one week. Synthesized crystals displayed strong Raman signals at 384 cm^{-1} and 407 cm^{-1} for MoS_2, and 352 cm^{-1} and 417 cm^{-1} for WS_2. Lastly, monolayers exfoliated from MoS_2 and WS_2 crystals displayed sharp bright luminescence peaks at 1.88 eV and 2.04 eV, respectively.

3.3 Characterizing the Origins of the Splitting

Fig. 3.6(a) and 3.6(b) show detailed momentum-resolved constant-energy maps for bulk MoS_2 and WS_2, respectively. The two-dimensional (reduced in the k_z dimension as shown in the inset) hexagonal Brillouin zone is overlaid as white dashed lines. The observed suppression of intensity in MoS_2 along a specific momentum direction near $\overline{\Gamma}$ is due presumably to matrix element effects[68, 69, 70]. The evolution of the valence band about the $\overline{\Gamma}$, $\overline{\mathrm{K}}$, and $\overline{\mathrm{K}'}$ points can be clearly observed throughout the range of binding energies shown. We offset the two sets of data so that the valence band maximum at $\overline{\mathrm{K}}$ is shown at the same energy and we compare the two band structures as binding energy is increased. The two samples produce similar spectra with the most notable difference being the appearance of the lower split valence band at $\overline{\mathrm{K}}$ at approximately 170 meV below the local valence band maximum (VBM) for MoS_2. This appears as a small circular feature centered at $\overline{\mathrm{K}}$ within a larger concentric feature. The analogous splitting for WS_2 becomes apparent in the spectra at much higher binding energy, as seen in the map at 540 meV below the VBM. The splitting for both samples is shown by vertical white arrows. Trigonal warping of the valence band in the vicinity of the $\overline{\mathrm{K}}$ and $\overline{\mathrm{K}'}$ points, similar to that seen in other bulk TMDs[53, 59], is observed for both samples and presented here for the first time for bulk WS_2. This deviation

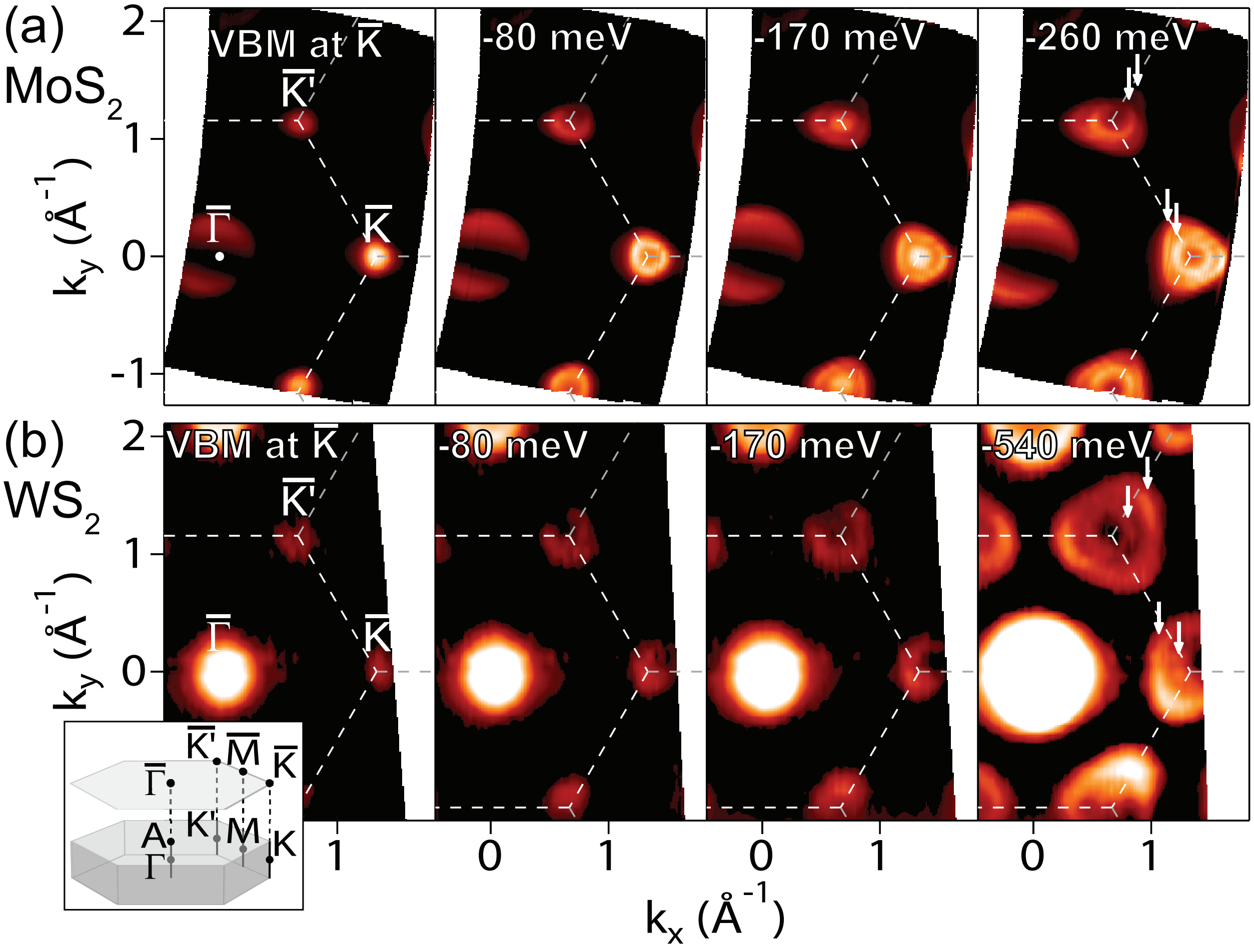

Figure 3.6: Constant energy maps of the electronic band structure of bulk **(a)** $\mathrm{MoS_2}$ and **(b)** $\mathrm{WS_2}$ taken at photon energies of 50 eV and 90 eV, respectively. The maps were taken at and below the energy corresponding to their respective valence band maximum (VBM) at $\overline{\mathrm{K}}$. The dashed white line indicates the two-dimensional (reduced in the k_z dimension as shown in the inset) hexagonal Brillouin zone. Evolution of the valence band with increase in binding energy about the $\overline{\Gamma}$, $\overline{\mathrm{K}}$, and $\overline{\mathrm{K}'}$ points can be observed for both samples. An energy splitting at the $\overline{\mathrm{K}}$ and $\overline{\mathrm{K}'}$ points can be observed in the $\mathrm{MoS_2}$ maps, most easily at 170 meV or 260 meV below the VBM (white arrows). The splitting for $\mathrm{WS_2}$ is not observed 170 meV below the VBM, but can be observed 540 meV below the VBM (white arrows). Trigonal warping of the valence band about the $\overline{\mathrm{K}}$ and $\overline{\mathrm{K}'}$ points can be observed for both samples.

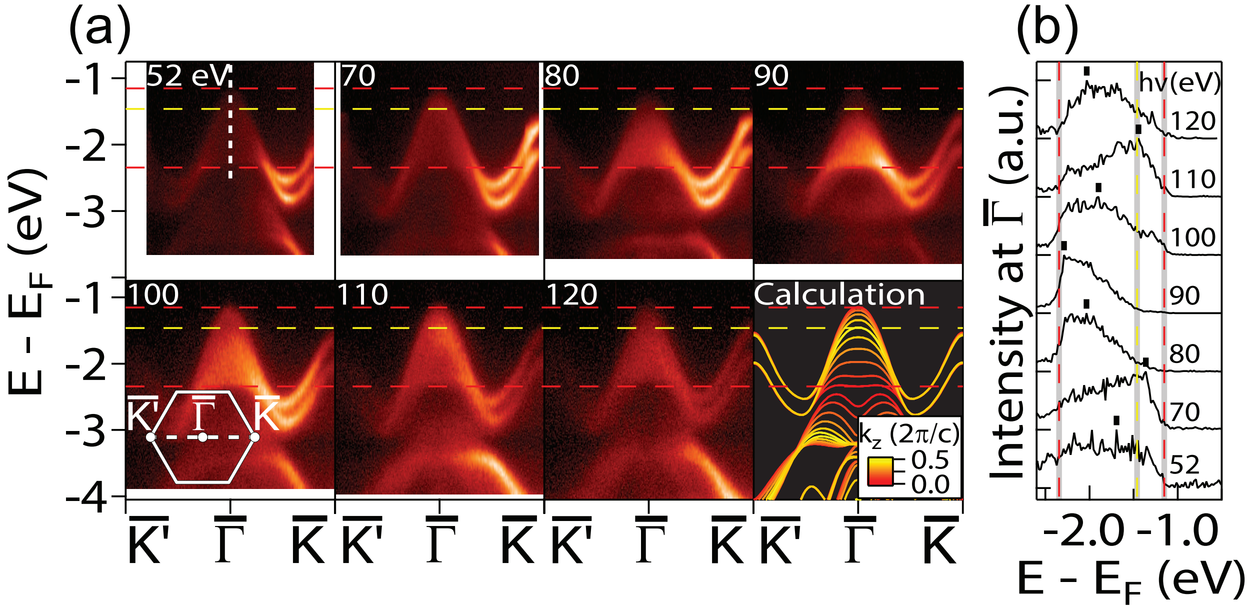

Figure 3.7: **(a)** Photon energy dependence from 52 to 120 eV and theoretical calculations of the electronic band structure of bulk WS_2 along the $\overline{\Gamma}$–$\overline{K}$ high symmetry direction. The horizontal red (yellow) dashed lines correspond to the calculated location of bulk WS_2 bands at the Γ point (A point). Observed intensity shifts of the valence band near the $\overline{\Gamma}$ point at different binding energies is evidence of strong k_z dispersion. **(b)** Energy distribution curves (EDCs) (solid black lines) taken along $k_x = k_y = 0$ Å^{-1} of the respective maps in (a) (e.g. along the white dashed line in the 52 eV map). The vertical red (yellow) dashed lines correspond to the calculated location of bulk WS_2 bands at the Γ point (A point). The peak in intensity (denoted by the tick marks) shifts periodically between higher and lower binding energies as a result of the strong k_z dispersion. Peaks in the 70 eV and 110 eV EDCs as well as the top of the feature in the 90 eV EDC correspond to the theoretical band maximum at A.

from a circular feature about $\overline{K}$ and $\overline{K'}$ is more pronounced at higher binding energies where the feature becomes more triangular. An analogous trigonal warping has been predicted[71, 72] to occur in monolayer MoS_2 samples as a consequence of the orbital structure of these bands and anisotropic (order q^3) corrections to the energy but has not been observed so far in an ARPES experiment.

To obtain information about the k_z dispersion, i.e. the interlayer dispersion, in Figure 3.7(a) we show detailed photon energy dependent maps compared with k_z-resolved theoretical calculations of bulk WS_2 along the $\overline{\Gamma}$–$\overline{K}$ high symmetry direction. Indeed, at normal emission ($k_\parallel = 0$), k_z is related to the kinetic energy of the ejected electrons (E_k) by $k_z = \sqrt{2m(E_k + V_{in})/\hbar^2}$ where V_{in} is the inner potential determined from the measured dispersion[73, 7]. Near $\overline{\Gamma}$, we observe a broad feature likely associated with the convolution of the various bands predicted for different k_z values as it extends between the two horizontal red dashed lines corresponding to the calculated energies of the top two valence bands at Γ ($k_z = 0$). The top of this broad feature aligns well with the calculated valence band maximum at Γ ($k_z = 0$) for the 52 eV map and as the photon energy is increased further, the top of the feature decreases in energy until it aligns with the calculated valence band maximum at the A point ($k_x = k_y = 0$, $k_z = \frac{\pi}{c}$) indicated by the horizontal yellow dashed line in the 90 eV map. Increasing the photon energy further returns the top of the valence band feature to its maximum value.

The observed k_z dispersion at $\overline{\Gamma}$ is investigated more closely in Fig. 3.7(b) by comparing energy distribution curves (EDCs) taken at $\overline{\Gamma}$ for each of the incident photon energies (e.g. along the dashed white line in the 52 eV image in (a)). The observation of a large spread in energy of the main peak in the EDC spectra between the calculated energies of the top two valence bands at Γ (vertical red dashed lines) is in agreement with the association of the broad feature near $\overline{\Gamma}$ with the convolution of multiple bands predicted for different k_z values. The peak intensity (tick mark) moves up and down in binding energy in a periodic manner confirming the strong k_z dependence of these bands. Overall, our observed k_z dispersions agree well with other predictions for WS_2[51] and our calculations which predict wide variation in binding energy (up to 880 meV) of the bands as k_z changes from 0 to $\frac{\pi}{c}$. Similar k_z dispersions are also found theoretically and experimentally more generally in TMDs[74, 75, 76, 77].

Near $\overline{\mathrm{K}}$, we observe the band splitting at the top of the valence bands for all photon energies, indicating that the splitting occurs for all corresponding k_z values. We measure the magnitude of the splitting to vary between 414 meV and 441 meV in accordance with our corresponding predicted range of 410 meV ($k_z = \frac{\pi}{c}$) to 466 meV ($k_z = 0$). This relatively small change in magnitude of the splitting (27 meV experimentally and 56 meV theoretically) across this range of photon energies indicates weak k_z dispersion near $\overline{\mathrm{K}}$ and $\overline{\mathrm{K}'}$. This is in contrast to the observation of large variations in the spectra of the broad feature at $\overline{\Gamma}$ which indicates strong k_z dispersion of the bands near $\overline{\Gamma}$.

As a result of the layered structure of bulk TMDs, the three-dimensional character of the band structure is directly related to the strength of the interlayer interaction. The strong k_z dispersion at $\overline{\Gamma}$ is a reflection of the three-dimensional character of those bands. However, the relatively weak k_z dispersion at $\overline{\mathrm{K}}$ and $\overline{\mathrm{K}'}$ is a reflection of the two-dimensional character of those bands and shows that interlayer interaction has a weak effect on the valence band splitting. Hence, we conclude that the splitting is dominated by spin-orbit coupling with interlayer interaction playing a minor role.

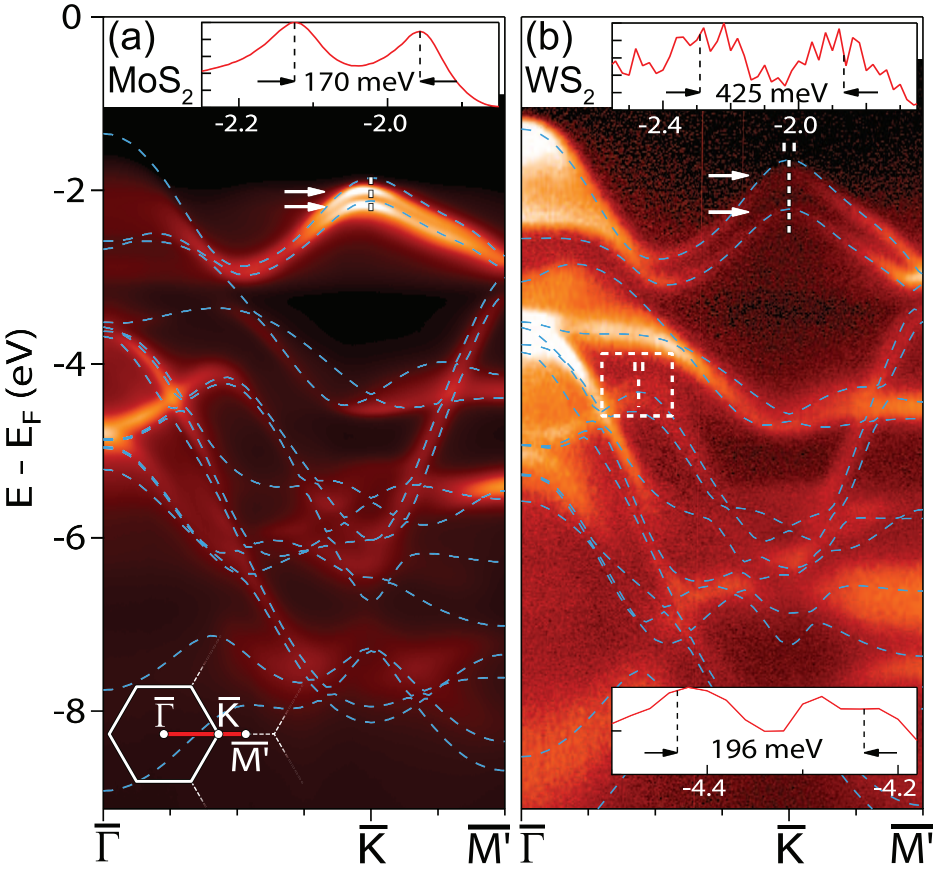

Figure 3.8: High resolution maps of the electronic band structure of bulk **(a)** MoS_2 and **(b)** WS_2 along the $\overline{\Gamma}$–$\overline{\mathrm{K}}$ high symmetry direction with theoretical calculations overlaid as dashed blue lines. Spin-orbit coupling and interlayer interaction induced splitting in the valence band near the $\overline{\mathrm{K}}$ point is fully resolved for both samples as indicated by the white arrows and the respective EDCs (upper insets) taken along the upper white dashed lines. [Here the WS_2 EDC was integrated in momentum between the two white tick marks.] The splitting is found to be approximately 170 ± 2 meV for MoS_2 and 425 ± 18 meV for WS_2. An additional splitting in a higher binding energy WS_2 valence band is observed within the white dashed rectangle in panel (b). The lower inset presents an EDC taken along the vertical white dashed line corresponding to the energy and momentum location of the maximum splitting of 196 ± 22 meV. [Here the EDC was integrated in momentum between the two white tick marks and smoothed with a Savitzky-Golay filter.] The calculated band structure is found to be in excellent agreement with the experimental band structure for both samples. The discrepancy in the location of the valence band near the $\overline{\Gamma}$ point for bulk MoS_2 can be attributed to its strong k_z dispersion.

3.4 The Effect of Spin-Orbit Coupling on the Valence Band Structure

Figure 3.8 shows high-resolution energy versus momentum maps of the band structure of bulk MoS_2 (panel a) and WS_2 (panel b). Band dispersions can be seen as far as 8 eV below the Fermi energy; many of these bands have not been observed before. The experimental band structure shows remarkable agreement with our theoretical predictions (blue dashed lines) throughout this energy and momentum region. The intensity of the valence band maximum near $\overline{\Gamma}$ for MoS_2 is reduced due presumably to matrix element effects[68, 69, 70]. Additionally, intensity of the experimental bands with low binding energy may be shifted near $\overline{\Gamma}$ due to their strong k_z dependence (as shown for WS_2 in Fig. 3.7). The splitting of the valence band at $\overline{\mathrm{K}}$ is fully resolved for both samples (as indicated by the white arrows) and is found to be 170 $\pm$ 2 meV for MoS_2 and 425 $\pm$ 18 meV for WS_2 (as shown in the upper insets). The value for MoS_2 agrees well with our experimental constant energy maps presented in Fig. 3.6(a) as the lower split band for MoS_2 appears 170 meV below the higher split band. The value for WS_2 is consistent with our experimental constant energy maps in Fig. 3.6(b) as the lower split band is not visible 170 meV below the higher split band, but is clearly visible 540 meV below. These measured magnitudes are smaller by approximately 100 meV than the values of 265 meV for MoS_2 and 570 meV for WS_2 predicted by HSE-based calculations. However, our experimental values agree very well with GGA-based calculations that predict a splitting of 145-224 meV for MoS_2 and 410-466 meV for WS_2 across all k_z values. The large difference in magnitude between the splittings for MoS_2 and WS_2 can be explained by the larger intrinsic spin-orbit coupling of tungsten compared with that of molybdenum. Additionally, our calculations predict a substantial splitting of a valence band of WS_2 at high binding energy (see white dashed rectangle). The maximum splitting predicted is in agreement with the experimental value of 196 $\pm$ 22 meV extracted from the EDC spectra (bottom inset) where two clear peaks can be distinguished. Similar to the splitting in the top valence band, we predict this band to be split largely due to spin-orbit coupling and only partially by interlayer interaction.

3.5 Relationship between Band Gap and Spin-Orbit Splitting

Figure 3.9(a) shows the magnitude of valence band splitting for bulk MoS_2, WS_2, and other bulk TMDs. The molybdenum- and tungsten-based TMDs are ordered separately from left to right with increasing molecular mass. For a given transition metal, the magnitude of the splitting increases as molecular mass increases. These trends are shown by the dashed lines and can be explained as a consequence of the larger intrinsic spin-orbit coupling of the successively heavier atoms. The same general trend is obtained from HSE hybrid functional calculations (triangles), although the splitting appears to be approximately 100 meV larger.

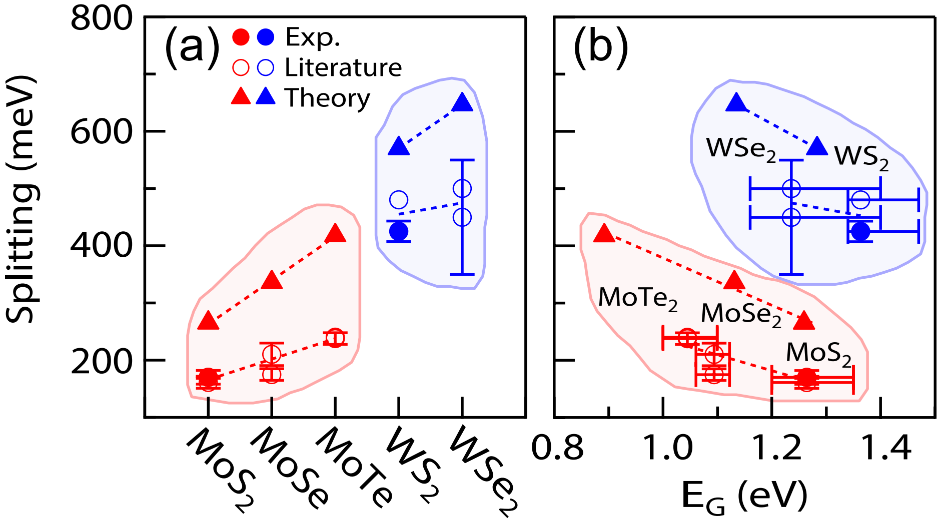

Figure 3.9: **(a)** Magnitude of valence band splitting at the $\overline{\mathrm{K}}$ point for bulk MoS_2[54, 74], $MoSe_2$[77, 74], $MoTe_2$[78, 74], WS_2[51], and WSe_2[79, 80]. **(b)** Magnitude of the splitting vs. band gap (E_G) for bulk MoS_2[81, 74, 82, 83], $MoSe_2$[81, 74, 84, 82, 83], $MoTe_2$[74, 83], WS_2[85, 81, 82], and WSe_2[81, 84, 86, 82]. The dashed lines are guides to the eye indicating the different trends for compounds containing molybdenum (red) and those containing tungsten (blue). The trends are further subdivided between experimental (circles) and theoretical (triangles) data. For all plots, filled (open) symbols represent data from this (other) work(s).

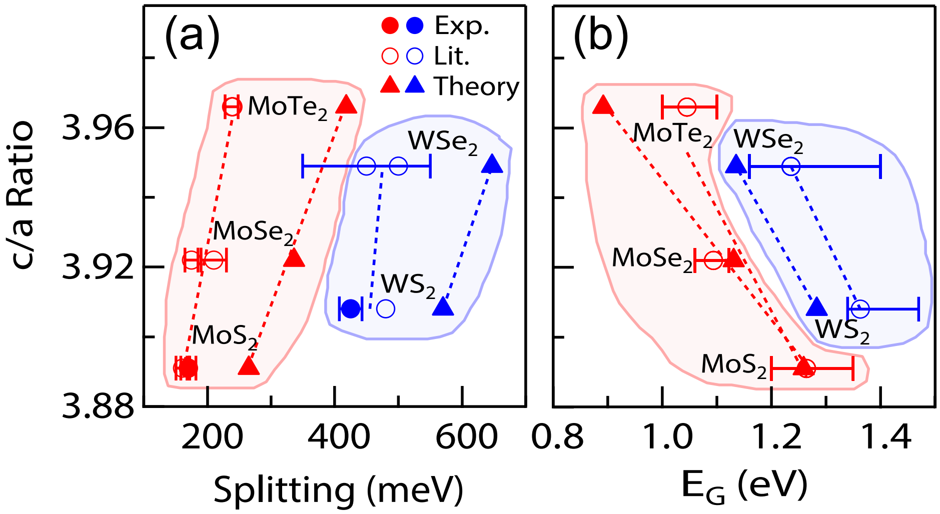

Figure 3.10: Ratio of out-of-plane to in-plane lattice constant ($\frac{c}{a}$)[74, 87] vs. **(a)** magnitude of valence band splitting and **(b)** band gap. See Fig. 3.9 for details on legend and references.

Figure 3.10(a) shows the ratio of out-of-plane to in-plane lattice constant ($\frac{c}{a}$) versus the magnitude of valence band splitting. Similar to the molecular mass trend, we observe that for a given transition metal, the magnitude of splitting increases with increasing $\frac{c}{a}$ ratio; however, our calculations indicate that although this trend holds across a range of TMDs, it does not hold for individual TMDs.

In addition to the valence band splitting, the band gap plays a key role when considering TMDs for use in spintronics/valleytronics devices. Figure 3.9(b) shows the magnitude of valence band splitting versus band gap (E_G) for bulk MoS_2, WS_2, and other bulk TMDs. For a given transition metal, the band gap of bulk TMDs decreases with increasing valence band splitting. The same trend is observed as a function of molecular mass in that the band gap decreases with increasing molecular mass. Again, this trend is seen for both experimental and theoretical data even though the magnitude of the splitting for each TMD is calculated to be approximately 100 meV larger than the corresponding experimental values. Figure 3.10(b) shows the ratio of out-of-plane to in-plane lattice constant versus band gap. It too follows the same trend as molecular mass and valence band splitting in that the band gap decreases with increasing $\frac{c}{a}$ ratio. This strong relationship between the band gap, the valence band splitting, and $\frac{c}{a}$ ratio would help guide the search for suitable TMDs targeted at specific applications.

3.6 Conclusions

We have presented in-depth high-resolution ARPES studies of the electronic band structure of bulk MoS_2 and WS_2 together with detailed first-principles computations. We have shown that the valence band splitting in bulk WS_2 is primarily due to spin-orbit coupling and not interlayer interaction, resolving previous debates on their relative role. These results strengthen the connection between bulk and monolayer TMDs as the splitting in the monolayer limit is due entirely to spin-orbit coupling. We have shown how the magnitude of this splitting changes for various TMDs and how it correlates with molecular mass, $\frac{c}{a}$ ratio, and band gap. These results provide important new information on how to control these parameters in TMDs and for the development of TMD-based devices in the fields of spintronics and valleytronics.

Chapter 4

Growth of High-Quality C_{60} Thin Films

This chapter gives an overview of both historical and modern C_{60} thin film growth on various substrates. Specific focus is given to growth on the strong spin-orbit coupling substrate transition metal dichalcogenide MoS_2. This is followed by a transition to growth on a novel substrate also with strong spin-orbit coupling, Bi_2Se_3, which is the type of sample studied in Chapters 5 and 6.

4.1 History

Different substrates have been reported in the past for the epitaxial growth of C_{60} thin films [88] including GaAs(110)[89], mica(001)[90], GeS(001)[91], and GaSe(001)[92]. These substrates all have in common a small lattice mismatch with bulk fcc C_{60}. Thick epitaxial films with coverage over millimiter square areas have been reported on substrates where the mismatch is minimized, as it is for GeS(001). In this lamellar substrate, C_{60} clusters along the fcc ($\bar{1}$,0,1) direction align along the a-axis of GeS. The separation of the C_{60} molecules is about twice the a-axis length of GeS (with a small mismatch of $\sim$0.75%). Despite lacking hexagonal surface symmetry, GeS was considered to be most likely one of the best possible lamellar substrates for epitaxial growth of C_{60}[91].

4.2 Modern Growth Process for High Quality C_{60} Thin Films

High quality C_{60} can be grown on a variety of thin film and bulk substrates. For thin film substrates, the growth process is began by annealing (temperature is sample-dependent) the substrate in situ under ultra-high vacuum (UHV, $\sim 10^{-10}$ Torr) to clean the surface. For bulk substrates, the growth process is began by first cleaving a bulk substrate in situ under UHV to reveal a clean, flat surface. Substrate quality is then confirmed by LEED measurements. The substrate is slowly heated to approximately 150 °C, while an effusion cell loaded with high purity (99.9%) C_{60} powder is slowly heated above 300 °C. Ideally the effusion cell is degassed the night before (at ∼200 °C) to reduce the pressure in the vacuum chamber during deposition. Deposition is started when a quartz crystal oscillator thickness monitor begins reading a steady deposition rate usually around 350 °C (at $\sim 1 \times 10^{-9}$ Torr). The shutter is closed when the desired thickness is reached. The substrate is heated during (and after if desired for ∼ 20 min.) the deposition to facilitate the arrangement of large crystalline domains through increased C_{60} mobility. Sample quality is then confirmed by LEED measurements.

4.3 Example of High Quality Growth on a Device-Ready Heterostructure

We have used the method described in Section 4.2 to grow a high quality C_{60} film on a heterostructure suitable for electronic device applications as reported in Ref. [27]. To first test the quality and crystallinity of the samples, 15 nm of C_{60} was deposited at 1.4×10^{-10} Torr on suspended graphene in preparation for transmission electron microscopy (TEM) measurements. The TEM images shown in Fig. 4.1(a) show evidence of a high quality C_{60} film with grain sizes up to 200 nm. The hexagonal lattice pattern of the C_{60} film is easily observed in the inset zoomed image.

Having shown that high quality C_{60} films were attainable using this method, the next step was to deposit C_{60} on a electronic device structure. A graphene/hexagonal boron nitride (h-BN) device was first fabricated and tested using electronic transport measurements before depositing a 50 nm C_{60} film in situ under UHV and at a substrate temperature of 156 °C, effusion cell temperature of 332 °C, and at a rate of 0.1 Å/s. The full device structure is shown in Fig. 4.1(b).

C_{60} is known to be an excellent electron acceptor [93] and hence is inherently attractive for the many electronic device applications making use of such a property for charge transfer, charge separation, and adjustment of charge carrier density. To this end, Ojeda-Aristizabal et al. [27] carried out charge transfer calculations for representative C_{60}/graphene and C_{60}/graphene/h-BN heterostructures. First-principles DFT simulations were used to calculate the magnitude and sign (blue for positive charge, red for negative) of the charge transfer within these heterostructures as shown in Fig. 4.2. As shown in panel (a), there is appreciable charge transfer of electrons from the graphene layer into the C_{60} layer leaving the graphene hole-doped for the C_{60}/graphene heterostructure. For the case of the C_{60}/graphene/h-BN heterostructure shown in panel (b), there is the same qualitative effect found with the C_{60} accepting electrons from the graphene layer, but remarkably the magnitude of which is reduced by about one full order of magnitude. This was found to be a surprising result as h-BN was previously regarded to be an excellent non-interacting sub-

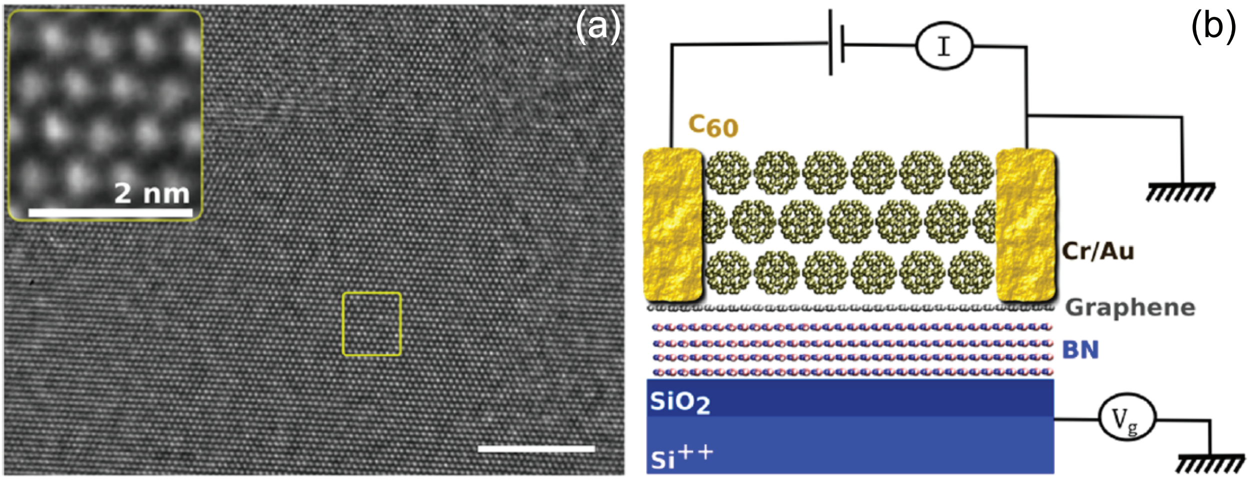

Figure 4.1: **(a)** TEM image of a ∼15 nm thick C_{60} film deposited on suspended graphene under UHV conditions. High crystallinity is clearly observed (scale bar 10 nm). The inset is a blow-up of the region outlined by the yellow box and highlights the close-packed structure of the C_{60}s (bright dots correspond to the projected lattice images of the C_{60} molecular columns). **(b)** Schematic representation of C_{60}/graphene/h-BN device used for transport measurements. The device can be electrically probed prior to, and after, C_{60} deposition. Reprinted (adapted) with permission from Ref. [27]. Copyright 2017 American Chemical Society.

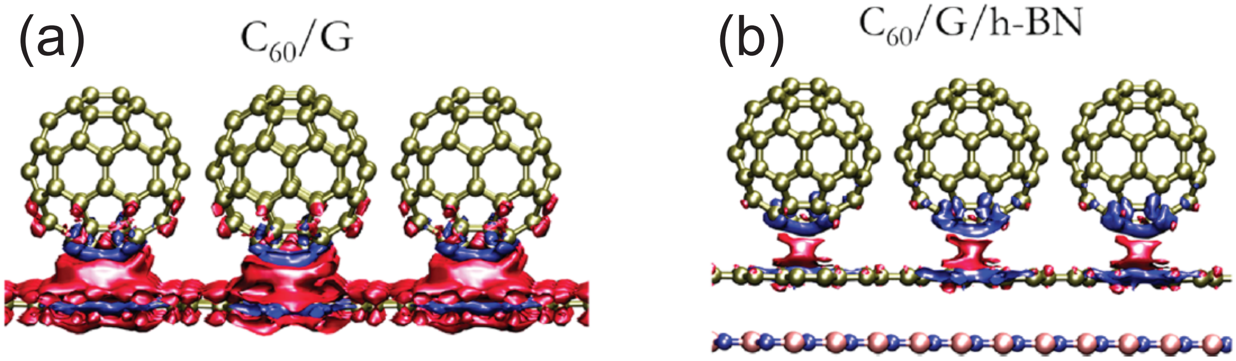

Figure 4.2: **(a)** Charge difference density for C_{60}/graphene. **(b)** Charge difference density for C_{60}/graphene/h-BN. Blue and red isosurfaces represent positive and negative charges, respectively. Reprinted (adapted) with permission from Ref. [27]. Copyright 2017 American Chemical Society.

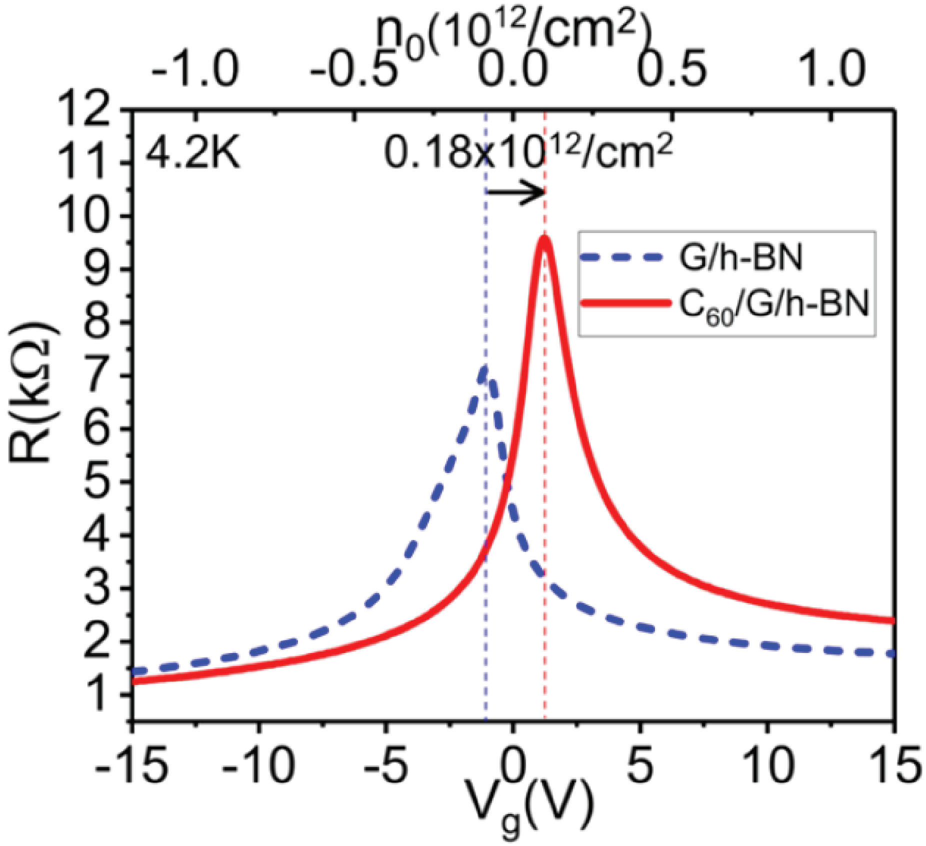

Figure 4.3: Gate voltage dependence of the resistance of graphene/h-BN devices before (dotted line, blue) and after (solid line, red) deposition of 15 nm high crystallinity C_{60}. Samples are measured at 4.2 K. Shift of peak to the right indicates hole doping of the graphene by the C_{60}. Reprinted (adapted) with permission from Ref. [27]. Copyright 2017 American Chemical Society.

strate for graphene showing similar characteristics as suspended graphene [94]. Clearly, in this case the h-BN layer has a significant impact on the characteristics of this graphene-based device.

In order to experimentally test the characteristics of the graphene-based device, transport measurements were carried out before and after the C_{60} deposition. The results of which are shown in Fig. 4.3 as resistance versus gate voltage curves taken at 4.2 K. In accord with the DFT charge transfer predictions, the C_{60} film accepts electrons from the graphene layer for a charge transfer of 0.2×10^{12} cm $^{-2}$ as shown by the shift of the peak when comparing the two curves.

In summary, high quality C_{60} thin films have been proven to be attainable using our method described above. Their structure and charge transfer properties lends themselves well to electronic device applications such as in this case of a C_{60}/graphene heterostructure.

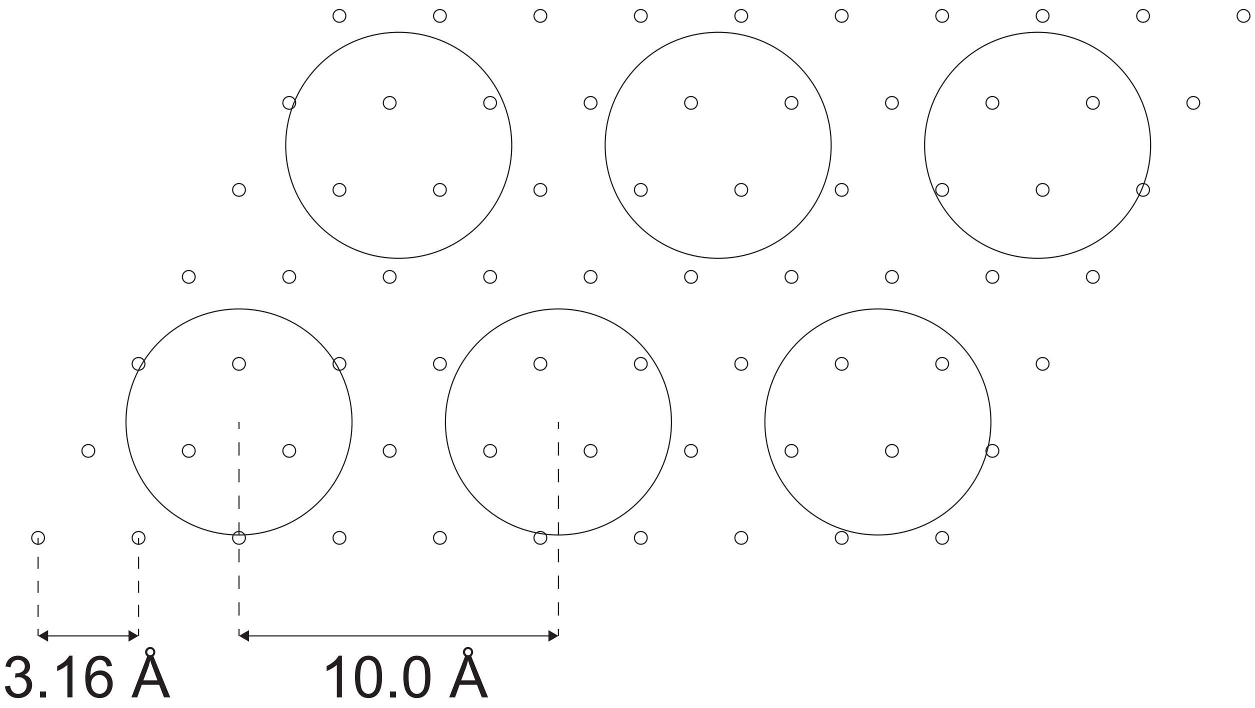

Figure 4.4: The alignment of a C_{60} thin film (large circles) on the sulfur atom surface of MoS_2 (small circles) as reported by Sakurai et al. [95].

4.4 Growth on TMDs (MoS_2)

History

Growth of high quality C_{60} thin films on TMDs was reported as early as 1991 for MoS_2 [95]. They performed their depositions in a molecular beam epitaxy (MBE) chamber with a base pressure of 7.5×10^{-10} Torr. The bulk MoS_2 substrate was cleaved in air before being loaded into the chamber and subsequently annealed at 200 °C in UHV for a time to clean the surface before being returned to room temperature. Purified C_{60} powder (although containing up to 15% C_{70}) was heated to 240 °C in a Knudsen cell and deposited onto the (room temperature) MoS_2.

Sakurai et al. found epitaxial growth of their C_{60} film on MoS_2 based on their reflection high-energy electron diffraction (RHEED) measurements. Comparing the diffraction patterns of C_{60} and MoS_2, they deduced that the C_{60} monolayer lattice constant was approximately 3.18 times as large as that of the MoS_2 surface. Hence, they concluded that the C_{60} lattice constant was approximately 10.0 Å (given a 3.16 Å lattice constant of MoS_2). This is expected as it corresponds to the nearest neighbor distance in the (111) layers of bulk C_{60} ($10.0\ \text{Å} = \frac{14.2\ \text{Å}}{\sqrt{2}}$, where $a_{\text{Bulk C60}} = 14.2$ Å [5]). Their proposed arrangement of C_{60} on MoS_2 is shown in Fig. 4.4. They found perfect azimuthal alignment of the C_{60} film with the

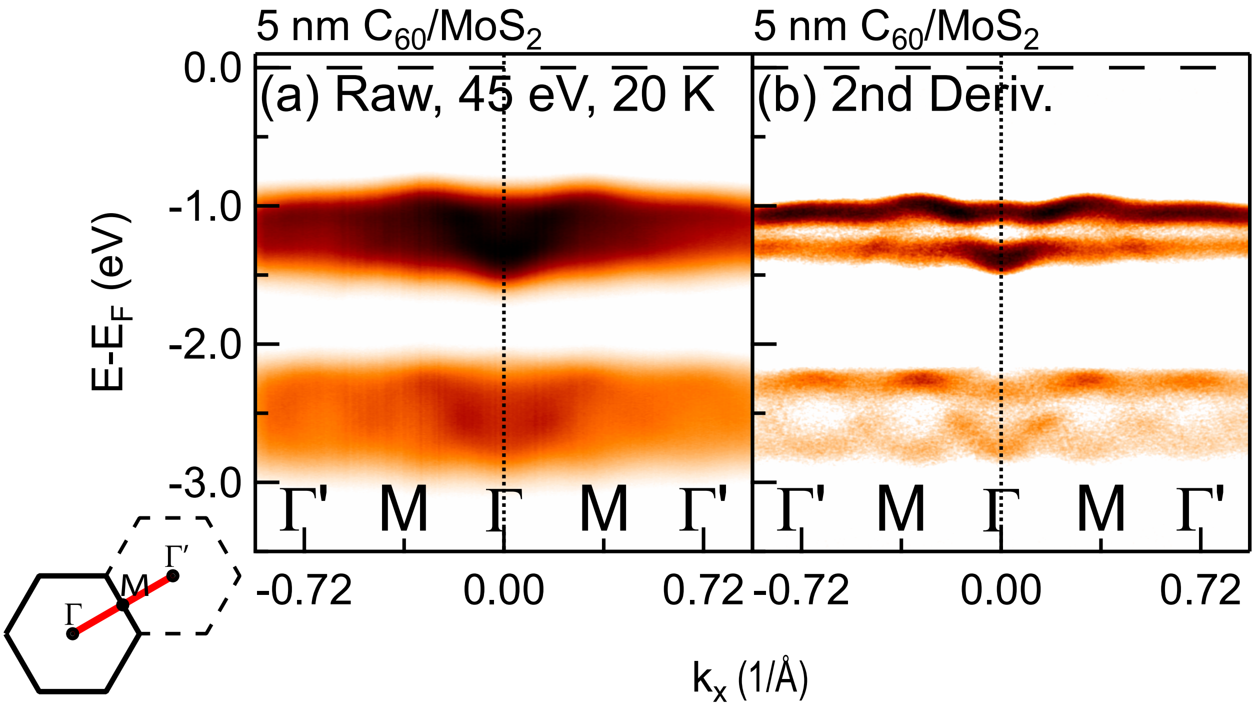

Figure 4.5: **(a)** Raw energy vs. momentum along $\Gamma - \mathrm{M}$ for a 5 nm C_{60} film on bulk MoS_2. **(b)** Second derivative in the energy dimension of the data in (a). Data taken with 45 eV photons and at 20 K.

MoS_2 surface based on their RHEED measurements (i.e. the in-plane lattice vectors for the thin film substrate are aligned), but otherwise make no claim as to the translational position of the buckyballs with regards to the sulfur atom surface. They conclude that the weak van der Waals forces between the film and substrate imposes negligible strain on the C_{60} film even with the large lattice constant mismatch between thin film and substrate.

High Quality Growth on MoS_2

We have grown high quality C_{60} thin films on MoS_2 using the modern C_{60} growth process as detailed previously in Section 4.2. Fig. 4.5 shows ARPES data from a 5 nm thick C_{60} film on a bulk MoS_2 substrate. Dispersions can be observed in the raw ARPES data (panel (a)) in both the HOMO and HOMO-1 along the $\Gamma - \mathrm{M}$ direction. There is a prominent band minimum at Γ and maximum at M for both of the band manifolds. Sinusoid-shaped dispersions across a wide momentum range are easily observed in the HOMO-1. The second derivative of the data in the energy dimension more precisely locates the dispersions within the band manifolds as shown in panel (b). There appears to be a prominent avoided crossing at the center energy of the HOMO and possibly a similar, but less prominent feature in the HOMO-1. Multiple dispersive bands are now easily observed within each of the band

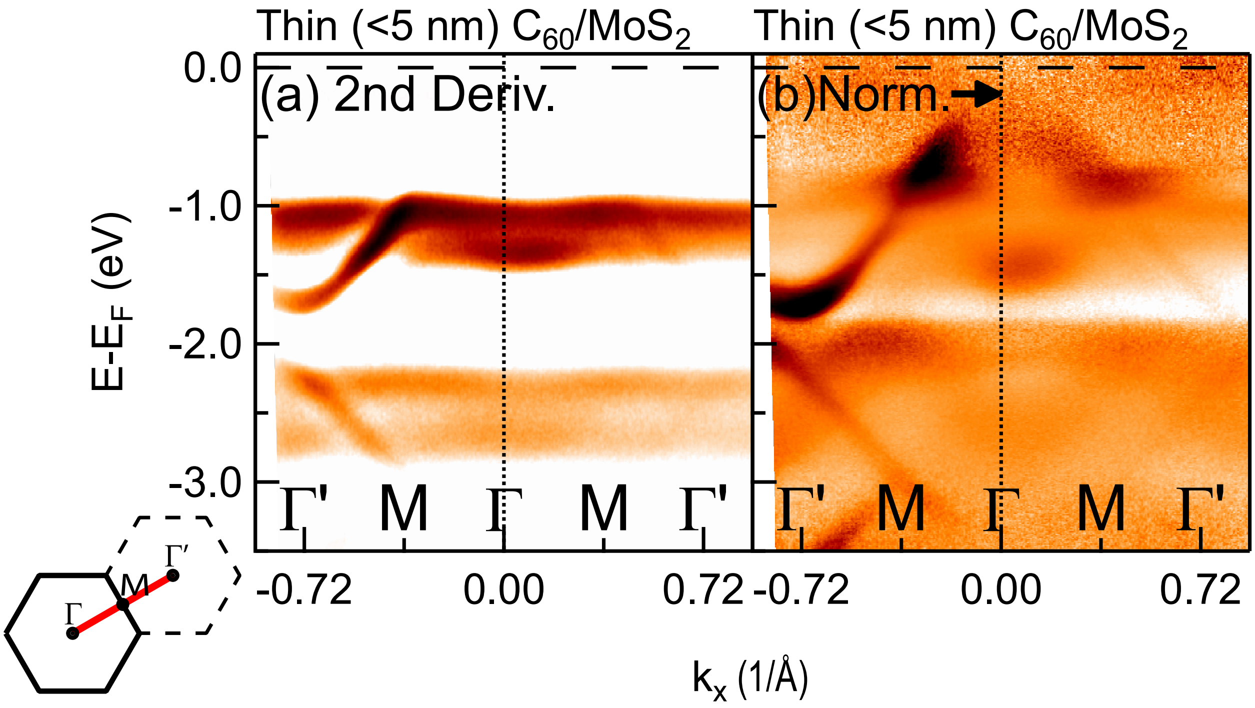

Figure 4.6: **(a)** Second derivative in the energy dimension of ARPES data along $\Gamma - \mathrm{M}$ for a ~ 1 nm C_{60} film on bulk MoS_2. **(b)** ARPES data with intensity normalized to reveal bulk MoS_2 bands. Data taken with 45 eV photons and at 20 K.

manifolds.

Fig. 4.6 presents ARPES data from a thin (~ 1 nm) C_{60} film on a bulk MoS_2 substrate. The second derivative of the raw ARPES data is shown in panel (a). By comparison with Fig. 4.5(b), we find that this thin C_{60} sample has little (if any) dispersion within the C_{60} band manifolds likely due to a lower quality film as compared with the thick film. On the left side of the image we see two new features traversing across the HOMO and HOMO-1, respectively. By looking at the intensity normalized ARPES data in Fig. 4.6(b), we can now clearly see that these features originate from the bulk MoS_2 valence bands. The ability to simultaneously probe the substrate MoS_2 and overlayer C_{60} allows us to observe the interaction between the two. As indicated by the black arrow in panel (b), the MoS_2 global valence band maximum is found to be only a few hundred meV below the Fermi level. This indicates a strong hole doping of the substrate MoS_2 by the C_{60} thin film. As explained earlier, this is due to C_{60} being an excellent electron acceptor. Such a strong interaction calls for further investigation into C_{60}/TMD heterostructures for electronic device applications.

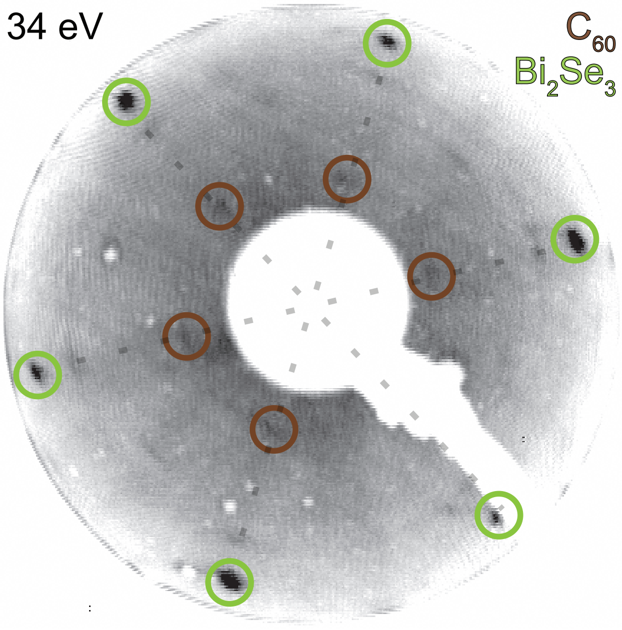

Figure 4.7: LEED image of monolayer C_{60} (brown) on bulk Bi_2Se_3 (green) at 34 eV showing perfect azimuthal alignment. Dotted gray lines are guides to the eye.

4.5 High Quality Growth on Bi_2Se_3

Although not a substrate that has been used for C_{60} growth in the past, Bi_2Se_3 has proven to provide the perfect foundation for high quality C_{60} thin films. The growth process used for C_{60} films on bulk Bi_2Se_3 is the same as that described in Section 4.2. C_{60} films of 5 nm (approximately 5 layers) on Bi_2Se_3 were used for the data presented in Chapters 5 and 6. A reference LEED measurement of a sample of monolayer C_{60} on Bi_2Se_3 is shown in Fig. 4.7. The LEED pattern of C_{60} and Bi_2Se_3 is able to be simultaneously resolved due to the single layer thickness of the C_{60} film. The Bi_2Se_3 surface drives the C_{60} buckyballs to order themselves during the deposition and creates and epitaxial C_{60} film with perfect azimuthal alignment with the substrate as shown by the perfect rotational alignment between the diffraction spots of C_{60} and Bi_2Se_3.

We can discover why Bi_2Se_3 is such a good substrate for C_{60} deposition by looking deeper into its properties. Bi_2Se_3 has a layered structure allowing for a clean, flat surface after in situ UHV cleaving ideal for thin film deposition. By comparing lattice constants, we find that $\sim$7 times the nearest neighbor distance between Se atoms on the Bi_2Se_3 surface is $\sim$3 times the nearest neighbor distance between C_{60} molecules (equivalent to the single layer lattice constant). Thus, a 3.4% compression on the close-packed C_{60} lattice is imposed as shown in Fig. 4.8. Additionally, the Bi_2Se_3 surface layer has a hexagonal lattice, in accord with the C_{60} single layer hexagonal lattice.

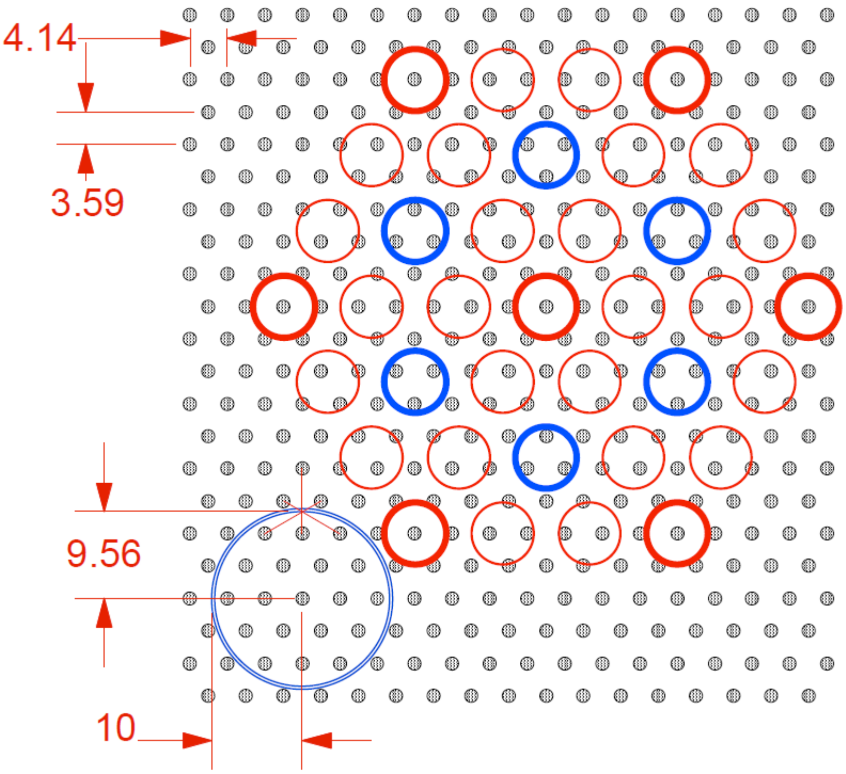

Figure 4.8: Bird's eye diagram of C_{60} (red and blue circles) alignment on the Se atom surface of bulk Bi_2Se_3 (small gray circles). All dimensions are given in units of angstroms.

Chapter 5

First Observation of Dispersive Pure C_{60} Band Structure

This chapter provides an in-depth study of the first experimental observation of highly-dispersive band structure in pure C_{60} through angle-resolved photoemission spectroscopy (ARPES) measurements supported by first-principles calculations. The effects previously hindering this observation are discussed as well as the role of the novel Bi_2Se_3 substrate in reducing C_{60} disorder and allowing for high quality epitaxial C_{60} deposition.

5.1 Introduction and Methods

Here we report the first observation of multiple highly dispersive bands in high quality C_{60} thin films grown on a novel substrate, Bi_2Se_3, within the HOMO and HOMO-1 band manifolds using high-resolution angle-resolved photoemission spectroscopy (ARPES) measurements. These results are enabled by the excellent lattice match between the Bi_2Se_3 substrate and C_{60} lattice and the constraints that the former imposes on the orientational order of the C_{60} molecules. The agreement of our results with density functional theory (DFT) calculations supports the presence of a long range crystalline order in the C_{60} thin films.

The high quality samples were grown on a bulk Bi_2Se_3 substrate cleaved in situ under ultra-high vacuum ($\sim 10^{-10}$ Torr) before C_{60} deposition using an effusion cell loaded with high purity (99.9%) C_{60} powder directed at the substrate. During the deposition (at $\sim 1 \times 10^{-9}$ Torr), the sample was heated between 100-200 °C to facilitate the arrangement of large crystalline domains through increased C_{60} mobility. A thickness of 5 nm (as measured by a quartz crystal thickness monitor) for the C_{60} thin film was chosen to accurately probe the C_{60} and minimize the substrate signal. We extract from our low-energy electron diffraction (LEED) measurements, shown in Fig. 5.1(a), a nearest neighbor spacing of $\sim$10 Å, similar to that of a bulk crystal. The clear LEED pattern consistent with C_{60} structure and the well-matched lattice constants testify that Bi_2Se_3 is an excellent substrate for growth of high

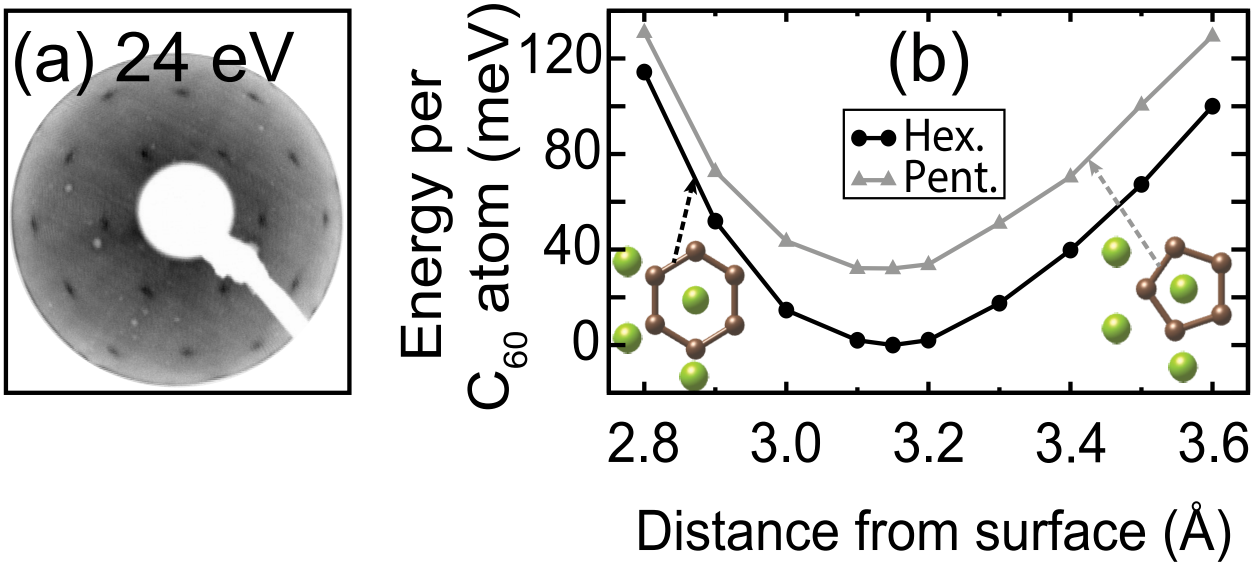

Figure 5.1: **(a)** LEED image of the crystalline 5 nm C_{60} film. **(b)** Calculated DFT total energy for hexagon-down and pentagon-down C_{60} molecules at various distances from a single layer of Se-terminated Bi_2Se_3 with van der Waals corrections included. Diagrams indicate the geometry of the bottom C_{60} face (brown) on the substrate Se surface atoms (green).

quality C_{60} films as previously discussed in Chapter 4. A further contributing factor to this harmony, as shown in Fig. 5.1(b) and discussed later on, is discovered in our calculations which favor the hexagon faces of C_{60}, as opposed to the pentagon faces, to point towards the Se surface atoms.

High-resolution ARPES experiments were performed at Beamline 4.0.3 (MERLIN) of the Advanced Light Source using 45 eV linearly polarized (mostly out-of-plane) photons in a vacuum better than 5×10^{-11} Torr. The total-energy resolution was 20 meV with an angular resolution ($\Delta\theta$) of $\leq 0.2°$. Data were taken at 20 K to assure the absence of spinning of the individual C_{60} molecules, known to rotate and follow a ratcheting behavior above 50 K [88].

5.2 Strong Photoemission Matrix Elements Effects in C_{60}

Integrated ARPES and Calculated DOS

Fig. 5.2 gives an overview of the physical and electronic structure of the thin film (5 nm) C_{60} sample. Panel (a) shows the HOMO and HOMO-1 energies for molecular C_{60}. These discrete energy levels evolve into dispersive manifolds for a crystalline lattice as a result of its symmetry and the interactions between C_{60} molecules, as shown in panel (b). We

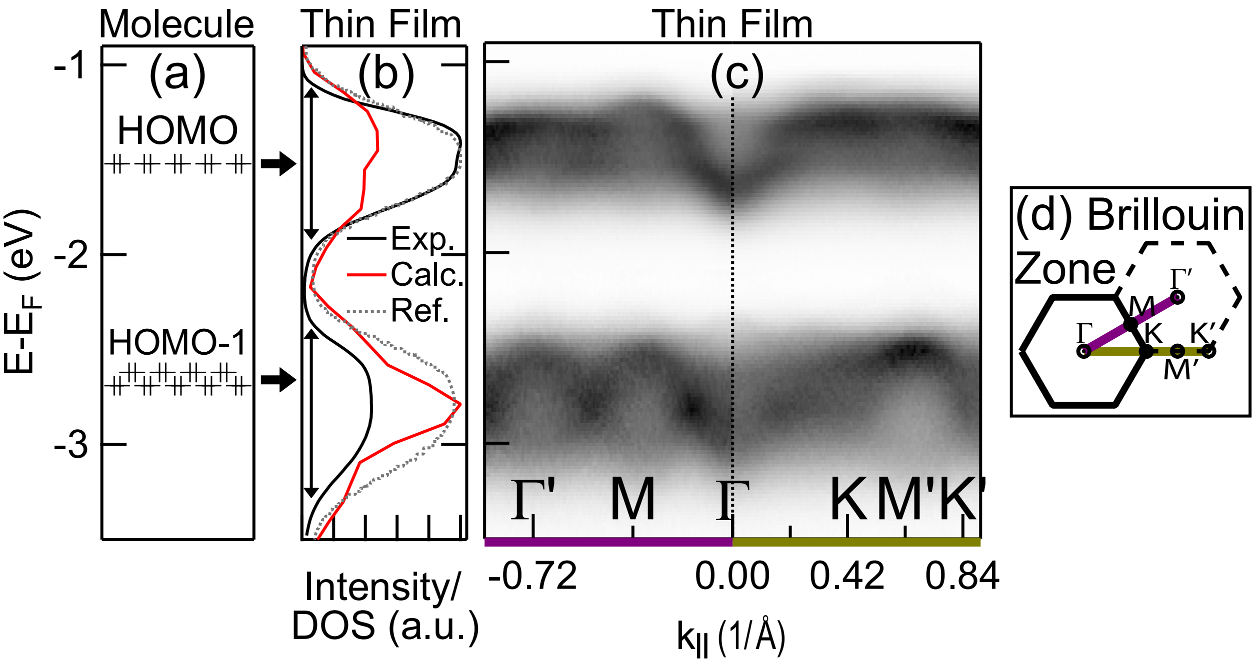

Figure 5.2: **(a)** Energy diagram comparing the molecular energy levels for the HOMO and HOMO-1 in a single C_{60} molecule with **(b)** the corresponding band manifold in a thin film as shown by momentum-integrated ARPES intensity within the first Brillouin zone (solid black line), literature data [96] (dotted gray line), and the calculated density of states (DOS, calculation for single layer C_{60}, solid red line). **(c)** ARPES data along each of the high symmetry directions indicated in panel (d) showing large dispersions in the HOMO and HOMO-1 band manifolds. **(d)** Reduced surface Brillouin zone of thin film C_{60}. ($h\nu = 45$ eV, $T = 20$ K).

see an overall good agreement between the momentum-integrated energy distribution curve (EDC) from our sample (black line) with the density of states (DOS, red line, computed with DFT for single layer C_{60}) and previous measurements on a different substrate (dotted gray line) [96] for both the HOMO and HOMO-1 centroid energies and bandwidths. The relative intensity of the two band manifolds is reversed when compared with the DFT DOS, but as shown in Fig. 5.3 this is due to matrix element effects not considered in our calculations.

Photon-Energy-Dependent Intensity

The average intensity from each band cluster in C_{60} is highly photon energy dependent. Most of the data presented in the main text was taken using 45 eV photons where the HOMO band cluster has about twice the average intensity as the HOMO-1 band cluster as can be seen in Fig. 5.3 (solid black line). This is the opposite of what we see in the density of states (DOS, yellow line, calculated for a single C_{60} layer) where the peak DOS for the HOMO is roughly

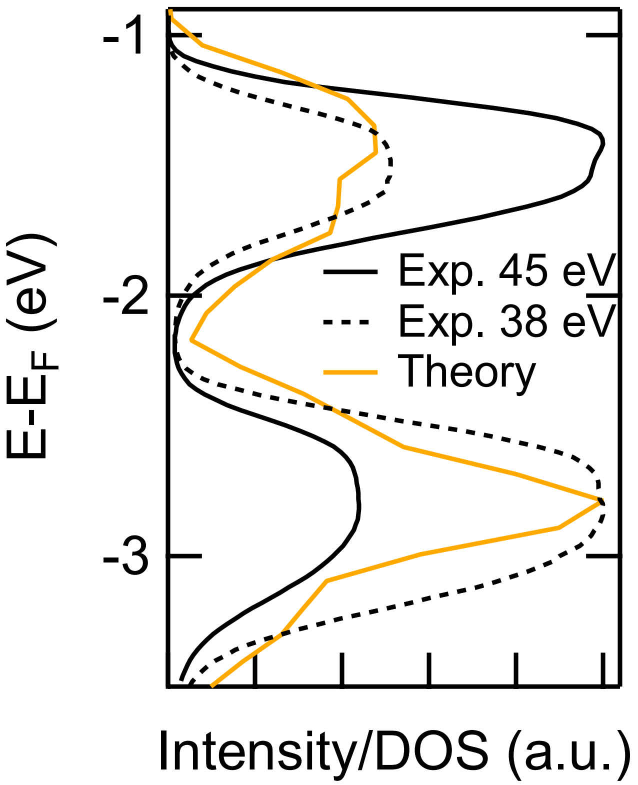

Figure 5.3: Momentum-integrated ARPES data for 45 eV (solid black line) and 38 eV (dashed black line) incident photon energy on a C_{60} film. Theory calculated density of states are presented in yellow.

half of that for the HOMO-1. This is, however, not indicative of a general disagreement between the theory and experiment due to the strong photon energy dependent intensity effects in C_{60}. For example, at 38 eV (dashed black line) incident photon energy we recover nearly the exact same ratio of HOMO to HOMO-1 intensity as we find in the calculated DOS. The photon energy dependence of C_{60} will be elaborated in Chapter 6.

Observation of Dispersive C_{60} Bands in Raw ARPES Data

The high quality of our C_{60} thin film, enabled by epitaxial growth and a reduction of rotational disorder thanks to the Bi_2Se_3 substrate, allows us to resolve for the first time highly dispersive HOMO and HOMO-1 bands along the high symmetry directions, as shown in panel (c). The location of the cuts are shown in the Brillouin zone diagram in panel (d).

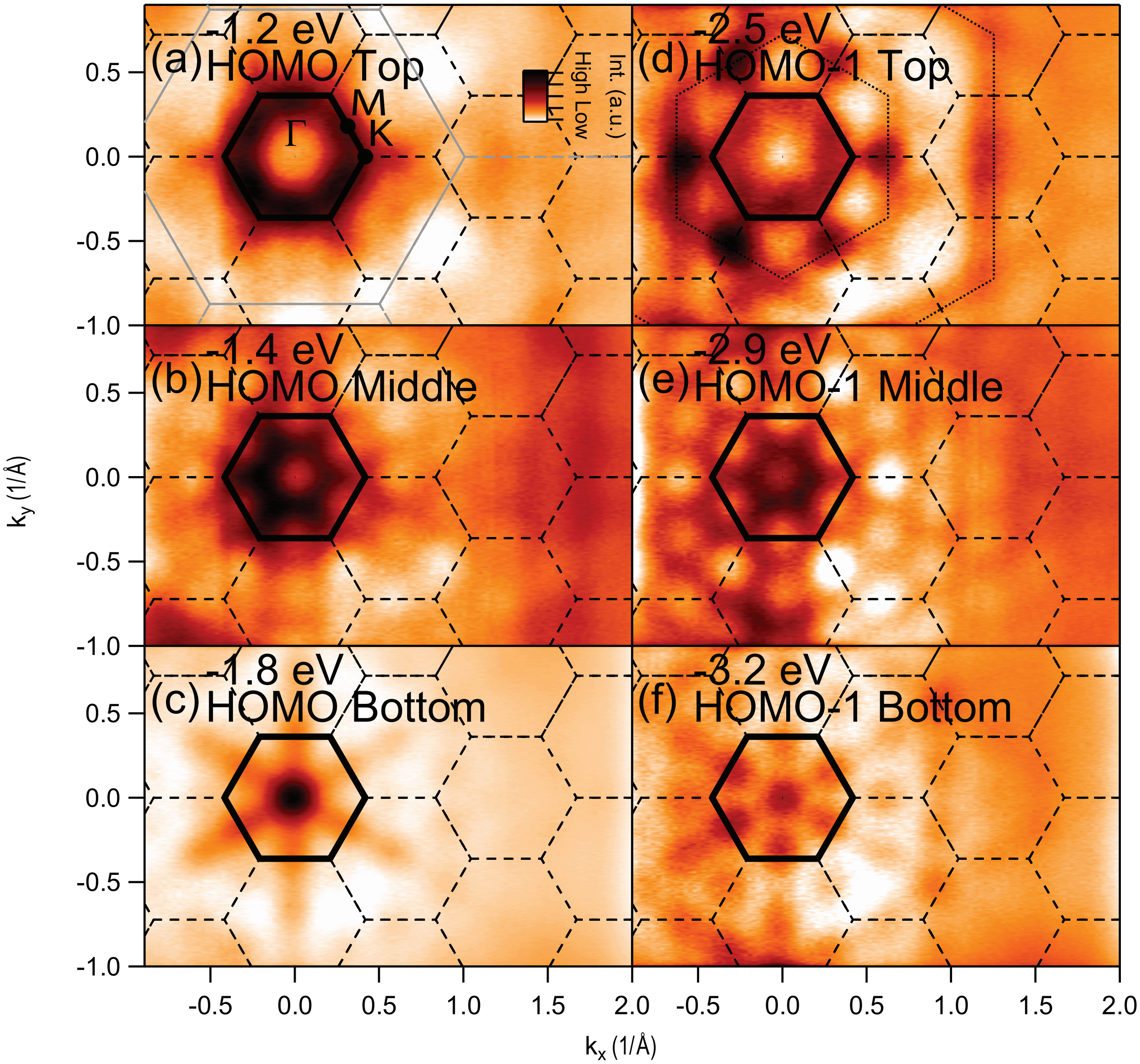

Figure 5.4: Constant energy maps of C_{60} with energies near the **(a)** HOMO top, **(b)** middle, **(c)** bottom, and **(d)** HOMO-1 top, **(e)** middle, and **(f)** bottom. The first Brillouin zone of C_{60} (Bi_2Se_3) is indicated by a thick black (gray) hexagon with the high-symmetry points labeled in panel (a). Dashed hexagons indicate higher order Brillouin zones, while two intensity patterns are highlighted in panel (d) by large dotted hexagons. ($h\nu = 45$ eV, $T = 20$ K).

Constant Energy Maps

HOMO Matrix Elements Effects

Fig. 5.4 shows the momentum location and the energy dispersion of the HOMO and HOMO-1 bands over multiple Brillouin zones (dotted black hexagons). Brillouin zone size was calculated using a C_{60} nearest neighbor spacing of 10.0 Å, consistent with LEED measurements (Fig. 5.1(a)) and our DFT calculations. Panels (a-f) show the constant energy maps at the top (a,d), middle (b,e), and bottom (c,f) of the HOMO and HOMO-1 band, respectively. In both cases, dipole matrix element effects enhance the intensity within the first Brillouin zone (thick black hexagon). For the top energy of the HOMO band manifold in panel (a), the most apparent feature is the strongly peaked hexagonal-like intensity pattern at the boundary of the first Brillouin zone. Moving to the middle energy of the HOMO band manifold (panel (b)), we see a highly periodic honeycomb-shaped structure which too has an enhanced intensity within the first Brillouin zone while faint highly periodic honeycomb-like features can still be observed in higher order Brillouin zones. These features decrease in size as we continue moving down in energy, eventually turning into an high intensity point at Γ at the bottom of the HOMO band (panel (c)). Here in panel (c), we observe an additional enhancement of intensity along the $\Gamma - \mathrm{M}$ high symmetry direction. The evolution of these features (panels (a)-(c)) is consistent with dispersive HOMO bands, whose minima occur at the Γ and M point.

HOMO-1 Matrix Elements Effects

The intensity maps of the HOMO-1 bands (Fig. 5.4(d-f)) show strong similarities as well as peculiar differences with the HOMO dispersions at equivalent energies—the main difference being the redistribution of spectral weight within the high symmetry points and the different Brillouin zones. Within the first Brillouin zone, the top of the HOMO-1 band (panel (d)) shows the same hexagonal intensity pattern as the top of the HOMO band (panel (a)). In contrast however, only three of the six M points are slightly more intense in this case, suggesting some breaking of the in-plane six-fold rotational symmetry of C_{60} down to three-fold, possibly due to the constrained rotation of the buckyball on the Bi_2Se_3 substrate, as discussed later. At this energy we also observe two large hexagonal intensity patterns beyond the first zone, as marked by the dotted line hexagons, that evolve as binding energy increases. These hexagonal patterns appear to be rotated by 30° with respect to the first Brillouin zone boundary and are three and twelve times as large in size, respectively, with maximum spectral weight at discrete points along the $\Gamma - \mathrm{K}$ direction.

As we continue decreasing in energy, the middle of the HOMO-1 (panel (e)) shows a honeycomb-shaped structure which decreases in size similarly as for the HOMO band, in agreement with an overall dispersion of the HOMO-1 band toward the Γ and M points. More specifically, we find the same honeycomb pattern found in the HOMO, but the effect of enhanced intensity is slightly reduced within the first Brillouin zone. Similarly, the bottom energy of the HOMO-1 (panel (f)) shows a similar pattern as the HOMO, but with the enhanced intensity effects reduced. A larger hexagonal pattern is again seen in the HOMO-1 at this energy.

Bi_2Se_3 Influence

While the origin of the hexagonal six-fold patterns is still not clear, when comparing them to the size and shape of the Bi_2Se_3 Brillouin zone (gray hexagon in panel (a)), we see that none of them align perfectly, making it unlikely that the substrate contributes significantly to the observation of these patterns. Additionally, comparisons with our DFT calculations (to be discussed later) suggest the direct influence of the substrate on the electronic structure of the C_{60} film is negligible. In summary these energy maps reveal highly dispersive HOMO and HOMO-1 bands whose minima occur at the Γ and M points. The different intensity patterns between the two reveal different dipole matrix elements and likely small, but important, differences in orbital character. Further studies are needed to fully understand the underlying orbital characters of these bands including the precise details.

Conclusions

Our findings underline the importance of taking into account matrix elements effects in C_{60} and their effect beyond the first Brillouin zone. Indeed, many previous studies only considered dispersions near or within the first Brillouin zone [97, 98, 99, 15, 16, 100, 9] and may have been susceptible to similar matrix elements effects that went unnoticed as the studies did not have a larger momentum range (like that of our study) to compare with. These effects could have inconspicuously affected their observations and conclusions. Additionally, with our relatively high photon energies ($\geq$30 eV), we are not susceptible to final state effects affecting the observed dispersions due to conduction band dispersion that may be present in previous studies claiming observation of HOMO and HOMO-1 dispersion using lower photon energies ($\lesssim$10 eV) [15, 16].

5.3 Reduction of C_{60} Disorder by Bi_2Se_3 Substrate

Figure 5.5 shows our DFT calculations for C_{60} and Bi_2Se_3 structures. Given the computational demands of a full *ab-initio* calculation of the Bi_2Se_3/C_{60} interface, we consider a representative interface of a C_{60} monolayer with hexagonal symmetry on one quintuple layer of $Bi_2Se_3(0001)$, where the separation between adjacent C_{60} molecules is 14.3 Å (compared to the experimental C_{60} separation of 10 Å). We use this interface structure to determine the degree of electronic hybridization between the C_{60} and substrate Bi_2Se_3, but do not (as will be elaborated) otherwise use it to compare to our experimental results. We calculated the relative energies of interfaces with Bi- and Se-terminated Bi_2Se_3 with both hexagon-down and pentagon-down C_{60} for variety of C_{60} distances from the substrate. Our calculations revealed that the lowest-energy interface structure was a Se-terminated hexagon-down interface, and we refer to this interface structure for our remaining calculations. We found that

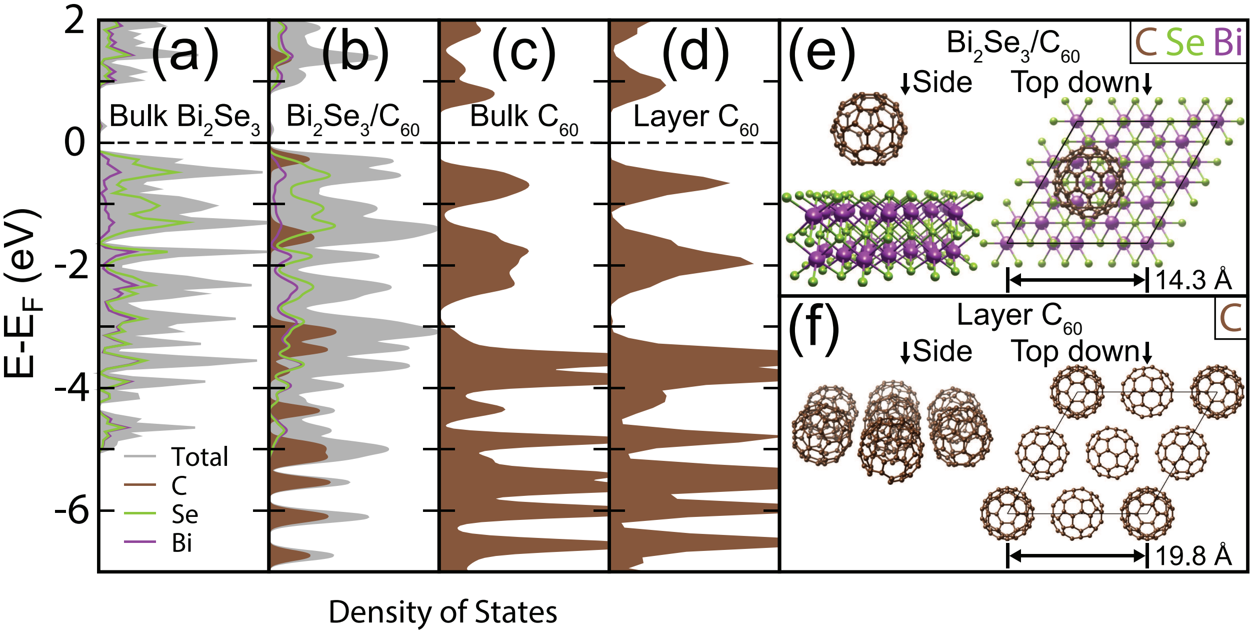

Figure 5.5: Calculated total and atom-projected density of states for **(a)** bulk Bi_2Se_3, **(b)** a single quintuple layer of $Bi_2Se_3(0001)$ with a hexagon-down C_{60} ball at its optimal distance of 3.15 Å, **(c)** bulk C_{60} in the $P\bar{a}3$ structure, and **(d)** a single hexagonal layer of C_{60} in the (111) direction of the $P\bar{a}3$ structure. In each calculation both van der Waals corrections and the spin-orbit interaction were included. **(e)** Configuration of the Bi_2Se_3/C_{60} structure used for DOS calculations in panel (b). **(f)** Configuration of the layer C_{60} structure used for DOS calculations in panel (d). See text for further details.

the Se-termination is almost 1.4 eV per Se atom lower in energy than the Bi-termination using DFT plus van der Waals corrections [101], while the pentagon and hexagon C_{60} interfaces are essentially degenerate when van der Waals corrections are not included. For the Se-terminated surface, we calculated the optimum distance of the C_{60} monolayer from the surface. The hexagon-down geometry is lower in energy than the pentagon-down case by 32 meV per C_{60} with an optimal distance of 3.15 Å with PBE+vdW and 4.05 Å for PBE as previously shown in Fig. 5.1(b). Furthermore, we find a slight (few meV) preference for the hexagon to align along the hexagonal directions set by the Se atoms. The lower energy for the alignment of a C_{60} hexagon face towards a Se atom, as compared with a pentagon face, imposes a constraint on the orientation of the C_{60} molecules on the Bi_2Se_3, which may favor some long range order beneficial for ARPES experiments.

The calculated electronic density of states for C_{60}, Bi_2Se_3, and the interface structure are shown in Fig. 5.5(a-d). Panel (a) shows the calculated density of states for bulk Bi_2Se_3 and panel (b) shows the lowest-energy Bi_2Se_3/C_{60} interface structure. A representation of the interface structure is shown in panel (e). The interface DOS shows little hybridization between the Bi_2Se_3 substrate and C_{60} molecule—the Bi and Se projected density of states in the Bi_2Se_3/C_{60} interface are very similar to those in bulk Bi_2Se_3. Owing to the lack of hybridization between the Bi_2Se_3 and C_{60} in our interface calculation (panel (b)), we calculate the density of states of bulk C_{60} in the $P\bar{a}3$ structure (the calculated ground-state structure, panel (c)) and the density of states of a single hexagonal layer of C_{60} (a slice of the $P\bar{a}3$ structure along (111), panel (d)). Interestingly, the density of states is quite similar in both cases suggesting that already in a single (111)-oriented layer, the C_{60} band dispersion is quite robust, which is also is supported by our experiments. As a result of these conclusions, we use the single layer C_{60} (structure shown in panel (f)) band structure calculations to compare with our experimental results, as will be discussed in Fig. 5.6.

5.4 Realization of Dispersive Valence Band Structure of Pure C_{60}

ARPES Curvature Data Reveals Distinct Dispersive Bands

Due to the lack of hybridization in our DFT calculations between states in the Bi_2Se_3 substrate and the C_{60} thin film, in Figure 5.6 we compare the experimentally measured valence bands of the C_{60} thin film to the calculated band structure for a single (111)-oriented layer of C_{60}. Fig. 5.6(a) shows energy vs. momentum cuts of the experimental thin film C_{60} band structure along the $\Gamma - \mathrm{M}$ and $\Gamma - \mathrm{K}$ high-symmetry directions. The curvature in the energy dimension of the raw data (Fig. 5.2(c)) is presented to more precisely locate and resolve the individual band dispersions. Two clear main dispersions are observed concurrently within each of the HOMO and HOMO-1 band manifolds which have bandwidths of 330 meV and 520 meV, respectively, based on the extent of the dispersions. As discussed previously in Fig. 5.4, for each band manifold these two dispersions provide both a local band maximum and minimum at Γ (as well as at M), unveiling bands previously not resolved experimentally.

HOMO and HOMO-1 Similarities

The high degree of similarity between the HOMO and HOMO-1 dispersions as noted in our constant energy maps (Fig. 5.4) is again readily apparent. Similarities between angle-resolved EDCs for the HOMO and the HOMO-1 band manifolds were previously reported for studies on cleaved (111) surfaces of C_{60} single crystals [100] including the observation of a band minimum at Γ in each of the band manifolds, which is compatible with our observations (in a thin film sample). In contrast, other studies have reported a local band maximum for the HOMO at Γ [15]. Our measurements reconcile this apparent disagreement, while providing a full view of the dispersion of multiple bands within each band manifold and simultaneously resolving two bands in both the HOMO and HOMO-1 with a local band maximum and minimum at Γ. Additionally, we have resolved another valence band manifold (HOMO-2) at higher binding energy (~ 4.5 eV) where multiple weakly dispersive bands can be discerned.

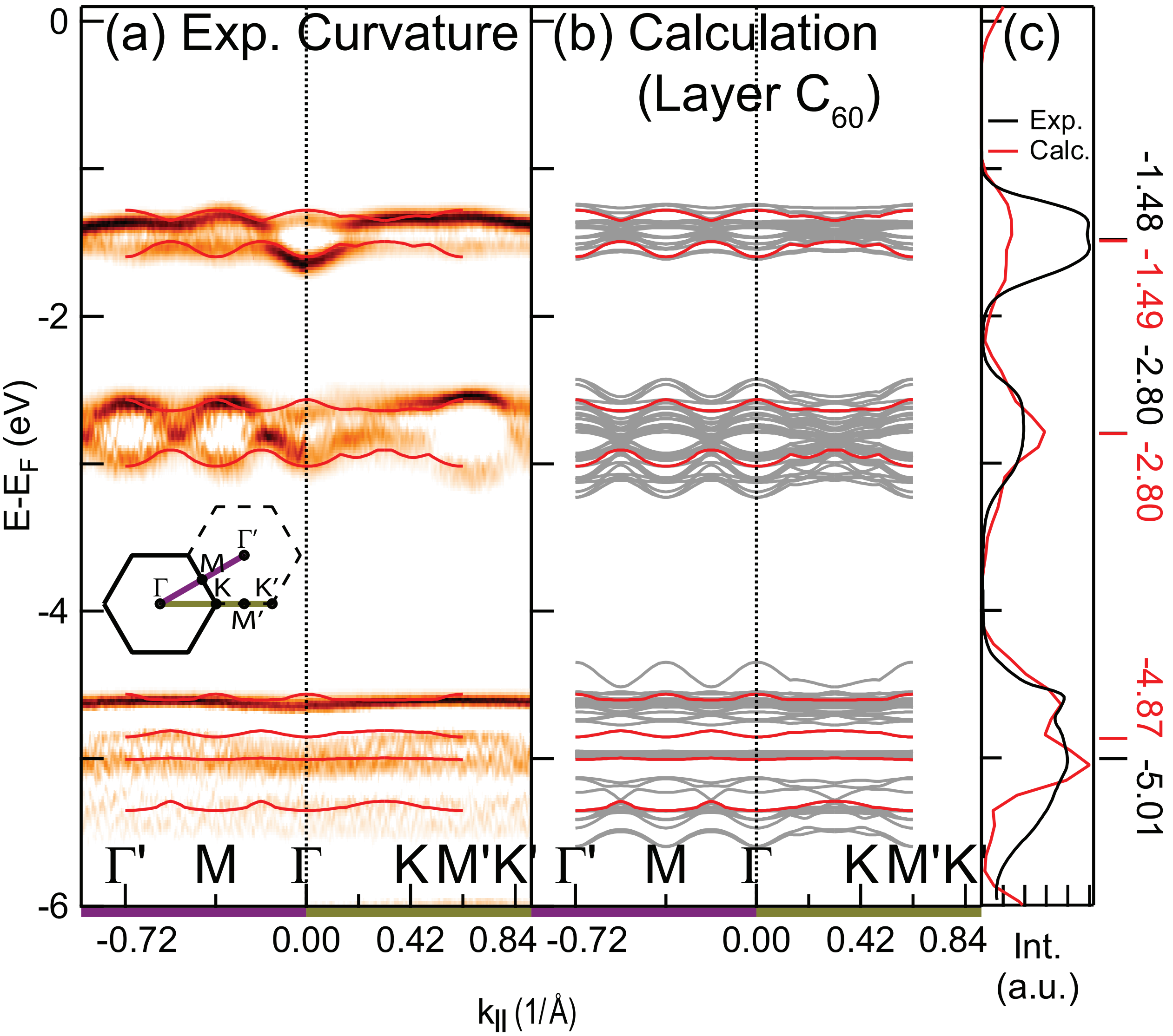

Figure 5.6: **(a)** Curvature of the electronic band structure of C_{60} along the $\Gamma - M$ (purple) and $\Gamma - K$ (olive) high-symmetry directions. The calculated bands that best fit the HOMO, HOMO-1, and HOMO-2 experimental dispersions are plotted over the data as red lines. **(b)** Full DFT-calculated theory band structure of single layer C_{60} including the same bands plotted in panel (a) highlighted in red. **(c)** Integrated EDC (black) across $\Gamma' - M - \Gamma - M - \Gamma'$ in comparison with DFT-calculated single layer C_{60} density of states (red) indicating the centroid energy of each experimental and calculated band manifold peak. ($h\nu = 45$ eV, $T = 20$ K).

Full Theory Calculations

Fig. 5.6(b) shows the complete DFT-calculated band structure for single layer C_{60} over the first three valence band manifolds. Despite lacking self-energy corrections, e.g. within the GW approximation, the DFT spectra show an overall good agreement with our experimental data across multiple valence band manifolds. The calculated bands show an upper and lower grouping for both the HOMO and HOMO-1 that follows the path of the experimentally observed dispersions with singular bands that best fit the dispersions highlighted here in red (also plotted in panel (a) for direct comparison). Similarly, the HOMO-2 band manifold at high energy shows an excellent agreement with the theory calculations. The upper and lower groupings are easily observed as shoulders in the integrated EDC in Fig. 5.6(c) (black). We find that these shoulders are not as well defined for lower quality samples lacking dispersive bands. The comparison of our experimental EDC with the theory-calculated density of states (red) shows an excellent agreement with only a 14.9% expansion in the energy dimension of the theory data. The center energy for the HOMO and HOMO-1 fit within just 10 meV of the calculated band structure and the HOMO-2 within 140 meV.

Many Body Effects

The comparison of observed experimental dispersions and DFT results motivates a discussion on many body effects in C_{60}. It has been reported that electron correlations and electron-phonon coupling play an important role in the electronic properties of C_{60} [102, 18, 23, 103, 104, 21]. Different groups have calculated the Hubbard parameter U or on-site Coulomb interaction (on-molecular and next-neighbor-ball) finding values between 0.8 eV and 1.6 eV [105, 88]. These proposed values are clearly greater than the electronic bandwidth measured in our experiment (0.33 eV for the HOMO), indicating that strong correlations are present in our C_{60} thin film. Despite the presence of such strong correlations, the constraints on the orientation of the C_{60} molecules imposed by the Bi_2Se_3 substrate potentially reduce the effects of disorder, provide a source of increased screening, and are likely the main effects enabling dispersive C_{60} bands [12]. We note that the strength of U can be reduced by the presence of a metallic substrate [106]. Given the metallic nature of our n-doped Bi_2Se_3 (chemical potential lies in the bulk conduction band), more studies are needed as a function of doping to determine the strength of such an effect.

5.5 Conclusions

In conclusion, we have identified a novel substrate for the growth of high quality thin film C_{60}, the topological insulator Bi_2Se_3. The constraints that this substrate imposes on the orientation of the buckyballs, its excellent lattice matching, and its metallic nature support a long range crystalline order in C_{60}, enabling the first observation of highly dispersive valence band structure, previously obscured by sample quality, momentum and energy resolution limitations, and final state effects. These results solve the missing link between electronic dispersions, vibronic loss, and the gas state spectra, paving the way for further investigations of the orbital character of the C_{60} bands and engineering of novel C_{60} heterostructures.

Chapter 6

Orbital Character Effects in the Photon Energy and Polarization Dependence of Pure C_{60} Photoemission

This chapter gives a comprehensive review of photon energy- and polarization-dependent effects in pure C_{60}. The effects of and new details about the orbital character of the C_{60} valence band manifolds are discussed with relation to our linear- and circular-polarization dependent ARPES data. Band manifold ARPES-intensity oscillations with photon energy (and hence, k_z) are discussed including implications for the precise details of the orbital character within each of the band manifolds.

6.1 Introduction and Methods

Fullerene C_{60} has a unique buckyball molecular structure and a crystalline form that exhibits a number of unconventional properties including relatively high T_c superconductivity when doped with alkali metals (A_3C_{60}) and a non-continuous transition to an insulating phase (A_4C_{60}) [23]. These, as well as other useful properties, have led to promising electronic device applications including photovoltaics [24], solar cells [25, 26], and field-effect devices [27, 28]. Additionally, interests in C_{60} extend to other fields such as astrophysics, where signature of the formation of C_{60} in the interstellar medium has been an active subject in recent years [29, 30, 31]. Despite such interest and promising applications, the dispersive C_{60} electronic valence band structure was unable to be observed experimentally until recently (as discussed in Chapter 5) and its complex photon energy and polarization dependent photoemission effects have yet to be thoroughly investigated especially in terms of orbital character details.

Polarization and photon energy dependent photoemission studies can reveal important details on both intrinsic material properties and how to interpret experimental data. Here we report on the detailed photon energy and polarization dependence of the thin film C_{60} band structure. The effect of different linear polarizations on C_{60} photoemission data has been largely unstudied until now. Schiessling et al. [17] found an angular dependence of C_{60} photoelectron intensity where intensity is maximized when the angle of the photoelectron and polarization vector is equal. Our linear polarization analysis reveals more expansive and specific polarization-dependent intensity enhancements and patterns for the HOMO and HOMO-1 as a result of strong matrix elements effects. Completely separate bands in the HOMO-2 are observed for different linear polarizations and we find a strong overall intensity effect for each band manifold based on orbital character.

Similar to the aforementioned lack of linear polarization dependence literature, little has been reported on its circular polarization dependence. Fecher et al. [107] performed circular dichroism studies on C_{60} thin films drawing a main conclusion that the HOMO-2 is mainly of a σ-like character at 30 eV. However, their methods used to come to this conclusion do not hold up to our more detailed analysis. Our circular polarization analysis provides a much larger wealth of data, reinforces our observations of multiple bands within each band manifold, and reveals a band splitting at the top of the HOMO not resolved with linear polarizations.

In contrast to the lack of polarization dependence literature, there has been significant experimental and theoretical study into the C_{60} band manifold intensity oscillations with photon energy [108, 109, 110, 111, 112, 9, 113, 114, 115, 116, 117, 118, 119, 120, 121]. Our photon-energy-dependent analysis of the C_{60} intensity oscillations with k_z determines the frequency and phase of the oscillations for the HOMO, HOMO-1, and HOMO-2 across a wide range of energy and in-plane momenta unlike previous studies that only look at the overall band manifold or at a single momentum. Our results reveal precise details of the differing orbital character of each band manifold especially within the HOMO-2.

High quality C_{60} thin film samples were grown in situ in an ultra-high vacuum on a bulk Bi_2Se_3 substrate as detailed elsewhere in Chapter 5. High-resolution ARPES experiments were performed at Beamline 4.0.3 (MERLIN) of the Advanced Light Source using 30–128 eV linearly or circularly polarized photons in a vacuum better than 5×10^{-11} Torr. The total-energy resolution was 20 meV with an angular resolution ($\Delta\theta$) of $\leq 0.2°$. Data were taken at 20 K to assure the absence of spinning of the individual C_{60} molecules, known to rotate and follow a ratcheting behavior above 50 K [88].

6.2 Linear Polarization Effects

Constant Energy Maps

Matrix Elements Effects: Enhanced Intensity and Patterns

Figures 6.2 and 6.3 show the linear-polarization-dependent band structure of thin film C_{60} with ARPES constant energy maps. Fig. 6.1 presents the experimental setup indicating

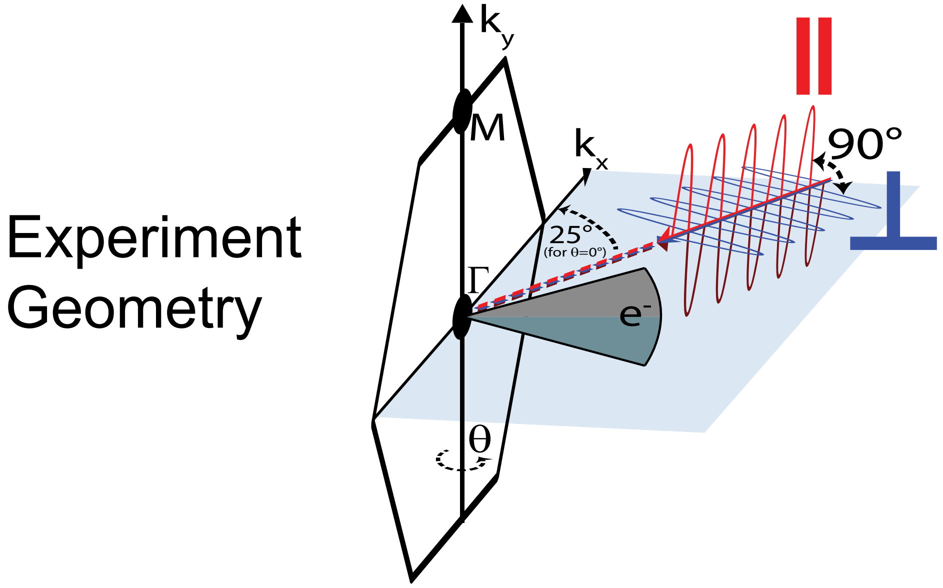

Figure 6.1: Geometry of the experimental setup indicating incoming light polarization, outgoing photoelectrons, and Brillouin zone for the C_{60} thin film.

sample orientation, outgoing photoelectrons, and incoming photon beam. Two orthogonal linearly-polarized beams are depicted: mostly out-of-plane light polarization ($\perp$, blue) and fully in-plane light polarization ($\|$, red). We compare constant energy maps taken with these two orthogonal linear light polarizations at energies near the top and bottom of the HOMO and HOMO-1, as shown in Figures 6.2 and 6.3. We note a strong intensity pattern following the first Brillouin zone boundary (thick black hexagon) for the top energy of the HOMO with $\perp$ polarized light (Fig. 6.2(a)), which is completely attenuated for $\|$ light. The $\|$ data reveals the intensity spot corresponding to the band maximum at Γ which is entirely obscured otherwise due to the intensity effect. Similarly, we observe an enhanced intensity at Γ for the bottom of the HOMO (Fig. 6.2(b)), which is reduced in the $\|$ case along with the asterisk-shaped intensity pattern radiating along $\Gamma - \mathrm{M}$ into higher-order Brillouin zones (dashed-line hexagons). The intensity at the Γ' points in these higher-order Brillouin zones is relatively increased for the $\|$ case and we recover a close resemblance between the first and higher-order Brillouin zones.

Similar to the HOMO, the top energy of the HOMO-1 has an enhanced intensity along its first Brillouin zone boundary for the $\perp$ polarization (Fig. 6.3(a)), albeit with a lesser magnitude than in the HOMO case. Additionally, we observe large strong intensity patterns outside of the first Brillouin zone marked here by dotted bright green hexagons. These patterns again nearly completely disappear for the $\|$ polarization. The bottom energy of the HOMO-1 (Fig. 6.3(b)) exhibits a slightly enhanced intensity within the first Brillouin zone

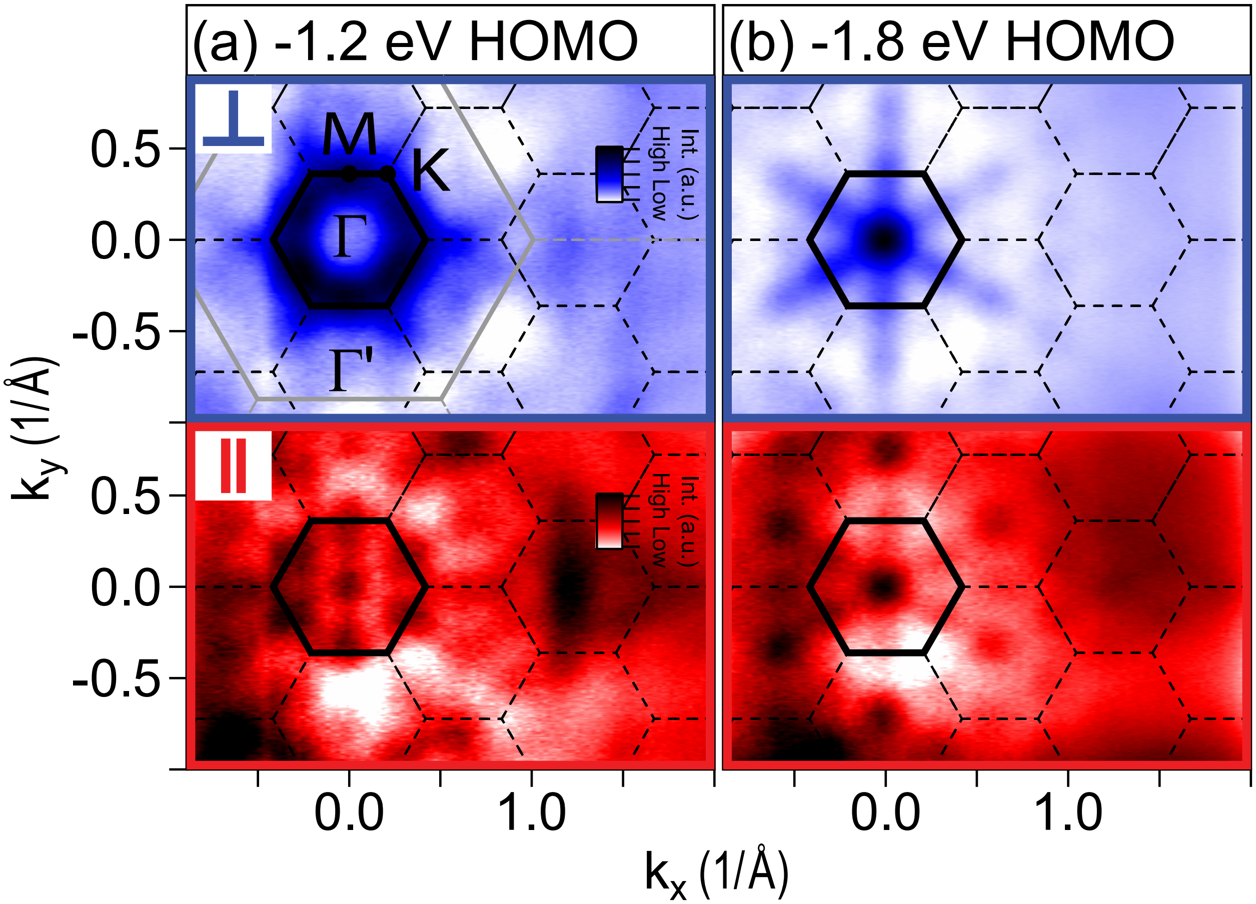

Figure 6.2: High resolution constant energy maps of C_{60} (5 nm) on Bi_2Se_3 with cuts through the energies near the **(a)** HOMO top and **(b)** HOMO bottom. Upper and lower images are taken with out-of-plane light polarization ($\perp$, blue) and in-plane light polarization ($\parallel$, red), respectively. The first Brillouin zone of C_{60} (Bi_2Se_3) is indicated by a thick black (gray) hexagon with the high-symmetry points labeled in panel (a). ($h\nu = 45$ eV, $T = 20$ K).

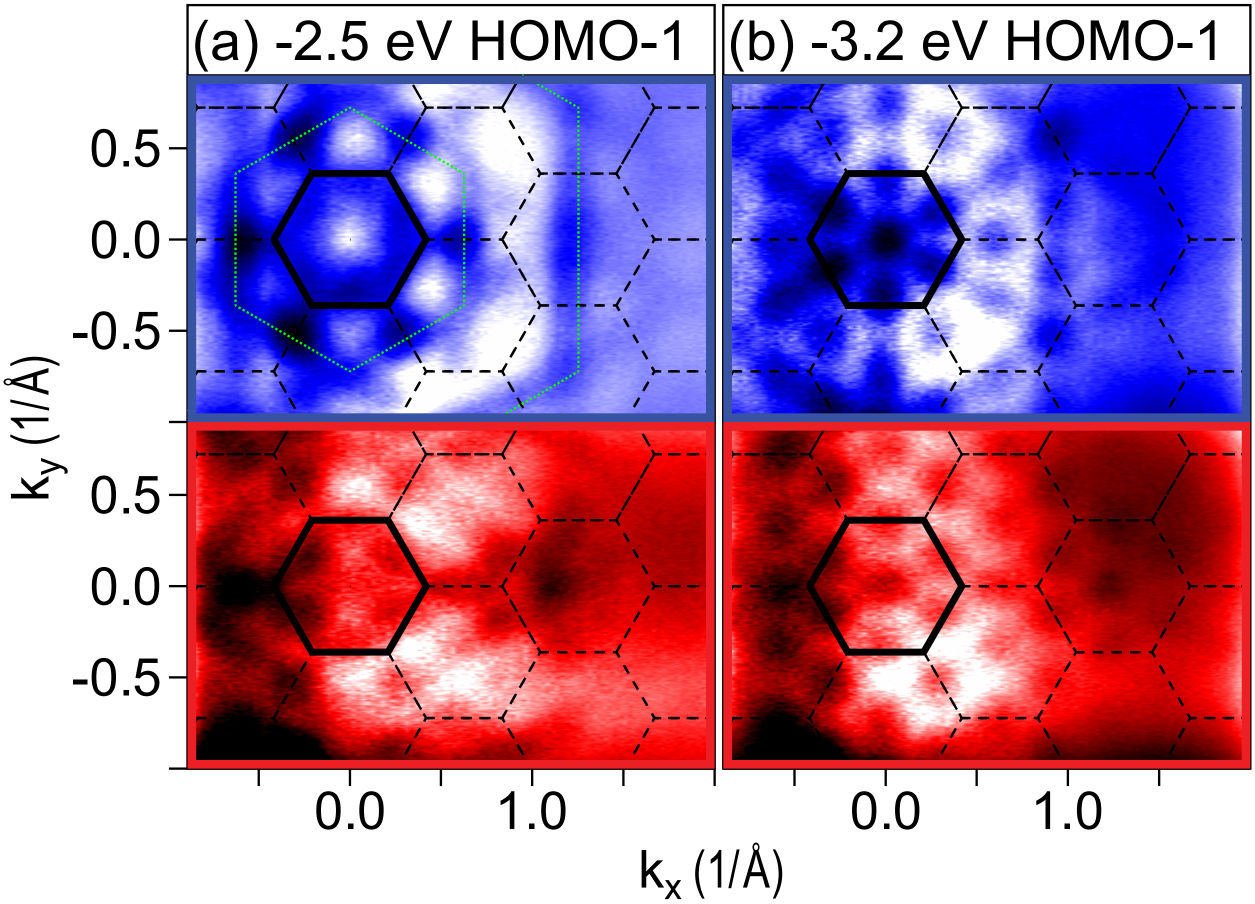

Figure 6.3: High resolution constant energy maps of C_{60} (5 nm) on Bi_2Se_3 with cuts through the energies near the **(a)** HOMO-1 top and **(b)** HOMO-1 bottom. Upper and lower images are taken with out-of-plane light polarization ($\perp$, blue) and in-plane light polarization ($\|$, red), respectively. ($h\nu = 45$ eV, $T = 20$ K).

and a large intensity pattern outside of it as well. Again, these effects are largely negated when the polarization is switched to $\|$.

Orbital Character Effects

Elaboration on the possible cause of the observed intensity effects necessitates a discussion on the predicted orbital character of the HOMO and HOMO-1. Two quantum numbers can be used to label the molecular orbitals in C_{60}: n and l. This labeling scheme was introduced by Martins et al. [122] who assumed that the screened electronic potential in C_{60} is localized on a hollow shell encompassing the buckyball. Motivated by the spherical shape of C_{60}, this model takes into account the angular behavior of the molecular orbitals. The angular number l describes therefore the angular pattern of the wavefunction nodes, while the principal quantum number n equals the number of radial nodes plus one. The σ wavefunctions, which do not have a radial nodal surface as they lie on the surface on the buckyball, correspond to $n = 1$, while π orbitals having one radial nodal surface at the buckyball surface correspond to $n = 2$. Inspection of the radial functions of each molecular orbital in C_{60} allows the labeling of the HOMO with π_5 (i.e. $n = 2$ and $l = 5$) and the HOMO-1 with π_4 (i.e. $n = 2$ and $l = 4$). In other words, the HOMO and HOMO-1 are both formed entirely from π orbital character, but differ in angular number by one. Others have confirmed these predictions finding that the π orbitals for both the HOMO and HOMO-1 are localized to surfaces just outside and inside the icosahedral C_{60} shell [108, 123, 124] with a nodal surface along the buckyball surface (see Fig. 6.4(e) for a diagram). The HOMO and HOMO-1 can be further distinguished as the HOMO is formed by h_u orbitals, while the HOMO-1 is formed by g_g and h_g orbitals. These are formed entirely by p orbitals perpendicular to the surface at each carbon atom except for the h_g orbital which has a 25% contribution from in-plane p orbitals as a result of renormalization due to the curved buckyball surface [125].

Conclusions

The strong intensity enhancements and patterns are due to strong photoemission matrix elements effects (most evident in the $\perp$ polarized data) which manifest in different ways for the HOMO and HOMO-1 likely as a result of their small orbital character differences described above. In all cases we find these effects to be minimized for the $\parallel$ polarization and we are able to observe strong similarities between the HOMO and HOMO-1 dispersions as reported previously in Chapter 5. For example, when considering the $\parallel$ polarization maps, the top energy of the HOMO and HOMO-1 (bottom of Figures 6.2(a) and 6.3(a), respectively) both primarily show intensity spots at Γ and M (and at equivalent locations in higher-order Brillouin zones) indicating local band maxima at these momenta. The bottom energy of the HOMO and HOMO-1 (bottom of Figures 6.2(b) and 6.3(b), respectively) show similar patterns indicating local band minima at Γ and M as well. The similarity in dispersion for the HOMO and HOMO-1 is most likely a result of their overall similar π-orbital character. We note that similarities in the electronic structure of the HOMO and HOMO-1, while less extensive than in our studies, have been previously reported for a bulk C_{60} sample [100].

Energy vs. Momentum Cuts

Matrix Elements Effects on Observed Dispersions

Fig. 6.4 compares ARPES curvature (in the energy dimension) data along $\Gamma - \mathrm{M}$ from each of the two orthogonal linear light polarizations. The enhanced first Brillouin zone intensity effects observed in the $\perp$ constant energy maps of Figures 6.2 and 6.3 manifest themselves as stronger peaks and/or slight shifts of the dispersions shown in Fig. 6.4(a). For example, as seen by comparing the HOMO in the ARPES curvature image with $\perp$ polarization in panel

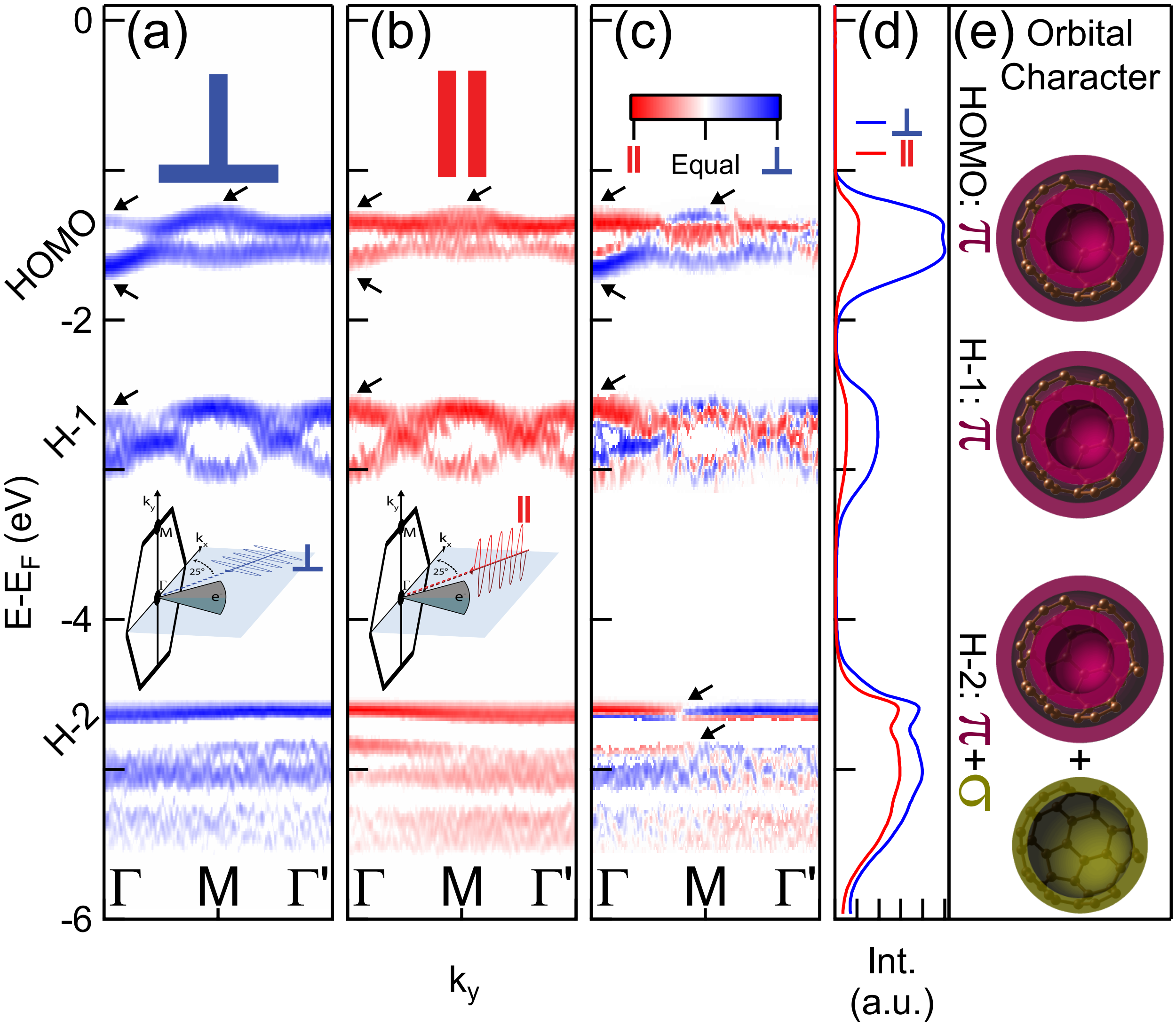

Figure 6.4: Polarization dependent C_{60} band structure along $\Gamma - \mathrm{M}$ from ARPES curvature using **(a)** out-of-plane light polarization ($\perp$, blue), **(b)** in-plane ($\parallel$, red), and **(c)** their difference. See insets for polarization geometry. **(d)** Integrated EDCs across $\Gamma' - \mathrm{M} - \Gamma - \mathrm{M} - \Gamma'$ for incident out-of-plane (blue) and in-plane (red) polarized light. Intensities were normalized by incident photon flux. **(e)** Diagram of the theory-derived orbital character of each band manifold.

(a) to that with $\parallel$ polarization in panel (b), the band maximum at Γ is diminished, while the band minimum at Γ and the band maximum at M are enhanced for the $\perp$ polarization (see arrows). This is nicely summarized in panel (c) by comparing the difference of the curvature from each polarization where we can see a red color (corresponding to stronger $\parallel$ curvature) for the HOMO band maximum at Γ, and a blue color ($\perp$ is stronger) for the HOMO band minimum at Γ and band maximum at M. Similar to the HOMO, the HOMO-1 (H-1) band maximum at Γ is also weakened for the $\perp$ polarization as shown by a strong red band maximum at Γ in the HOMO-1 in panel (c) (see arrows). Considering only the $\parallel$ polarization for a moment, we see the same dispersions at both Γ and Γ' for the HOMO and HOMO-1 as one would have initially predicted when comparing equivalent momenta. Just as observed in the constant energy maps, the matrix elements intensity effects are minimized in this case, while for the $\perp$ case we see clear differences (as previously mentioned for Figures 6.2 and 6.3) when comparing Γ and Γ'.

In addition to the HOMO and HOMO-1, we are able to resolve the next highest band manifold, the HOMO-2 (H-2), as well. The polarization-dependent effects are even more striking in the HOMO-2 as the two polarizations appear to reveal, in multiple instances, completely separate bands. Starting from the top energy of the HOMO-2 for the $\perp$ polarization in Fig. 6.4(a), we find that the first two bands have a minimum at Γ and rise to a maximum at Γ'. However, when the polarization is switched to $\parallel$ as in panel (b), we find that the top two observable bands now have a maximum at Γ and move down in energy to a minimum at Γ', opposite of the behavior observed for the $\perp$ polarization. This can be observed more clearly in panel (c) as the discussed bands flip colors (for a given energy) going from Γ to Γ' (see arrows where flip occurs). Evidently, the effect of the polarization dependence on these top HOMO-2 bands is so strong that the two orthogonal polarizations reveal completely separate bands in the photoemission data. The HOMO-2, unlike the HOMO and HOMO-1, has majority contribution from σ-like bands which may be responsible for the specific polarization-dependent bands pointed out here as we do not see such features in the entirely π-like HOMO and HOMO-1. A possible explanation for the differences observed with $\perp$ and $\parallel$ polarizations for all of the band manifolds may be related to the highly two-dimensional nature of the C_{60} thin film as it is only $\sim$5 layers thick while simultaneously exhibiting high lateral order which represents a clear difference between its in-plane and out-of-plane physical structure which may couple differently with the in-plane and out-of-plane polarizations.

Orbital Character Effects on Overall Band Manifold Intensity

Fig. 6.4(d) shows a momentum-integrated energy distribution curve (EDC) comparison for the $\perp$ (blue) and $\parallel$ (red) polarizations which are normalized by incident photon flux. The overall intensity within the HOMO and HOMO-1 band manifolds for the $\parallel$ polarization is greatly reduced by 79% and 72%, respectively, as compared with the $\perp$ polarization. However, the HOMO-2 intensity is hardly diminished comparatively as it is reduced by only 24%. We believe this to be a consequence of the differing overall orbital character of the

HOMO and HOMO-1 compared with the HOMO-2. As previously discussed, the HOMO and HOMO-1 are of entirely π orbital character. However, the HOMO-2 is a mixture of π (g_u and t_{2u} orbitals) and σ (h_u and h_g orbitals) states, with more than half of the HOMO-2 electrons being of a σ nature [5, 126]. As shown in panel (e), the physical implications of this are that the π-like states are localized to a surface outside and inside the C_{60} shell with a nodal surface along the buckyball surface (as for the HOMO, HOMO-1, and partially the HOMO-2), while the σ-like states are localized to a surface on the C_{60} shell (as mostly for the HOMO-2). In the HOMO, HOMO-1, and HOMO-2, the photoemission signal is evidently minimized from the π-like states for the case of $\|$ incident light, while the σ-like states are left mostly unattenuated in that case.

Further explanation of the linear-polarization effect on overall band manifold intensity may be found by considering the available experimental data and theory regarding the photon energy and polarization-dependent partial cross sections of the band manifolds. The partial differential cross sections have been calculated to be $d\sigma/d\Omega = (\sigma_{tot}/4\pi)[1 + \beta P_2(\cos\phi)]$ considering electric dipole absorption with a single-electron model [127, 14, 128] (for total cross section σ_{tot}, asymmetry parameter β, second order Legendre polynomial P_2, and angle between outgoing photoelectron and incoming polarization vector ϕ). The asymmetry parameter β is dependent on the orbital character of each band manifold, particularly the angular momentum quantum number l. It is also dependent on photon energy and for 45 eV, it is found to be 0.95, 1.1, and 0.5 for the HOMO, HOMO-1, and HOMO-2, respectively [118, 117]. Given ϕ's dependence on the polarization vector, when switching from $\perp$ to $\|$ the partial cross section would decrease by approximately 66% and 71% for the HOMO and HOMO-1, respectively, but only 42% for the HOMO-2. A decrease in partial cross section would lead to a proportional decrease in observed intensity. Hence, the large decrease of the HOMO and HOMO-1 partial cross sections and the smaller decrease of the HOMO-2 partial cross section, while not an exact quantitative match, is consistent with our observations and likely a contributing factor to the polarization-dependent overall band manifold intensity effect observed in addition to the π and σ orbital character effect previously discussed. In either case, the differences in the band manifolds' orbital character are the driving forces behind this effect.

6.3 Circular Dichroism Effects

Effect of Experiment Handedness

In order to fully explore the nature and orbital character details of C_{60}'s valence bands, we continued our polarization dependence by measuring the corresponding ARPES circular dichroism (CD) in Fig. 6.5 using left- and right-hand circularly polarized light. CD effects are known to occur in all spatially oriented molecular thin films when using an experimental geometry with a handedness [129, 130]. This handedness is achieved in our experiment (panel (b)) when the direction of the incoming left-hand (LC) or right-hand (RC) circularly

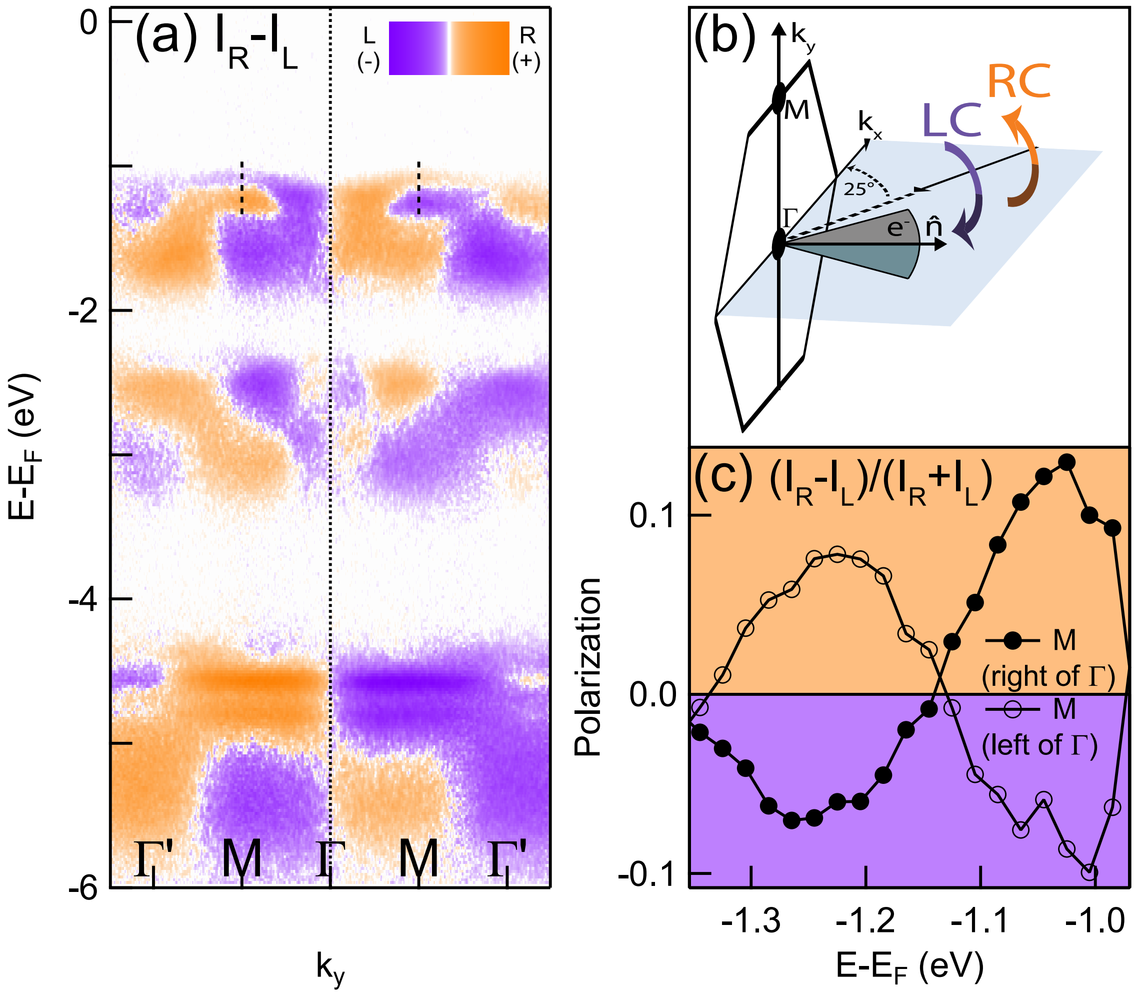

Figure 6.5: **(a)** Circular dichroism intensity difference ($I_R - I_L$) of C_{60} band structure along $\Gamma - M$ where orange (purple) indicates a stronger intensity from right-hand (left-hand) circularly polarized incident light. **(b)** Geometry of the experimental setup indicating incoming right-hand (RC, orange) or left-hand (LC, purple) circularly polarized light, outgoing photoelectrons, sample normal n̂, and Brillouin zone. **(c)** Circular dichroism polarization ($[I_R - I_L]/[I_R + I_L]$) versus energy near the top energy of the HOMO at the M points on either side of Γ (dashed lines in panel (a)).

polarized photon beam, the sample normal n̂, and the outgoing photoelectrons (e^-) do not lie in the same plane as is the case for all displayed momenta in panel (a) except at precisely Γ (coincident with n̂) where the circular dichroism effect disappears as a result of the loss of handedness. The handedness combined with the symmetry of the C_{60} thin film is the cause of the change in sign of the CD intensity when crossing Γ.

Observation of Split HOMO Bands

We resolve similar dispersions as observed for linearly polarized light, particularly for the HOMO-1 where in Fig. 6.5(a) we see two main band groupings near the top and bottom energies differentiated by opposing signs of circular dichroism intensity ($I_R - I_L$) indicated by the orange (positive, $I_R > I_L$) and purple (negative, $I_L > I_R$) colors. The HOMO has a similar structure, but the upper energy grouping is further split in two to reveal separate features that were previously combined for either of the linear polarizations. It is only in our CD data that this more detailed structure is observed. As for the HOMO-2, similar to the linear polarizations, we resolve two weakly dispersing features between -4.43 eV to -4.95 eV with similar CD polarizations which are opposite in sign of the CD polarization of the bottom half (-4.95 eV to -5.8 eV) of the HOMO-2. These HOMO-2 features will be discussed later on with regards to our photon-energy-dependent observations. Overall, we see the same structure in our circular dichroism on either side of Γ demonstrating a proper normalization of the incident photon flux and promoting the validity of the circular dichroism features we observe.

Orbital Character Determination

A previous CD study on C_{60} thin films [107] found that, when compared with one another, the HOMO and HOMO-1 showed the same sign and a similar magnitude of CD polarization while the HOMO-2 showed an opposite sign of CD polarization. They concluded that the opposing polarization of the HOMO-2 must originate from its (mostly) σ orbital character based on the fact that opposing signs of CD were observed for σ and π bands in graphite [131]. This reasoning does not hold up to our more detailed analysis as we observe opposing signs of CD within even just the HOMO (or HOMO-1), which has entirely π orbital character (as does the HOMO-1). Therefore, we cannot conclude the overall band manifold character from the overall CD for each band manifold, but this does not preclude observing more precise orbital character effects from the bands within each band manifold.

Evidence of Strong Circular Dichroism

We more closely examine the polarization change across the upper HOMO splitting at the M point on either side of Γ in Fig. 6.5(c). The curve with filled circles is from M on the right side of Γ, while the open circles are from the left. The CD signal is nearly perfectly inverted on either side of Γ, as expected. We see substantial CD polarization in this split

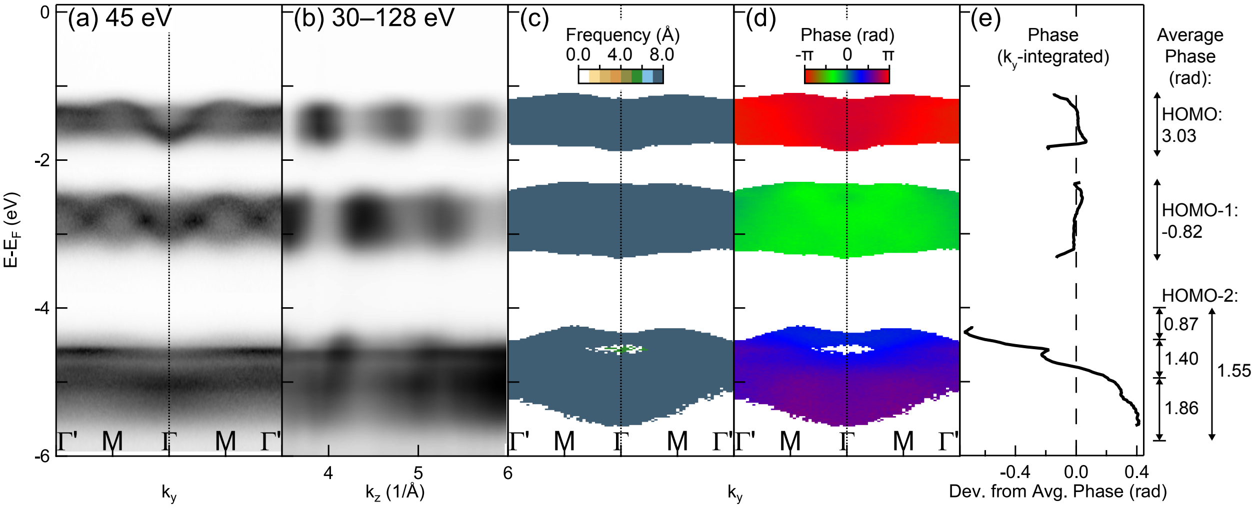

Figure 6.6: **(a)** High-resolution ARPES band structure of C60 along $\Gamma - \mathrm{M}$ at 45 eV for reference. **(b)** Integrated ARPES intensity across the momentum range in panel (a) for 30–128 eV showing intensity oscillations with respect to k_z in the HOMO, HOMO-1, and HOMO-2. **(c)** Extracted frequency of the oscillations for each in-plane momentum (k_y) and energy shown. **(d)** Extracted relative phase of the oscillations for each in-plane momentum (k_y) and energy shown. **(e)** Deviation of phase (momentum-integrated across full k_y window) from average phase for each band manifold. Average (mean) phase for each band manifold shown to the right including for specific energy ranges within the HOMO-2.

feature as the polarization of the upper feature reaches a magnitude of approximately 0.10, while the lower feature reaches a magnitude of approximately 0.08 (with opposite sign). A contributing factor leading to the observation of strong CD polarizations in our C_{60} thin film is likely its low disorder as previous reports [129] have linked increased disorder within a molecular thin film with a decreased CD polarization. The low disorder of our C_{60} thin film is a result of its epitaxial growth on and interaction with Bi_2Se_3 as detailed elsewhere in Chapter 5. We note that the strength of CD polarization may also depend on the angle of incidence of the incoming light (angle shown in panel (b)). For example, a sine factor based on the angle of incoming light is added to the CD polarization in the case of a simple p_z orbital [132, 130]. C_{60}, however, does not have such simply-oriented orbitals (e.g. a p_z orbital) given its unique buckyball shape so is unlikely to have such a strong dependence on the angle of incoming light, but there may be some geometric effect given its two-dimensional thin film nature as opposed to that of a fully three-dimensional bulk sample.

6.4 Photon Energy Dependence

Frequency and Phase Analysis of Intensity Oscillations

In Fig. 6.6, we present our findings on the observed strong oscillations of the band manifolds' intensity with photon energy (and hence k_z). Similar oscillations have been reported in previous works on C_{60} bulk crystals [9, 14] and thin films [133, 113, 120]. High resolution data were taken for the HOMO, HOMO-1, and HOMO-2 bands along $\Gamma - M$ spanning a range of two Brillouin zones with 30–128 eV (step size of 2 eV) ⊥-polarized photons. Fig. 6.6(a) presents data at 45 eV incident photon energy across the range of energy and in-plane momenta (k_y) considered in our oscillation analysis. Strong oscillations of the band manifolds' intensity with k_z can be observed in Fig. 6.6(b) where intensities were obtained by momentum-integrating across the k_y range in panel (a). In the past, these oscillations were thought to be related to strong final state effects [9], but later on were identified as a signature of interference of photoelectron waves emanating from each of the constituent C_{60} carbon atoms, where each wave has a different phase. The unique spherical structure of C_{60} and its large radius play a critical role in this effect [133, 109, 108, 120].

In order to investigate the observed k_z dependent oscillations and their link to the orbital character of the different band manifolds, we performed Fourier analysis using a Fast Fourier Transform (FFT) algorithm (see Supplemental Material). This analysis is used to separate the intensity oscillation (with respect to k_z) curves into different frequency components. We are able to determine the dominant frequency of the oscillation and the corresponding phase (for that frequency component). For each energy and in-plane momenta we extracted the dominant frequency and corresponding phase of the k_z dependent oscillations as shown in Figure 6.6(c) and (d), respectively. As shown in panel (c), the dominant frequency of the oscillations is nearly identical in each band manifold (≈7.5 Å), which is very close to the molecule's structural diameter of 7.1 Å [134, 135, 108] as expected. The phase, on the other hand, is quite different for each band manifold. This dissimilarity of the oscillations' phase can be well explained within a picture of interference [133, 116], where photoelectron waves emanating from the 60 carbon atoms constituting each molecule have a phase difference due to the path length difference from the atomic site to the detector. These oscillations can be approximated as spherical Bessel functions $j_l(kR)$ that depend on the radius of the molecule R, the photon energy dependent electron momentum k, and the angular quantum number l of the final state, that together with the principal quantum number n, label the molecular orbitals in C_{60} [122] as previously described.

Theory Considerations

The angular quantum number for the initial π HOMO, HOMO-1, and HOMO-2 states can be identified as $l = 5$, $l = 4$, and $l = 3$, respectively [122], and the final states are determined by the dipole selection rules, e.g. $l_i \Rightarrow l_f = l_i \pm 1$. Mathematically, the spherical Bessel functions j_l look like damped sinusoids with an approximate phase difference of $\pi/2$ between

l and $l+1$, which leads to an antiphase relation between the HOMO and HOMO-1. As can be seen in Fig. 6.6(b) and 6.6(d), this antiphase relation (between the HOMO-1 and HOMO or HOMO-2) is close to being realized, but not exact. In fact, following Xu's work [111], a more quantitative study by Hasegawa et al. [116] introduced a modified asymptotic form for the Bessel functions with a correction factor α_{l_i} describing the initial and final states. The photoionization cross section is then proportional to $\cos^2\left(kr + \alpha_{l_i} - \frac{l_i}{2}\pi\right)$ with $l_i = 5$ and $\alpha_5 = 1.66$ for the HOMO and $l_i = 4$ and $\alpha_4 = 1.43$ for the HOMO-1, giving a phase difference between the HOMO and HOMO-1 of 1.3 rad, close to the value extracted from the FFT analysis of our data, 2.4 rad (see Supp. Mat. for a more detailed analysis).

HOMO-2 Abnormalities and Orbital Character

In fact, the results from the FFT phase analysis of our data (Fig. 6.6(d)) show that while the phase across the HOMO and HOMO-1 band manifolds is nearly constant with energy, it varies substantially across the energy range of the HOMO-2. This is shown in closer detail in Fig. 6.6(e) where we plot the k_y-integrated (over the full window shown) phase for each band manifold. For each band manifold, the zero is set to its average phase (i.e. 3.03 rad, -0.82 rad, and 1.55 rad for the HOMO, HOMO-1, and HOMO-2, respectively, as shown to the right) to more easily compare phase deviations from average between the band manifolds. The range of phase deviation within the HOMO-2 is clearly much larger than for the HOMO and HOMO-1. At Γ, the HOMO-2 phase (depending on energy) spans a range of 1.24 rad, while the equivalent values for the HOMO and HOMO-1 are only 0.14 rad and 0.22 rad, respectively. As shown to the right of panel (e), the top energies of the HOMO-2 (-4 eV to -4.43 eV) have an average phase of 0.87 rad, the middle energies (-4.43 eV to -4.95 eV) have 1.40 rad, and the bottom energies (-4.95 eV to -5.8 eV) have 1.86 rad. The significant difference in phase across these energy ranges suggest a difference in orbital character of the states present within each of these energy ranges. This suggestion is strengthened by our previously discussed polarization-dependent observations for the middle and bottom energy ranges. The middle energy hosts the weakly-dispersive bands with opposite dispersions with $\perp$ or $\parallel$ light polarization (Fig. 6.4(c)), while the bottom energy has weaker bands that do not exhibit a clear linear-polarization-dependent effect. As for the circular dichroism studies, we see a clear flipping of the CD polarization between the middle (polarization of 0.10) and bottom (opposite pol. of 0.04) energy ranges (Fig. 6.5(a)). These combined observations from our linear-polarization-dependence, CD measurements, and photon-energy-dependence strongly suggest a differing in orbital character of the bands within these energy ranges. The HOMO-2 is composed of π_3, σ_8, and σ_9 states [122, 112] (or possibly π_3, σ_9, and σ_{10} [115]). So, in other words, the π_3, σ_8, and σ_9 bands are not spread evenly across the energy range, but instead are more strongly localized within certain energy ranges. Theory calculations support a localization in energy between the π and σ states, but are not definitive to their relative ordering in energy as certain models calculate the σ states to lie at the top HOMO-2 energies [136], while others calculate the σ states to lie near the bottom energies [133], and others still show them nestled in the middle energies between the π states [122, 5].

Overall, the unusual phase deviations in the HOMO-2 are a result of the mixed orbital character of this band manifold. The continuous phase shift across the HOMO-2 might hide interesting phenomena that go beyond the discrete integer $l = 5, 4, 3$ dependence (of the π states) of the spherical Bessel functions, associated to the simple interference models introduced before [116, 111]. Wang et al. [113] have suggested that the HOMO-2 oscillations are almost entirely due to the π states as they predict the σ states will only affect the overall background due to deconstructive interference. Toffoli et al. [114] similarly predict the σ states to only contribute to a smooth background and not exhibit clear oscillations. Our studies additionally examine the energy dependence of the oscillations and similarly find that the overall oscillation is largely consistent with what is expected from the π states. However, the effect of the σ states is also clear and significant considering our discussion above and in comparison to our HOMO and HOMO-1 observations (which have no σ states). Further theoretical studies may provide further insight on the oscillations of the HOMO-2 band manifold intensity with photon energy.

6.5 Conclusions

In conclusion, we have elucidated precise details of the orbital character of C_{60} valence band manifolds and the band within them through photon energy and polarization-dependent measurements. A typical photon beam used for photoemission experiments (mostly out-of-plane linear polarization) causes intensity anomalies for the HOMO and HOMO-1 within the first Brillouin zone and intensity patterns in constant energy maps well beyond the first Brillouin zone as a result of strong matrix elements effects. Additionally, the specific linear light polarization (in-plane or mostly out-of-plane) can reveal completely separate bands in the HOMO-2 and has a strong overall intensity effect for each band manifold based on its predominate orbital character. These effects should be kept in mind both for future experiments and when examining previous experiments, many of which do not take into account the effect of different polarizations. Circularly polarized data strengthen our observations of multiple bands within each band cluster as they show clear opposing CD polarizations. Additionally, the CD data reveals a band splitting at the top of the HOMO that cannot be resolved with linear polarizations. Our analysis of the C_{60} intensity oscillations with k_z finds the same frequency for the HOMO, HOMO-1, and HOMO-2, but different phases for each. Additionally, we find a variation (mainly with energy) of the phase within the HOMO-2 providing more specific details on the orbital character of the bands and their energy location. These results are well explained by a model based on the precise details of the differing orbital character of each band manifold. These results provide a comprehensive photon energy and polarization dependent study of the valence band structure of C_{60} revealing not only unique photoemission traits, but precise details of the C_{60} dispersions and their orbital character.

Bibliography

[1] H. W. Kroto et al. "C60: Buckminsterfullerene". In: *Nature* 318.6042 (1985), pp. 162–163. DOI: 10.1038/318162a0.

[2] H. W. Kroto et al. "Long carbon chain molecules in circumstellar shells". In: *The Astrophysical Journal* 314 (1987), p. 352. DOI: 10.1086/165065.

[3] W. Krätschmer et al. "Solid C60: a new form of carbon". In: *Nature* 347.6291 (1990), pp. 354–358. DOI: 10.1038/347354a0.

[4] Karl M. Kadish and Rodney S. Ruoff, eds. *Fullerenes: Chemistry, Physics, and Technology*. Wiley-Interscience, 2000. ISBN: 0471290890.

[5] N. Troullier and José Luís Martins. "Structural and electronic properties of C_{60}". In: *Phys. Rev. B* 46 (3 1992), pp. 1754–1765. DOI: 10.1103/PhysRevB.46.1754.

[6] H. W. Kroto, A. W. Allaf, and S. P. Balm. "C60: Buckminsterfullerene". In: *Chemical Reviews* 91.6 (1991), pp. 1213–1235. DOI: 10.1021/cr00006a005.

[7] S. Hüfner. *Photoelectron Spectroscopy: Principles and Applications*. 3rd. Springer Berlin Heidelberg, 2003. DOI: 10.1007/978-3-662-09280-4.

[8] Joseph Shinar, Zeev Valy Vardeny, and Zakya H. Kafafi, eds. *Optical and Electronic Properties of Fullerenes and Fullerene-Based Materials*. Marcel Dekker, Inc., 2000. ISBN: 9780824782573.

[9] J. Wu et al. "Electronic structure of single crystal C60". In: *Physica C: Superconductivity* 197.3 (1992), pp. 251–260. ISSN: 0921-4534.

[10] W. Y. Ching et al. "First-principles calculation of optical properties of C_{60} in the fcc lattice". In: *Phys. Rev. Lett.* 67 (15 1991), pp. 2045–2048. DOI: 10.1103/PhysRevLett.67.2045.

[11] Eric L. Shirley and Steven G. Louie. "Electron excitations in solid C_{60}: Energy gap, band dispersions, and effects of orientational disorder". In: *Phys. Rev. Lett.* 71 (1 1993), pp. 133–136. DOI: 10.1103/PhysRevLett.71.133.

[12] Steven G. Louie and Eric L. Shirley. "Electron excitation energies in fullerites: Many-electron and molecular orientational effects". In: *Journal of Physics and Chemistry of Solids* 54.12 (1993), pp. 1767–1777. DOI: 10.1016/0022-3697(93)90289-4.

[13] Saeid Jalali-Asadabadi et al. "Electronic Structure of Crystalline Buckyballs: fcc-C60". In: *Journal of Electronic Materials* 45.1 (2016), pp. 339–348. ISSN: 1543-186X. DOI: `10.1007/s11664-015-4080-2`.

[14] S He et al. "Angle-dependent oscillations in valence-band photoemission intensity of C 60". In: *Journal of Physics: Condensed Matter* 19.2 (2007), pp. 026202–. ISSN: 0953-8984.

[15] G. Gensterblum et al. "Experimental evidence for 400-meV valence-band dispersion in solid C_{60}". In: *Phys. Rev. B* 48 (19 1993), pp. 14756–14759. DOI: `10.1103/PhysRevB.48.14756`.

[16] P. J. Benning et al. "Band dispersion in C_{60}(111): An angle-resolved photoemission study". In: *Phys. Rev. B* 50.15 (Oct. 1994), pp. 11239–11242.

[17] J. Schiessling et al. "Polarization-dependent angular photoelectron distribution of solid C_{60}". In: *Phys. Rev. B* 68 (20 2003), p. 205405. DOI: `10.1103/PhysRevB.68.205405`.

[18] W. L. Yang et al. "Band Structure and Fermi Surface of Electron-Doped C60 Monolayers". In: *Science* 300.5617 (2003), pp. 303–307. DOI: `10.1126/science.1082174`.

[19] V. Brouet et al. "Orientation-Dependent C_{60} Electronic Structures Revealed by Photoemission Spectroscopy". In: *Phys. Rev. Lett.* 93 (19 2004), p. 197601. DOI: `10.1103/PhysRevLett.93.197601`.

[20] V. Brouet. In: *private communication* ().

[21] A. Goldoni et al. "Evidence for bandlike dispersion in K_6C_{60}(110) films". In: *Phys. Rev. B* 74 (4 2006), p. 045414. DOI: `10.1103/PhysRevB.74.045414`.

[22] T. Takahashi et al. "Photoemission study of C60 and its alkali-metal compounds". In: *Physica C: Superconductivity* 185 (1991), pp. 417–418. ISSN: 0921-4534. DOI: `http://dx.doi.org/10.1016/0921-4534(91)92011-Y`.

[23] V. Brouet et al. "Dependence of the band structure of C60 monolayers on molecular orientations and doping observed by angle resolved photoemission". In: *Journal of Physics and Chemistry of Solids* 67.1-3 (2006). Spectroscopies in Novel Superconductors 2004, pp. 218 –222. ISSN: 0022-3697. DOI: `10.1016/j.jpcs.2005.10.170`.

[24] Akshay Rao et al. "Exciton Fission and Charge Generation via Triplet Excitons in Pentacene/C60Bilayers". In: *Journal of the American Chemical Society* 132.36 (2010), pp. 12698–12703. DOI: `10.1021/ja1042462`.

[25] Sih-Hao Liao et al. "Single Junction Inverted Polymer Solar Cell Reaching Power Conversion Efficiency 10.31% by Employing Dual-Doped Zinc Oxide Nano-Film as Cathode Interlayer". In: *Scientific Reports* 4 (2014), p. 6813.

[26] Yuhang Liu et al. "Aggregation and morphology control enables multiple cases of high-efficiency polymer solar cells". In: *Nature Communications* 5 (2014), p. 5293. DOI: `10.1038/ncomms6293`.

[27] Claudia Ojeda-Aristizabal et al. "Molecular Arrangement and Charge Transfer in C60/Graphene Heterostructures". In: *ACS Nano* 11.5 (Apr. 2017), pp. 4686–4693. ISSN: 1936-0851. DOI: 10.1021/acsnano.7b00551.

[28] Kwanpyo Kim et al. "Structural and Electrical Investigation of C60–Graphene Vertical Heterostructures". In: *ACS Nano* 9.6 (2015), pp. 5922–5928. DOI: 10.1021/acsnano.5b00581.

[29] J. Cami et al. "Detection of C60 and C70 in a Young Planetary Nebula". In: *Science* 329.5996 (2010), pp. 1180–1182. DOI: 10.1126/science.1192035.

[30] Kris Sellgren et al. "C60 IN REFLECTION NEBULAE". In: *The Astrophysical Journal* 722.1 (2010), pp. L54–L57. DOI: 10.1088/2041-8205/722/1/l54.

[31] E. K. Campbell et al. "Laboratory confirmation of C60+ as the carrier of two diffuse interstellar bands". In: *Nature* 523.7560 (July 2015), pp. 322–323. ISSN: 0028-0836.

[32] H. Hertz. "Ueber einen Einfluss des ultravioletten Lichtes auf die electrische Entladung". In: *Annalen der Physik und Chemie* 267.8 (1887), pp. 983–1000. DOI: 10.1002/andp.18872670827.

[33] Wentao Zhang. *Photoemission Spectroscopy on High Temperature Superconductor*. Springer Berlin Heidelberg, 2013. DOI: 10.1007/978-3-642-32472-7.

[34] Stefan Hüfner. *Very high resolution photoelectron spectroscopy*. eng. Stefan Hüfner (ed.)., Includes bibliographical references and index. Berlin, 2007.

[35] Andrea Damascelli. "Probing the Electronic Structure of Complex Systems by ARPES". In: *Physica Scripta* T109 (2004), p. 61. DOI: 10.1238/physica.topical.109a00061.

[36] Andrea Damascelli, Zahid Hussain, and Zhi-Xun Shen. "Angle-resolved photoemission studies of the cuprate superconductors". In: *Rev. Mod. Phys.* 75.2 (Apr. 2003), p. 473.

[37] N. Mermin Neil W. Ashcroft. *Solid State Physics*. Cengage Learning, Inc, Jan. 2, 1976. 848 pp. ISBN: 0030839939.

[38] Max Gulde. *Development of an Ultrafast Low-Energy Electron Diffraction Setup*. Springer-Verlag GmbH, June 10, 2015. ISBN: 3319185608.

[39] Drew W. Latzke et al. "Electronic structure, spin-orbit coupling, and interlayer interaction in bulk MoS_2 and WS_2". In: *Physical Review B* 91.23 (2015). DOI: 10.1103/physrevb.91.235202.

[40] Qing Hua Wang et al. "Electronics and optoelectronics of two-dimensional transition metal dichalcogenides". In: *Nat Nano* 7.11 (Nov. 2012), pp. 699–712. ISSN: 1748-3387.

[41] Peter Y. Yu and Manuel Cardona. *Fundamentals of Semiconductors*. Springer Berlin Heidelberg, 2010. DOI: 10.1007/978-3-642-00710-1.

[42] Rafael Roldán and Francisco Guinea. "Electronic Properties and Strain Engineering in Semiconducting Transition Metal Dichalcogenides". In: *2D Materials*. Ed. by Phaedon Avouris, Tony F. Heinz, and Tony Low. Cambridge University Press, 2017, pp. 259–278. DOI: 10.1017/9781316681619.015.

[43] Di Xiao et al. "Coupled Spin and Valley Physics in Monolayers of MoS_2 and Other Group-VI Dichalcogenides". In: *Phys. Rev. Lett.* 108 (19 2012), p. 196802. DOI: `10.1103/PhysRevLett.108.196802`.

[44] C. N. R. Rao and U. V. Waghmare, eds. *2D Inorganic Materials beyond Graphene*. World Scientific Publishing Europe Ltd, 2017. ISBN: 9781786342690.

[45] Andrea Splendiani et al. "Emerging Photoluminescence in Monolayer MoS_2". In: *Nano Letters* 10.4 (2010), pp. 1271–1275. DOI: `10.1021/nl903868w`.

[46] Hongyi Yu and Wang Yao. "Valley-Spin Physics in 2D Semiconducting Transition Metal Dichalcogenides". In: *2D Materials*. Ed. by Phaedon Avouris, Tony F. Heinz, and Tony Low. Cambridge University Press, 2017, pp. 279–294. DOI: `10.1017/9781316681619.016`.

[47] Z. Y. Zhu, Y. C. Cheng, and U. Schwingenschlögl. "Giant spin-orbit-induced spin splitting in two-dimensional transition-metal dichalcogenide semiconductors". In: *Phys. Rev. B* 84.15 (2011), p. 153402. DOI: `10.1103/PhysRevB.84.153402`.

[48] Ting Cao et al. "Valley-selective circular dichroism of monolayer molybdenum disulphide". In: *Nat Commun* 3 (June 2012), pp. 887–.

[49] Hualing Zeng et al. "Valley polarization in MoS_2 monolayers by optical pumping". In: *Nat Nano* 7.8 (Aug. 2012), pp. 490–493. ISSN: 1748-3387.

[50] Rafael Roldán et al. "Strain engineering in semiconducting two-dimensional crystals". In: *Journal of Physics: Condensed Matter* 27.31 (2015), p. 313201. DOI: `10.1088/0953-8984/27/31/313201`.

[51] A. Klein et al. "Electronic band structure of single-crystal and single-layer WS_2 : Influence of interlayer van der Waals interactions". In: *Phys. Rev. B* 64.20 (Nov. 2001), pp. 205416–. DOI: `10.1103/PhysRevB.64.205416`.

[52] Alejandro Molina-Sánchez et al. "Effect of spin-orbit interaction on the optical spectra of single-layer, double-layer, and bulk MoS_2". In: *Phys. Rev. B* 88 (4 2013), p. 045412. DOI: `10.1103/PhysRevB.88.045412`.

[53] Nasser Alidoust et al. "Observation of monolayer valence band spin-orbit effect and induced quantum well states in MoX2". In: *Nat Commun* 5 (Aug. 2014), pp. –.

[54] T. Eknapakul et al. "Electronic Structure of a Quasi-Freestanding MoS2 Monolayer". In: *Nano Lett.* 14.3 (Feb. 2014), pp. 1312–1316. ISSN: 1530-6984. DOI: `10.1021/nl4042824`.

[55] Wencan Jin et al. "Direct Measurement of the Thickness-Dependent Electronic Band Structure of MoS_2 Using Angle-Resolved Photoemission Spectroscopy". In: *Phys. Rev. Lett.* 111.10 (Sept. 2013), pp. 106801–.

[56] S K Mahatha, K D Patel, and Krishnakumar S R Menon. "Electronic structure investigation of MoS_2 and $MoSe_2$ using angle-resolved photoemission spectroscopy and *abinitio* band structure studies". In: *Journal of Physics: Condensed Matter* 24.47 (2012), pp. 475504–. ISSN: 0953-8984.

[57] S K Mahatha and Krishnakumar S R Menon. "Inhomogeneous band bending on MoS_2(0001) arising from surface steps and dislocations". In: *Journal of Physics: Condensed Matter* 24.30 (2012), pp. 305502–. ISSN: 0953-8984.

[58] S K Mahatha and Krishnakumar S R Menon. "Quantum well states in Ag thin films on MoS_2(0001) surfaces". In: *Journal of Physics: Condensed Matter* 25.11 (2013), pp. 115501–. ISSN: 0953-8984.

[59] R. Suzuki et al. "Valley-dependent spin polarization in bulk MoS2 with broken inversion symmetry". In: *Nat Nano* 9.8 (Aug. 2014), pp. 611–617. ISSN: 1748-3387.

[60] P. E. Blöchl. "Projector augmented-wave method". In: *Phys. Rev. B* 50 (24 1994), pp. 17953–17979. DOI: `10.1103/PhysRevB.50.17953`.

[61] G. Kresse and D. Joubert. "From ultrasoft pseudopotentials to the projector augmented-wave method". In: *Phys. Rev. B* 59 (3 1999), pp. 1758–1775. DOI: `10.1103/PhysRevB.59.1758`.

[62] G. Kresse and J. Hafner. "*Ab initio* molecular dynamics for open-shell transition metals". In: *Phys. Rev. B* 48.17 (Nov. 1993), pp. 13115–13118. DOI: `10.1103/PhysRevB.48.13115`.

[63] G. Kresse and J. Furthmüller. "Efficiency of ab-initio total energy calculations for metals and semiconductors using a plane-wave basis set". In: *Computational Materials Science* 6.1 (July 1996), pp. 15–50. ISSN: 0927-0256.

[64] G. Kresse and J. Furthmüller. "Efficient iterative schemes for *ab initio* total-energy calculations using a plane-wave basis set". In: *Phys. Rev. B* 54 (16 1996), pp. 11169–11186. DOI: `10.1103/PhysRevB.54.11169`.

[65] John P. Perdew, Kieron Burke, and Matthias Ernzerhof. "Generalized Gradient Approximation Made Simple". In: *Phys. Rev. Lett.* 77 (18 1996), pp. 3865–3868. DOI: `10.1103/PhysRevLett.77.3865`.

[66] Jochen Heyd, Gustavo E. Scuseria, and Matthias Ernzerhof. "Hybrid functionals based on a screened Coulomb potential". In: *The Journal of Chemical Physics* 118.18 (2003), pp. 8207–8215. DOI: `10.1063/1.1564060`.

[67] Jochen Heyd, Gustavo E. Scuseria, and Matthias Ernzerhof. "Erratum: "Hybrid functionals based on a screened Coulomb potential" [J. Chem. Phys.118, 8207 (2003)]". In: *The Journal of Chemical Physics* 124.21, 219906 (2006), pp. –. DOI: `10.1063/1.2204597`.

[68] A. Bansil and M. Lindroos. “Importance of Matrix Elements in the ARPES Spectra of BISCO”. In: *Phys. Rev. Lett.* 83 (24 1999), pp. 5154–5157. DOI: `10.1103/PhysRevLett.83.5154`.

[69] S. Sahrakorpi et al. “Evolution of Midgap States and Residual Three Dimensionality in $La_{2-x}Sr_xCuO_4$”. In: *Phys. Rev. Lett.* 95 (15 2005), p. 157601. DOI: `10.1103/PhysRevLett.95.157601`.

[70] A. Bansil et al. “Influence of the third dimension of quasi-two-dimensional cuprate superconductors on angle-resolved photoemission spectra”. In: *Phys. Rev. B* 71 (1 2005), p. 012503. DOI: `10.1103/PhysRevB.71.012503`.

[71] Habib Rostami, Ali G. Moghaddam, and Reza Asgari. “Effective lattice Hamiltonian for monolayer MoS_2: Tailoring electronic structure with perpendicular electric and magnetic fields”. In: *Phys. Rev. B* 88.8 (Aug. 2013), pp. 085440–.

[72] Andor Kormányos et al. “Monolayer MoS_2: Trigonal warping, the Γ valley, and spin-orbit coupling effects”. In: *Phys. Rev. B* 88 (4 2013), p. 045416. DOI: `10.1103/PhysRevB.88.045416`.

[73] F. J. Himpsel. “Angle-resolved measurements of the photoemission of electrons in the study of solids”. In: *Advances in Physics* 32.1 (Jan. 1983), pp. 1–51. ISSN: 0001-8732. DOI: `10.1080/00018738300101521`.

[74] Th. Böker et al. “Band structure of MoS_2, $MoSe_2$, and $\alpha - MoTe_2$: Angle-resolved photoelectron spectroscopy and ab initio calculations”. In: *Phys. Rev. B* 64 (23 2001), p. 235305. DOI: `10.1103/PhysRevB.64.235305`.

[75] K Fives et al. “The photoelectron bandstructure of molybdenum disulphide”. In: *Journal of Physics: Condensed Matter* 4.25 (1992), p. 5639.

[76] L. F. Mattheiss. “Band Structures of Transition-Metal-Dichalcogenide Layer Compounds”. In: *Phys. Rev. B* 8 (8 1973), pp. 3719–3740. DOI: `10.1103/PhysRevB.8.3719`.

[77] R. Coehoorn et al. “Electronic structure of $MoSe_2$, MoS_2, and WSe_2. I. Band-structure calculations and photoelectron spectroscopy”. In: *Phys. Rev. B* 35 (12 1987), pp. 6195–6202. DOI: `10.1103/PhysRevB.35.6195`.

[78] Th. Böker et al. “Valence-band structure of $\alpha - MoTe_2$ by angular-resolved photoelectron spectroscopy in the constant-final-state mode”. In: *Phys. Rev. B* 60 (7 1999), pp. 4675–4681. DOI: `10.1103/PhysRevB.60.4675`.

[79] S.-W. Yu et al. “Spin resolved photoemission spectroscopy on WSe2”. In: *Journal of Electron Spectroscopy and Related Phenomena* 101103.0 (June 1999), pp. 449–454. ISSN: 0368-2048.

[80] Th. Finteis et al. “Occupied and unoccupied electronic band structure of WSe_2”. In: *Phys. Rev. B* 55 (16 1997), pp. 10400–10411. DOI: `10.1103/PhysRevB.55.10400`.

[81] K. K. Kam and B. A. Parkinson. “Detailed photocurrent spectroscopy of the semiconducting group VIB transition metal dichalcogenides”. In: *J. Phys. Chem.* 86.4 (Feb. 1982), pp. 463–467. ISSN: 0022-3654. DOI: 10.1021/j100393a010.

[82] A. Aruchamy. *Photoelectrochemistry and Photovoltaics of Layered Semiconductors.* Physics and Chemistry of Materials with Low-Dimensional Structures. Springer Netherlands, 1992. ISBN: 9780792315568.

[83] Leopold Gmelin. *Gmelin Handbook of Inorganic and Organometallic Chemistry. Mo - Molybdenum. Supplement Vol. B 7, 8, 9.* Springer, 1992. ISBN: 9783540936503.

[84] K K Kam, C L Chang, and D W Lynch. “Fundamental absorption edges and indirect band gaps in W 1-x Mo x Se 2 (Ox1)”. In: *Journal of Physics C: Solid State Physics* 17.22 (1984), pp. 4031–. ISSN: 0022-3719.

[85] Daniele Braga et al. “Quantitative Determination of the Band Gap of WS2 with Ambipolar Ionic Liquid-Gated Transistors”. In: *Nano Lett.* 12.10 (Sept. 2012), pp. 5218–5223. ISSN: 1530-6984. DOI: 10.1021/nl302389d.

[86] M. Traving et al. “Electronic structure of WSe_2: A combined photoemission and inverse photoemission study”. In: *Phys. Rev. B* 55 (16 1997), pp. 10392–10399. DOI: 10.1103/PhysRevB.55.10392.

[87] W.J. Schutte, J.L. De Boer, and F. Jellinek. “Crystal structures of tungsten disulfide and diselenide”. In: *Journal of Solid State Chemistry* 70.2 (Oct. 1987), pp. 207–209. ISSN: 0022-4596.

[88] M.S. Dresselhaus, G. Dresselhaus, and P.C. Eklund. *Science of Fullerenes and Carbon Nanotubes: Their Properties and Applications.* Elsevier Science, 1996. ISBN: 9780080540771.

[89] Y. Z. LI et al. “Ordered Overlayers of C60 on GaAs(110) Studied with Scanning Tunneling Microscopy”. In: *Science* 252.5005 (1991), pp. 547–548. ISSN: 0036-8075. DOI: 10.1126/science.252.5005.547. eprint: http://science.sciencemag.org/content/252/5005/547.full.pdf.

[90] D. Schmicker et al. “Epitaxial growth of single-crystal C_{60} on mica by helium-atom scattering”. In: *Phys. Rev. B* 44 (19 1991), pp. 10995–10997. DOI: 10.1103/PhysRevB.44.10995.

[91] G. Gensterblum et al. “C60 growth on Si(100), GaSe(0001) and GeS(001)”. In: *Applied Physics A* 56.3 (1993), pp. 175–183. ISSN: 1432-0630. DOI: 10.1007/BF00539471.

[92] G. Gensterblum et al. “High resolution electron energy loss spectroscopy of epitaxial films of {C60} grown on GaSe”. In: *Journal of Physics and Chemistry of Solids* 53.11 (1992), pp. 1427 –1432. ISSN: 0022-3697. DOI: 10.1016/0022-3697(92)90236-7.

[93] Giriraj Jnawali et al. “Observation of Ground- and Excited-State Charge Transfer at the C60/Graphene Interface”. In: *ACS Nano* 9.7 (2015), pp. 7175–7185. DOI: 10.1021/acsnano.5b01896.

[94] C. R. Dean et al. "Boron nitride substrates for high-quality graphene electronics". In: *Nature Nanotechnology* 5.10 (2010), pp. 722–726. DOI: `10.1038/nnano.2010.172`.

[95] Masatoshi Sakurai et al. "Van der Waals Epitaxial Growth of C 60 Film on a Cleaved Face of MoS 2". In: *Japanese Journal of Applied Physics* 30.11A (1991), p. L1892.

[96] Andrew J. Gibson et al. "Resonant core spectroscopies of the charge transfer interactions between C60 and the surfaces of Au(111), Ag(111), Cu(111) and Pt(111)". In: *Surface Science* 657 (2017), pp. 69–78. DOI: `10.1016/j.susc.2016.11.009`.

[97] G. K. Wertheim. "Photoemission from the valence band ofC60: Bandwidth and phonon broadening". In: *Physical Review B* 51.15 (1995), pp. 10248–10251. DOI: `10.1103/physrevb.51.10248`.

[98] G. Gensterblum et al. "Growth mode and electronic structure of the epitaxial C60(111) / GeS(001) interface". In: *Physical Review B* 50.16 (1994), pp. 11981–11995. DOI: `10.1103/physrevb.50.11981`.

[99] C.-T. Tzeng et al. "Photoemission, near-edge x-ray-absorption spectroscopy, and low-energy electron-diffraction study of C60 on Au(111) surfaces". In: *Physical Review B* 61.3 (2000), pp. 2263–2272. DOI: `10.1103/physrevb.61.2263`.

[100] Peimo He et al. "Angle-resolved UPS studies on the cleaved (111) surface of C60 single crystals". In: *Surface Science* 328.3 (May 1995), pp. 287–290. ISSN: 0039-6028.

[101] Stefan Grimme et al. "A consistent and accurate ab initio parametrization of density functional dispersion correction (DFT-D) for the 94 elements H-Pu". In: *The Journal of Chemical Physics* 132.15 (2010), p. 154104. DOI: `10.1063/1.3382344`.

[102] M. Knupfer et al. "Satellites in the photoemission spectra of A3C60(A=K and Rb)". In: *Physical Review B* 47.20 (1993), pp. 13944–13947. DOI: `10.1103/physrevb.47.13944`.

[103] P. J. Benning, F. Stepniak, and J. H. Weaver. "Electron-diffraction and photoelectron-spectroscopy studies of fullerene and alkali-metal fulleride films". In: *Physical Review B* 48.12 (1993), pp. 9086–9096. DOI: `10.1103/physrevb.48.9086`.

[104] P. J. Benning et al. "Electronic properties of K-doped C60(111): Photoemission and electron correlation". In: *Physical Review B* 47.20 (1993), pp. 13843–13847. DOI: `10.1103/physrevb.47.13843`.

[105] M S Golden et al. "The electronic structure of fullerenes and fullerene compounds from high-energy spectroscopy". In: *Journal of Physics: Condensed Matter* 7.43 (1995), pp. 8219–8247. DOI: `10.1088/0953-8984/7/43/004`.

[106] R Hesper, L. H Tjeng, and G. A Sawatzky. "Strongly reduced band gap in a correlated insulator in close proximity to a metal". In: *Europhysics Letters (EPL)* 40.2 (1997), pp. 177–182. DOI: `10.1209/epl/i1997-00442-2`.

[107] G.H. Fecher et al. "Circular dichroism in angular resolved photoemission from pure and Rb-doped C60 and C22H14 layers on platinum and tungsten". In: *Thin Solid Films* 303.1-2 (1997), pp. 58–65. DOI: `10.1016/s0040-6090(97)00088-6`.

[108] Andy Rüdel et al. "Imaging Delocalized Electron Clouds: Photoionization ofC60in Fourier Reciprocal Space". In: *Physical Review Letters* 89.12 (2002). DOI: `10.1103/physrevlett.89.125503`.

[109] Uwe Becker, Oliver Gessner, and Andy Rüdel. "Photoelectron scattering in molecules and fullerenes". In: *Journal of Electron Spectroscopy and Related Phenomena* 108.1-3 (2000), pp. 189–201. DOI: `10.1016/s0368-2048(00)00128-6`.

[110] Olaf Frank and Jan-Michael Rost. "Diffraction effects in the photoionization of clusters". In: *Chemical Physics Letters* 271.4-6 (1997), pp. 367–371. DOI: `10.1016/s0009-2614(97)00471-5`.

[111] Y. B. Xu, M. Q. Tan, and U. Becker. "Oscillations in the Photoionization Cross Section of C60". In: *Physical Review Letters* 76.19 (1996), pp. 3538–3541. DOI: `10.1103/physrevlett.76.3538`.

[112] P. J. Benning et al. "Electronic states of solid C60: Symmetries and photoionization cross sections". In: *Physical Review B* 44.4 (1991), pp. 1962–1965. DOI: `10.1103/physrevb.44.1962`.

[113] Xiao-Xiong Wang et al. "Photoemission intensity oscillations in the HOMO-2 band of {C60} film". In: *Journal of Electron Spectroscopy and Related Phenomena* 165.1-3 (2008), pp. 20–23. ISSN: 0368-2048. DOI: `10.1016/j.elspec.2008.07.004`.

[114] Daniele Toffoli et al. "Computational characterization of the HOMO-2 photoemission intensity oscillations in C60". In: *Chemical Physics Letters* 516.4-6 (2011), pp. 154–157. DOI: `10.1016/j.cplett.2011.10.006`.

[115] P. Colavita et al. "Theoretical study of the valence and core photoemission spectra of C60". In: *Phys. Chem. Chem. Phys.* 3 (20 2001), pp. 4481–4487. DOI: `10.1039/B104761M`.

[116] Shinji Hasegawa et al. "Origin of the photoemission intensity oscillation of C_{60}". In: *Phys. Rev. B* 58 (8 1998), pp. 4927–4933. DOI: `10.1103/PhysRevB.58.4927`.

[117] T. Liebsch et al. "Angle-resolved photoelectron spectroscopy of C_{60}". In: *Phys. Rev. A* 52 (1 1995), pp. 457–464. DOI: `10.1103/PhysRevA.52.457`.

[118] M. Venuti et al. "Photoionization of C60 by large scale one-center density functional explicit continuum wave-function". In: *The Journal of Chemical Physics* 111.10 (1999), pp. 4589–4597. DOI: `10.1063/1.479220`.

[119] P Decleva et al. "High energy oscillations in the valence photoionization partial cross-section of C60". In: *Chemical Physics Letters* 348.5-6 (2001), pp. 363–367. DOI: `10.1016/s0009-2614(01)01166-6`.

[120] C. Ton-That et al. “Modulations of valence-band photoemission spectrum from C_{60} monolayers on Ag(111)”. In: *Phys. Rev. B* 67 (15 2003), p. 155415. DOI: `10.1103/PhysRevB.67.155415`.

[121] Hong-Nian Li et al. “Fine structure of C60 photoionization cross-section oscillations”. In: *Journal of Physics: Condensed Matter* 19.43 (2007), p. 436223. DOI: `10.1088/0953-8984/19/43/436223`.

[122] José Luís Martins, N. Troullier, and J.H. Weaver. “Analysis of occupied and empty electronic states of C60”. In: *Chemical Physics Letters* 180.5 (1991), pp. 457–460. DOI: `10.1016/0009-2614(91)85149-q`.

[123] J. H. Weaver and D. M. Poirier. *Solid State Physics*. Ed. by Henry Ehrenreich and Frans Spaepen. Vol. 48. Advances in Research and Applications. Elsevier S&T, May 10, 1994. 434 pp. ISBN: 0126077487.

[124] Hans Kuzmany. “Fullerenforschung in der zweiten Generation”. In: *Physik in unserer Zeit* 29.1 (1998), pp. 16–21. DOI: `10.1002/piuz.19980290104`.

[125] Dennis L. Lichtenberger et al. “Electronic structure and bonding of C60 to metals”. In: *Synthetic Metals* 59.3 (1993), pp. 353–367. DOI: `10.1016/0379-6779(93)91167-z`.

[126] R. C. Haddon. “Electronic structure, conductivity and superconductivity of alkali metal doped (C60)”. In: *Accounts of Chemical Research* 25.3 (1992), pp. 127–133. DOI: `10.1021/ar00015a005`.

[127] John W. Cooper and Steven T. Manson. “Photo-Ionization in the Soft X-Ray Range: Angular Distributions of Photoelectrons and Interpretation in Terms of Subshell Structure”. In: *Phys. Rev.* 177 (1 1969), pp. 157–163. DOI: `10.1103/PhysRev.177.157`.

[128] J. Cooper and R. N. Zare. “Angular Distribution of Photoelectrons”. In: *The Journal of Chemical Physics* 48.2 (1968), pp. 942–943. DOI: `10.1063/1.1668742`.

[129] C Westphal et al. “Experimental observation of circular dichroism in photoemission”. In: *Vacuum* 41.1-3 (1990), pp. 87–89. DOI: `10.1016/0042-207x(90)90281-3`.

[130] Gerd Schönhense. “Circular Dichroism and Spin Polarization in Photoemission from Adsorbates and Non-Magnetic Solids”. In: *Physica Scripta* T31 (1990), pp. 255–275. DOI: `10.1088/0031-8949/1990/t31/035`.

[131] G Schönhense et al. “Circular Dichroism in Photoemission from Nonmagnetic, Low-Z Solids: A Conspicuous Effect of the Photon Spin”. In: *Europhysics Letters (EPL)* 17.8 (1992), pp. 727–732. DOI: `10.1209/0295-5075/17/8/011`.

[132] Richard L. Dubs, S. N. Dixit, and V. McKoy. “Circular dichroism in photoelectron angular distributions from adsorbed atoms”. In: *Physical Review B* 32.12 (1985), pp. 8389–8391. DOI: `10.1103/physrevb.32.8389`.

[133] S. Hasegawa et al. "Comparison between calculated and measured photoemission spectra of C60 thin films". In: *Journal of Electron Spectroscopy and Related Phenomena* 88 (1998), pp. 891 –895. ISSN: 0368-2048. DOI: http://dx.doi.org/10.1016/S0368-2048(97)00208-9.

[134] S. Satpathy et al. "Conduction-band structure of alkali-metal-doped C60". In: *Physical Review B* 46.3 (1992), pp. 1773–1793. DOI: 10.1103/physrevb.46.1773.

[135] A measurement in a wider range of photon energy such as Rüdel et al. [108] should give a more precise value after FFT analysis.

[136] M. Braga et al. "Electronic transition in C60 - On the origin of the strong interstellar absorption at 217 NM". In: *Astronomy and Astrophysics* 245 (May 1991), pp. 232–238.